DEUTSCHES ELEKTRONEN-SYNCHROTRON

DESY 97–201
October 1997

A Feasibility Study of High Intensity Positron Sources for the S-Band and TESLA Linear Colliders

R. Glantz

Deutsches Elektronen-Synchrotron DESY, Hamburg

ISSN 0418-9833

Gutachter der Dissertation:	Dr.habil.J.Rossbach Prof.Dr.P.Schmüser
Gutachter der Disputation:	Prof.Dr.-Ing.Dr.h.c.G.A.Voss Prof.Dr.E.Lohrmann
Datum der Disputation:	25.9.1997
Sprecher des Fachbereichs Physik und Vorsitzender des Promotionsausschusses:	Prof.Dr.B.Kramer

ISSN 0418-9833

DESY 97-201
October 1997

A Feasibility Study of High Intensity Positron Sources for the S-Band and TESLA Linear Colliders

Dissertation
zur Erlangung des Doktorgrades
des Fachbereichs Physik
der Universität Hamburg

Vorgelegt von
Rainer Glantz
aus Büchen

Hamburg 1997

Abstract

Future high energy linear colliders require luminosities above $10^{33}cm^{-2}s^{-1}$. Therefore beam intensities have to be provided up to two orders of magnitude higher than achieved at present. It is comparably simple to reach high electron intensities. Positron intensities in this range, however, are difficult to realize with conventional positron sources. A new method of positron production was proposed in 1979 by V.E. Balakin and A.A. Mikhailichenko. The photons, necessary for pair production, are not generated by bremsstrahlung but by high energy electrons passing through an undulator. Based on this principle, a high intensity, unpolarized and polarized positron source for linear colliders was developed by K.Flöttmann.

In the present work, the requirements derived by K.Flöttmann are used to study the feasibility of both the polarized and the unpolarized positron source. For economical reasons it is advantageous to use the beam after the interaction for positron production. In the main part of the present work a beam line is developed which guarantees a stable operation of the unpolarized wiggler-based positron source for the S-Band and TESLA linear collider.

The requirements on the electron beam emittances are much higher for the polarized undulator-based source. For TESLA it is shown, that an operation of the polarized source is possible for design interactions. For a stable operation, taking into account perturbations at the interaction point, further investigations are necessary. For the SBLC, an operation of the polarized source is not possible with the present design. A way out could be the use of the electron beam before the IP for positron production. In this case the dispersive crab-crossing at the IP must be replaced by rf-crab-crossing.

The beam properties before the interaction point are not critical concerning the positron production. Therefore the feasibility of the positron sources using the beam before the interaction was studied. Apart from the costs for a 3 % longer electron linac, the operation of the polarized positron sources before the interaction would lead to an undesired increase of the energy spread by a factor of 5 for TESLA.

Zusammenfassung

Zukünftige Linear Collider benötigen Luminositäten oberhalb $10^{33}\mathrm{cm}^{-2}\mathrm{s}^{-1}$. Die dafür erforderlichen Strahlintensitäten liegen bis zu zwei Größenordnungen höher als gegenwärtig erreichbar. Während die Erzeugung hochintensiver Elektronenströme vergleichsweise unproblematisch ist, können Positronenintensitäten dieser Art mit herkömmlichen Teilchenquellen nur schwer erreicht werden. Eine neue Methode der Positronenerzeugung wurde 1979 von V.E. Balakin und A.A. Mikhailichenko vorgeschlagen, bei der die für die Paarerzeugung nötigen hochenergetischen Photonen nicht durch einen Bremsstrahlungsschauer, sondern durch Photonenemission hochenergetischer Elektronen in einem Undulator entstehen. Dieses Prinzip wurde im Hinblick auf die Erzeugung hoher Positronenintensitäten von K.Flöttmann weiterentwickelt und die Anforderungen der Positronenquellen an den Elektronenstrahl ermittelt.

Darauf aufbauend wird in der vorliegenden Arbeit die Realisierbarkeit einer unpolarsierten und polarisierten Positronenquelle untersucht. Aus wirtschaftlichen Gründen ist es vorteilhaft, den Elektronenstrahl nach der Wechselwirkung zur Positronenproduktion zu benutzen. Den Schwerpunkt der vorliegenden Arbeit bildet die Entwicklung eines Strahltransportsystems, das einen stabilen Betrieb der unpolarisierten wigglerbetriebenen Positronenquelle nach der Wechselwirkung sowohl für den S-Band Linear Collider als auch für TESLA gestattet.

Die Verwirklichung der polarisierten, undulatorbetriebenen Positronenquelle bereitet größere Schwierigkeiten. Grund dafür sind die höheren Anforderungen an die Strahlemittanzen. Für TESLA konnte gezeigt werden, daß ein Betrieb unter idealen Bedingungen möglich ist. Die Stabilität dieser Quelle gegenüber kleinen Schwankungen der Betriebsparameter erfordert jedoch weitergehende Untersuchungen. Für den S-Band Linear Collider mit dem gegenwärtigen Design ist ein Betrieb der polarisierten Quelle weder vor noch nach der Wechselwirkung möglich. Das zugrundeliegende Problem könnte gelöst werden, indem das dispersive crab-crossing durch ein rf-crab-crossing schema ersetzt wird.

Die Strahleigenschaften vor der Wechselwirkung sind für den Betrieb der Positronenquellen unkritisch. Daher wurde die Möglichkeit untersucht, die Positronenquellen vor der Wechselwirkung zu plazieren. Abgesehen von den Kosten für Bau und Betrieb eines um 3 % längeren Elektronen-Linacs würde dies jedoch zu einer unerwünschten Energieverbreiterung führen, die bei TESLA das fünffache der geplanten Energiebreite beträgt.

Contents

1 Introduction **3**

2 Components of the positron source **8**
2.1 The wiggler 8
2.2 The helical undulator 10
2.3 The target 11
2.4 The capture optics 13

3 Quantum fluctuations **15**
3.1 Quantum emission of relativistic charged particles 15
3.2 Radiation characteristics of a helical undulator 16
3.3 Power deposition inside a helical undulator 18

4 Particle tracking and simulations of photon emission **23**

5 Influence of a wiggler on an electron beam **25**
5.1 Effects of a helical undulator and an ideal wiggler 25
5.2 Influence of manufacturing tolerances 30

6 Operation of a wiggler-based positron source at low energies **33**

7 Beam properties behind the interaction point **39**
7.1 Disruption 39
7.2 Energy spread 41

8 The unpolarized positron source operated with the spent beam **45**
8.1 Beam separation after the IP and the dispersion matching section 47
8.1.1 TESLA 47
8.1.2 SBLC 49
8.2 The chromaticity correction section 59
8.2.1 Methods of chromaticity correction 59
8.2.2 The chromaticity correction section and the beam transport through the wiggler for TESLA 66
8.2.3 The chromaticity correction section and the beam transport through the wiggler for the SBLC 77

9 Operational stability of the positron source using the spent beam **87**
9.1 Bunch charge oscillations due to missing interactions 87
9.2 Effects of beam-beam offsets at the IP 89

10 Potential upgrade for a polarized positron source for TESLA 94

11 Conclusions 99

A Energy deposition by a single electron inside a helical undulator 103

B A statistical expression for emittances and optical functions 108

C Phase space distributions and collimator-cuts for the SBLC spent beam capture system 110

Chapter 1

Introduction

Research into the fundamental properties of matter is an elementary subject of modern physics. Despite the great progress in this field in recent times there are many open questions left which cannot be addressed with the existing particle accelerators. For example the proof of the existence and the mass of the Higgs boson (neutral or charged), the existence of supersymmetric particles and excited leptons or quarks are some of the remaining challenges in modern physics. Research in these regions of elementary particle physics requires accelerators with higher center-of-mass (CM) energies than those currently in operation. Two general accelerator concepts can be used to go beyond the present energy range, each with its specific advantages and both schemes can be considered as complementary to the other.

Very high CM energies have been reached with hadron colliders. The existing Tevatron, used in the discovery of the top quark in 1995 reaches a beam energy of 2 TeV. The future Large Hadron Collider at CERN (LHC) will provide an beam energy of 14 TeV. This high beam energy is distributed over the constituents of the interacting beam particles, i.e. each quark carries on average 1/6 of the total energy. Thus the initial state energies of the interacting constituents are not well defined which leads to uncertainties in the analysis of the experimental data. An additional disadvantage of hadron colliders is the large experimental background which causes problems in the analysis of the interesting events. An other problem is that the hadronic constituents are themselves not yet completely understood.

In the case of e^+e^- colliders, the problems mentioned above are not existing because of the pointlike character of the leptons. The interacting particles have no inner measured structure and therefore the initial states of the interacting leptons are well defined. The background in the experiments is much lower than in hadron colliders. Therefore the properties of the reaction products can be interpreted with a higher accuracy. Circular e^+e^- colliders have been very important in the last decades, with crucial breakthroughs being made, for example the discovery of the gluon at the PETRA e^+e^- storage ring collider. At the first stage of LEP, with a CM energy of 100 GeV, it was possible to prove the existence of the Z°, the neutral gauge boson of the electroweak interaction.

The main drawback of circular e^+e^- colliders is, however, the synchrotron radiation emitted by beam particles. Particles on circular orbits are accelerated perpendicular to the direction of movement. This causes a power loss proportional to the forth power of the particle energy for a fixed radius. This power loss due to synchrotron radiation has to be replaced after each turn. As a consequence, the operational costs for circular machines rise if the CM energy will be further increased. Taking into account also the construction price, the overall costs in the

expected lifetime of an e^+e^- storage rings grows approximately with the second power of the cm energy while the cost of linear colliders grows only linearly [Rich76].

There is a broad agreement in the physics community that the next accelerator facility should be an e^+e^- collider with a cm energy of 300...500 GeV and a luminosity above $10^{33}\text{cm}^{-2}\text{s}^{-1}$. A linear collider in this energy range would provide the opportunity for complementary research to the future LHC.

Several concepts are under study to realize linear colliders of 500 GeV center of mass energy. The JLC-X,CLIC and NLC schemes are being developed at KEK, CERN and SLAC,respectively. The SBLC (S-Band Linear Collider) and TESLA (TeV Energy Superconducting Linear Accelerator) are developed by an international collaborations with DESY as coordinating institute.

The normal-conducting Linear Colliders JLC-X, NLC and SBLC differ in the choice of the rf-frequencies in their accelerating structures. The SBLC, based on conventional technology, uses 3 GHz (S-band) as accelerating frequency whereas the NLC and JLC-X accelerating sections consist of 11 GHz cavities (X-band). The high frequency accelerating structures would be small compared to the SBLC cavities. The accelerating gradient can be higher than in the SBLC scheme. The main disadvantages of the NLC and JLC-X are the tighter tolerances.

The TESLA collider differs from the above mentioned concepts because superconducting accelerating structures are foreseen. Since in superconducting technology a low rf frequency can be combined with high power efficiency, TESLA provides by far the smallest wakefield effect.This translates into comparatively loose alignment tolerances of the rf cavities and a very small energy spread of the particle beam.

The CLIC linear collider uses a very different method of beam acceleration. Instead of klystrons, a second relativistic electron beam traveling parallel to the main beam is used: The second beam generates intense wakefields which are decoupled and transmitted to the accelerating structure of the main linac. Compared to conventional generation of rf power by klystrons, the CLIC scheme favor very high rf frequencies, i.e. 30 GHz. The VLEPP concept, which was studied at the BINP, has foreseen single bunches with a very high bunch charge of $20 \cdot 10^{10}$ of particles. An overview about the main machine parameters is given in tab.(1.1).

In comparison to circular machines the bunches can be used only once. Therefore the cross sections of the bunches have to be very small and the bunch charges have to be large to reach the required luminosity in the range of 10^{33}-$10^{34}\text{cm}^{-2}\text{s}^{-1}$. The luminosity $\mathcal{L}$ can be expressed (without consideration of the luminosity enhancement factor and a luminosity loss due to a

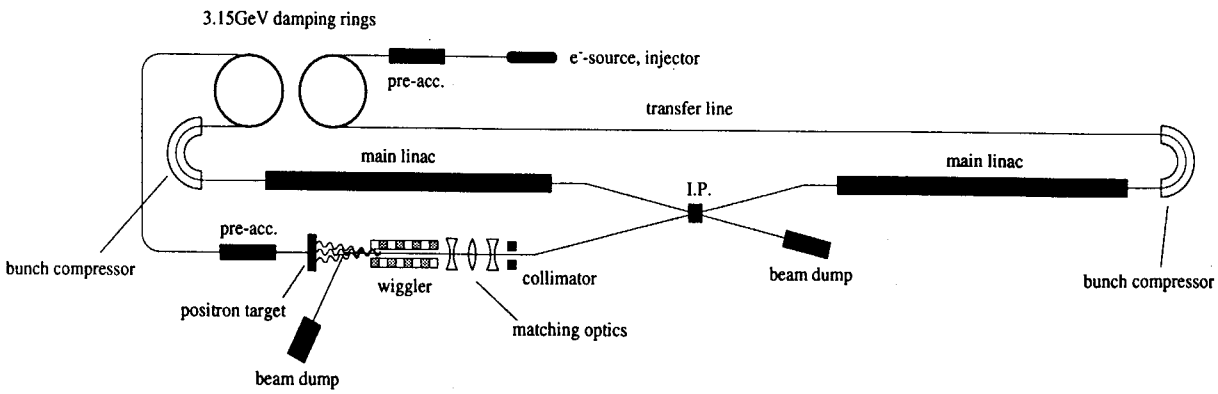

Figure 1.1: *Layout of the linac components for SBLC and TESLA*

Parameters	Units	TESLA	SBLC	JLC-X	NLC	VLEPP	CLIC
cm energy	GeV	500	500	500	500	500	500
RF frequency of main linac	GHz	1.3	3	11.4	11.4	14	30
Acc. gradient	MV/m	25	17	58	37	91	78
Luminosity	$10^{33}\mathrm{cm}^{-2}\mathrm{s}^{-1}$	6.0	5.0	5.2	7.1	9.3	1.1-4.8
Linac repetition rate	Hz	5	50	150	180	300	700
Particles per bunch	10^{10}	3.6	1.09	0.65	0.75	20	0.8
Bunches per pulse		1135	333	85	90	1	20
Avg. beam power	MW	8.25	7.26	3.2	4.8	2.6	4.5
Bunch spacing	ns	708	6	1.4	1.4	–	0.66
Hor. emittance at IP	10^{-11} rad-m	2.8	1	0.66	1	4	0.6
Vert. emittance at IP	10^{-13} rad-m	5	5	0.96	1	1.5	3
Hor. β at IP	mm	25	11	10	10	100	10
Vert. β at IP	mm	0.7	0.45	0.1	0.1	0.1	0.13
rms beam width at IP	nm	845	332	260	320	2000	264
rms beam height at IP	nm	19	15	3	3.2	4	5.15
Bunch length	mm	0.7	0.3	0.09	0.125	0.75	0.16
Crossing angle	mrad	0	6	6.1	20	6	20

Table 1.1: *Main parameters of the linear collider studies for the cm energy of 500 GeV [CDR97] [Loe95].*

crossing angle) by [Wil92]

$$\mathcal{L} = \frac{N_p^2 N_b f_{rep}}{4\pi\sigma_x\sigma_y} = \frac{P_b N_p}{4\pi E\sigma_x\sigma_y}. \tag{1.1}$$

Here N_p is the number of particles per bunch, N_b is the number of bunches per pulse and f_{rep} is the linac repetition rate. The beam power is signed as P_b, E the particle energy and σ_x and σ_y the horizontal and vertical beam size at the interaction point (IP). Equation.(1.1) shows, that the luminosity can be increased by increasing the bunch charge and the beam power or by decreasing the beam size at the IP. Each method to increase the luminosity, however, has its drawbacks. A detailed discussion of the options to reach high luminosities can be found in [Ros95]. Taking into account the coupled restrictions of the parameters, the luminosity can be alternatively expressed:

$$\mathcal{L} = A\frac{P_b}{\gamma}\sqrt{\frac{<\delta p/p>}{\varepsilon_y^n}}. \tag{1.2}$$

Here A is a constant around $10^{36}\mathrm{cm}^{-2}\mathrm{s}^{-1}$, P_b is the beam power in MW, ε_y^n is the normalized vertical emittance in rad·m and $< \delta p/p >$ is the average fractional energy loss due to beamstrahlung. The energy width, set by the experimental requirements, has to be small to ensure well defined initial conditions in the particle interactions. Therefore the only free parameters in eq.(1.2) are the beam power and the vertical emittance.

The macroscopic components of the SBLC are shown schematically in fig.(1.1). The electrons are generated in an electron gun, a GaAs cathode illuminated by a laser. They are emitted over a period of 2 μs with a repetition rate of 50 Hz and accelerated to an energy of 5 MeV. After leaving the injector system, the electron bunches are accelerated in the pre-accelerator to the energy of the following damping ring of 3.15 GeV. The damping ring consists of a low emittance Chasman-Green lattice with a radius of roughly 100 m and matches the transverse

emittances to the desired values of the main linac. After the damping ring, the bunches are shortened in a bunch compressor, a 180° arc, and transported to the main linac in which the beam is accelerated to the design energy of 250 GeV. After passing through the beam delivery system (providing a demagnification of the beam size, a chromaticity correction, beam diagnostics etc.), the beam reaches the interaction point (IP).

The macroscopic TESLA layout is basically the same as for the SBLC. Apart from the different linac technology, the damping ring between the pre-accelerator and the main linac is different. Due to the TESLA time structure, the bunch trains must be stored in a compressed mode. Even then, the required circumference is with 17 km much longer than for the SBLC. To avoid a second tunnel, the damping ring has to fit into the linac tunnel. Therefore a dogbone shape is proposed with two 8 km long straight sections with two loops of 60 m radius.

In both linear collider schemes, the positrons production differs from the method to produce electrons. The electrons after the interaction are not dumped but captured and guided to a wiggler or undulator in which they produce high energy photons. These photons are converted into positrons inside the following target. Behind the target, a capture optics matches the properties of the positron beam to the requirements of the pre-accelerator.

All linear collider schemes need high intensity particle sources. Particularly in the case of the positron sources for the high power TESLA and SBLC machines, the required intensities are up to two orders of magnitude higher than that provided by the existing ones. This would be difficult to realize by a conventional positron sources using electrons which are converted into positrons because of an heavy heat load inside the target.

An alternative concept of positron production mentioned above was first proposed by V.E. Balakin and A.A. Mikhailichenko [Bal79]. The possibilities of a high intensity wiggler or undulator-based positron source was investigated by K.Flöttmann [Flt93]. Instead of the conventional sources, the target thickness is only in the range of 0.7 radiation length. The thermal stress is reduced because it is possible to use a low Z material. A further advantage of this concept is the small beam divergence due to the thin target which leads to a high capture efficiency of the optics behind the target. The wiggler-based positron source provides unpolarized positrons.

The study of the interaction between polarized electrons and positrons is of great interest to the particle physics community. The interaction between polarized particle beams gives for example the opportunity to discover the spin dependence of the weak interaction and to suppress the background in W^+W^- production. An overview of the physical foundations and the expected results can be found in [JLC92]. The use of a 100 m long helical undulator for photon production gives the opportunity to generate longitudinally polarized positrons.

In the present work, the feasibility of wiggler- and undulator-based positron sources for the TESLA and S-Band linear colliders is studied.

In order of cost reduction, the source is proposed to be operated using the electron beam behind the IP for positron production (see fig.(1.1)). The realization of this option encompasses the main part of this work. The advantages and drawbacks of operating the positron source with the beam before the IP will also be discussed. This will be covered in the first part of this paper because the analysis of this option will also have consequences on the part concerning the spent beam operation.

The present work is structured as follows:

- The results from [Flt93] are summarized in the second chapter. The single components of the positron sources and the requirements on the electron beam will be described briefly.
- The radiation characteristics of relativistic electrons influenced by a magnetic field is treated in the third chapter. This is important for the simulation of quantum excitation of a particle beam along dispersive regions. Furthermore, the properties of the radiation produced in a helical undulator will be described. This will be used to estimate the deposited radiation power inside the superconducting undulator.
- In the following chapter, the method of particle tracking including the simulation of quantum emission will be explained.
- After the previous more general part, the effects of a wiggler or undulator on an electron beam will be presented in chapter (5). In the first section, the consequences of an ideal wiggler and undulator will be treated. It follows the analysis of manufacturing tolerances of a wiggler. The reason of this chapter is to investigate whether the positron source can be operated before the IP without disadvantages for the experiments.
- The possibilities to operate the wiggler-based positron source below the design energy is studied in the chapter (6). The calculations were started for the positron source before the IP. As shown in the last part of this section, the resulting lower limit for the cm energy providing a reasonable operation of the linac can be generalized for the spent beam operation.
- The beam properties behind the interaction point are analyzed in chapter (7) to prepare the development of the spent beam capture system for the positron source behind the IP.
- In chapter (8), the spent beam capture system for the unpolarized wiggler-based positron source will be developed. In the first part of this chapter treats the spent beam separation from the oncoming positron beam. The spent beam extraction section for TESLA, developed by A.Drozhdin [Dro94] will be described briefly. Than follows the analyzes of the final focus quadrupoles for the SBLC an their consequences on the spent beam properties. The methods of chromaticity correction is explained in the following section. After this is done, the structure of the chromaticity correction section is explained for the TESLA spent beam capture system. In the last part of this chapter, the SBLC capture system is described.
- Since the spent beam capture system is developed for interactions under design conditions, the effects of perturbations at the IP are studied in chapter (9).
- In chapter (10) the potential upgrade to an undulator-based polarized positron source is described for TESLA.
- The results of the present work are summarized in the last chapter.

Chapter 2

Components of the positron source

The high intensity positron sources for the next generation of linear colliders studied here are operated using a high energy electron beam to produce photons which are converted into electron-positrons pairs in a thin target. In the case of the polarized source these photons must be be circularly polarized. While the unpolarized source can be realized with a planar wiggler, the polarized source requires a helical undulator which is preferably built as a superconducting device. Behind the target the outcoming diverging particles are collected by a capture optics and accelerated in a following linac. It is possible to operate the positron source either with the beam before the IP or with the spent beam after the interaction. Shown in fig.(2.1) is a sketch of a wiggler-based positron source using the spent electron beam for photon production. The single components of the polarized and unpolarized positron source and the requirements on the electron beam will be described briefly in this chapter.

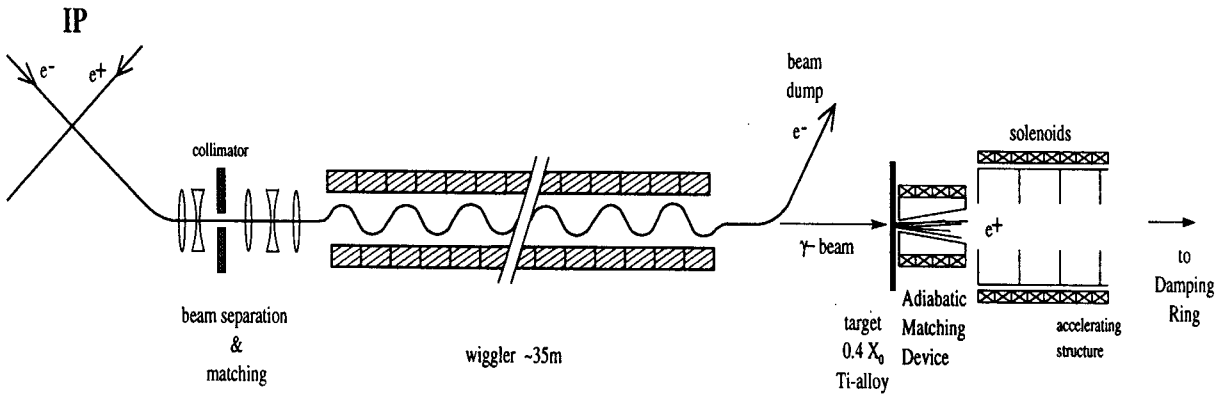

Figure 2.1: *A sketch of the components of the unpolarized positron source using the spent beam for positron production. In the case of the polarized positron source, the wiggler has to be replaced by an approximately 100 m long helical undulator; The distance between the end of the undulator and the target has to be increased to* ≈ 150 *m.*

2.1 The wiggler

In the case of an unpolarized positron source, the high energy photons are generated in a planar wiggler consisting of a sequence of short dipoles with alternating polarity. Electrons passing through such a device emit electromagnetic radiation as they are deflected by the

magnetic field. The characteristics of the radiation are similar as those of radiation produced by electrons passing through a dipole, if the so-called wiggler parameter

$$K = \frac{\lambda_W e B}{2\pi m_e c} = 0.94\ \lambda_W[\text{cm}]\ B[\text{T}], \tag{2.1}$$

is much greater than one. Here λ_W is the period length of the wiggler, c the velocity of light and B the wiggler strength; m_e and e denote the electron mass and the electron charge, respectively. The emission of quanta along the path through the wiggler is a statistical process, i.e. the position and energy of the photons is not determined. The opening angle of the radiation cone is $\theta_{rad} \approx 1/\gamma$. The condition $K >> 1$ implies, that θ_{rad} is much less than the deflection of the particle trajectories inside the wiggler. The photons are emitted incoherently and the photon number spectrum (the number of photons emitted per unit energy) and the power density spectrum (the radiated power per energy interval) are the same as those of synchrotron radiation generated in a dipole. The process of quantum emission will be explained in more detail in chapter (3).

The optical functions of the electron beam inside the wiggler are chosen such that the emitted photons are focussed onto the thin conversion target. The electron beam has to be deflected away from the target at the end of the wiggler. Behind the target, a solenoid field is foreseen to collect the positrons leaving the target.

The size of the radiation spot on the target is a critical parameter in the performance of the source. The radiation spot size on the target has to be small in order obtain a small emittance of the positrons emerging from the target. On the other hand, a very small radiation spot may laed to intolerable local heat loads on the target. An optimum value for the horizontal and vertical radiation spot size was found to be ≈ 0.7 mm (K.Floettmann [Flt93]). The spot size σ is determinated by the opening angle of the radiation generated inside the wiggler *and* the diameter of the virtual electron beam on the target. Both components add up quadratically and have to be in the order of ≈ 0.5 mm to reach the optimum radiation spot size of ≈ 0.7 mm. The spot size on the target can be approximated by

$$\sigma \approx \frac{eB\lambda_w}{2\pi p_e} \cdot (L/2 + D) \tag{2.2}$$

where L is the wiggler length and D the length of the drift space between the wiggler and the target. From eq.(2.2) follows the relation between the period length of the wiggler and the radiation spot size on the target. In [Flt93] the source parameters were calculated based on a wiggler of length 40 m with 10 m distance to the target. Together with a wiggler strength of 1.7 T this leads to a maximum period length of λ_W of 51 mm to reach the horizontal spot size of 0.5 mm. The electron beam is focused in such a way that the virtual spot size on the target is the same as that of the spot size due the opening angle of the radiation.

The maximum allowable electron beam emittance is determined by required virtual electron spot size σ_e^* and the aperture of the wiggler. The emittance requirements, estimated in [Flt93], are

$$\varepsilon_x = 1 \cdot 10^{-2}\text{mm mrad}, \quad \varepsilon_y = 5 \cdot 10^{-3}\text{mm mrad}. \tag{2.3}$$

These values, based on the same parameters mentioned above, were taken as an orientation to create a capture system for the spent beam. It has been found that a horizontal emittance of $\varepsilon_x = 2 \cdot 10^{-2}$mm mrad is sufficient for a reliable operation of the unpolarized source. This is the subject of chapter (8).

The dependence of the positron production on the wiggler parameters is very complicated. The present parameters for the unpolarized source using the spent electron beam at 250 GeV are shown in tab.(2.1). The source could alternatively be installed before the IP. Due to the

Wiggler	
field on axis	1.7 T
period length	51 mm
gap height	5 mm
# of photons p. electron	357
mean photon energy	22 MeV
photon beam power	250 kW

Table 2.1: Overview of the main wiggler parameters.

small beam emittance there, a broad range of wiggler parameters could be realized. However, a deterioration of the beam quality before the IP would result. The advantages and disadvantages of this option will be discussed in chapters (6) and (5).

2.2 The helical undulator

The study of interactions of longitudinally polarized high energy electrons with polarized positrons is of great interest to the particle physics community. The interaction between polarized particle beams gives for example the opportunity to discover the spin dependence of the weak interaction and to suppress the background in W^+W^- production. An overview of the physical foundations and the expected results can be found in [JLC92].

While polarized electrons can be produced by illuminating a photo cathode with circularly polarized laser light, the production of longitudinally polarized positrons is much more complicated. The basic idea for a polarized positron source was proposed by V.E.Balakin and A.A.Mikhailichenko in 1979 [Bal79].

In this scheme a helical undulator is used instead of a planar wiggler. The undulator consists of a pair of conductors which are wound in the form of a double helix. The currents in the two conductors are equal but travel in opposite directions. The axial components of the magnetic fields cancel and only transverse field components remain. The field pattern along the axis can be described by [Ell90]

$$\mathbf{B}(z) = B_0 \cdot (\sin(k_u \cdot z), \cos(k_u \cdot z), 0), \tag{2.4}$$

where $k_u = 2\pi/\lambda_u$ and where λ_u is the undulator period. Particles passing through this field follow helical trajectories.

An analytical formula for the magnetic field on-axis as a function of the undulator parameters (for an undulator without an iron yoke) was found by J.P.Bewlett and R.Chasman [Bew77]:

$$B_0 = 2.385 \cdot 10^{-4}[\mathrm{T \cdot mm/A}] \cdot I \cdot \lambda_u \left[\exp\left(-\frac{5.68 r_i}{\lambda_u}\right) - \exp\left(-\frac{5.68 r_o}{\lambda_u}\right)\right], \tag{2.5}$$

where I is the current density in [A/mm^2], r_i the inner and r_o the outer coil radii. A transverse field component B of 0.9 T can be reached with an axial width of $\lambda_u/3$ for the conductor, r_i=2 mm and r_o=6.8 mm, λ_u = 12 mm and I = 900 A/mm^2. The energy spectrum of the

photons produced by an undulator is different from that produced by a wiggler. The photon spectrum has maxima in the positions of the harmonics of the undulator radiation. The energy of the first harmonic is given by [Kin77]

$$E_1 = \hbar \frac{4\pi\gamma^2 c}{(1+K^2)\,\lambda_u}. \tag{2.6}$$

The undulator parameters were chosen such that the energy of the first harmonic was approximately 20 MeV. The contribution to positron production of photons with energy lower than 20 MeV is negligible because of the small cross section of pair production in this range. Shown in tab.(2.2) are different values of the undulator strength B and the corresponding period length λ_u with which one can realize the required photon energy E_1 of 20 MeV.

K	B[T]	$\lambda_u[cm]$
0.5	0.23	2.4
0.7	0.38	2.0
1.0	0.72	1.5
1.2	1.06	1.2
1.5	1.76	0.9

Table 2.2: Undulator parameters for the polarized source providing an energy of the first harmonic of 20 MeV.

A detailed description of the radiation characteristics of helical undulators can be found in the work of B.M. Kincaid [Kin77]. It can be shown that the photons emitted with a small angle to the undulator axis are nearly circularly polarized. The degree of longitudinal polarization decreases, and the fraction of transversely polarized photons increases for increasing emission angles. Thus, the radiation emitted under a large emission angle has to be scraped off before the target.

The radiation spot size on the target has to be dominated by the natural opening angle of the radiation and not by the contribution of the electron beam emittance. The distance between the end of the undulator and the target has to be much longer than for the unpolarized source. In the present design, an undulator length of 100 m and a distance to the target of 150 m are foreseen.

To estimate the electron beam emittance requirements the radiation spot size of the first harmonic has to be compared with the virtual spot size of the electron beam on the target. Extensive numerical calculations have been done by K.Floettmann [Flt93]. The degree of longitudinal polarization and the photon yield were studied as a function of the scraping angle. The required emittances were found to be

$$\varepsilon_x = 5 \cdot 10^{-4}\text{mm mrad}, \quad \varepsilon_y = 5 \cdot 10^{-4}\text{mm mrad}, \tag{2.7}$$

which are much smaller than for the unpolarized source. The design parameters for the polarized positron source [Flt93] are collected in tab.(2.3)

2.3 The target

The principle to realize a positron source is to convert photons into e^+-e^- pairs in a suitable material. The incident particles are electrons in the case of conventional positron sources or

inner coil radius	2-3 mm
current density	900 A/mm^2
undulator period	1.2 cm
undulator field	0.9 T
undulator parameter K	0.98
undulator length	$\approx$ 100 m
maximum polarization	66 %

Table 2.3: Parameters of a highly polarized, high intensity positron source.

photons in the case of wiggler or undulator based sources. The highest positron intensity is produced by the currently operating SLC source at SLAC, with intensities around $6 \cdot 10^{12}$ positrons per second. This is up to two orders of magnitude less than that required for future linear colliders. The highest required positron intensities are roughly $2 \cdot 10^{14}$ positrons per second, required for the TESLA and the SBLC schemes. Since the achievable positron intensity is limited by thermal stresses inside the target, a promising alternative is to use a photon beam instead of an electron beam.

High energy photons or electrons passing through a material create electromagnetic showers. Photons interact with matter through pair production, compton scattering and photoelectical effect. At high energies, the cross section is dominated by pair production. High energy electrons interact with matter through ionization and emission of bremsstrahlung photons. The photons again produce e^+-e^- pairs, and in this way a shower cascade is created with an exponentially growing number of particles. The shower maximum is reached when the ionization losses of the charged particles are equal to the energy loss due to bremsstrahlung. The particle energy at this point is called the critical energy E_c, given by $E_c \approx 580\text{MeV}/Z$, where Z denotes the nuclear charge. After this point, the number of charged particles in the shower decreases. The shower propagation stops when the energy loss of the particles is dominated by ionization losses.

The longitudinal shower development in a given material the so called radiation length X_0 which depends on the material properties in the following way [Kle84]:

$$X_0^{-1} = \frac{4\alpha r_e^2 N_A \rho}{A} \cdot Z(Z+1) ln(183 Z^{1/3}). \tag{2.8}$$

Here A is the atomic weight, Z the nuclear charge and ρ the density of the material and N_A is Avogadro's number.

The development of showers initiated by electrons is similar to that of photons. With main difference being that the primary photon passes through a material creates an e^+-e^- pair with a probability of 54 % after one radiation length. Electron, however, loose 63 % of their energy due to bremsstrahlung after one radiation length. Hence the use of photons instead of electrons allows one to use a thinner target.

While the longitudinal shower development is determined by ionization losses and pair production, the transverse shower development depends on multiple scattering of the shower particles. A useful parameter to quantify the transverse shower size is the so-called Moliere-radius, $R_M = 21\text{MeV} \cdot X_0/E_c$: 99% of the total shower energy can be found inside a cylinder with a radius of $3R_M$ around the longitudinal shower axis. The spread of the shower particles grows proportional by the square root of the the shower depth. Thus, with a thin target the

spread of the particles emerging from the target is small, resulting in an improved efficiency of the following capture optics.

Conventional positron sources, which use electrons as incident particles require a full development of the electromagnetic shower to achieve a high positron yield. Therefore the target thickness has to be many radiation lengths. To make effective use of the target thickness, the positrons produced in the early stage of the shower development must leave the target. As shown by K.Floettmann, the escape depth for positrons increases with the nuclear charge Z of the target material. Hence low Z materials should be avoided although these are advantageous with respect to their heat capacity. The advantages of positron sources operated by high energy photon beam can be summarized as follows:

- The target thickness can be chosen to be less than one radiation length since the first interaction inside the target is the production of an e^+-e^- pair.
- The thin target reduces the angular divergence of the positrons emerging from the target. This improves the efficiency of the following positron capture optics.
- A low Z material can be used. This causes a high heat capacity of the target and therefore a reduction of the heat load.

Numerical simulations have been done [Flt93] to determine the optimum thickness and the material of the target. The analyses was done using the shower simulation program **EGS4**. The optimum target thickness with regard to the overall efficiency (i.e. including the capture efficiency of the following optics) is about $0.4X_0$. The optimum material was found to be a titanium alloy.

A rotating target is foreseen to distribute the deposited energy and in this way to reduce the average heat load. The bunch spacing is very large for TESLA (Δs= 708 nm), thus the rotation velocity can be chosen so that adjacent bunches do not overlap. A target with a diameter of 80 cm is foreseen rotating at 1210 revolutions per minute. The average power deposition of 7 KW leads to a maximum temperature rise of 380°C inside the target.

The bunch spacing in the SBLC is only 6 ns. Therefore it is not possible to separate the single incident bunches by a rotating target. Despite this, the average heat load is reduced if adjacent bunch trains do not hit the target in the same position. For the SBLC, an average heat load of 6 KW leads to a maximum temperature of 780 °C, which cannot be dissipated by radiation. Water cooling of the target is then necessary for the SBLC.

2.4 The capture optics

The beam of particles leaving the target have a large angular divergence and a small spot size, even if the target is thin. These particles have to be captured and accelerated in a cavity which is surrounded by a solenoid. The acceptance of this device is characterized by a small divergence and a large spot size. To match the output of the target to the input of the cavity, a so-called Adiabatic Matching Device (AMD) is foreseen between the target and the first accelerating cavity. The AMD is made of a tapered solenoid field starting with a high initial field strength which decreases to a lower constant end field. Particle motion inside such a field has been analyzed by R.Helm [Hel62]. It has been found that the on-axis field to match the target optimally to the accelerating cavity is

$$B(z) = \frac{B_i}{1 + g \cdot z} \tag{2.9}$$

where z is the longitudinal position, g the so-called taper parameter, B_i the initial solenoid field at the entrance of the adiabatic matching device. The condition for adiabatic field variation is given by $(gp_e)/(eB_i) \ll 1$. The taper parameter has to be small in order to fulfill the condition also for high energy particles. A small taper parameter leads, however, to an increased bunch length and so a compromise is needed. At present, a taper parameter of $g = 30$ m^{-1} is foreseen. A capture efficiency of 17 % can be reached with an initial field strength B_i of 6 T which decreases to $B_e = 0.16$ T at the end of the matching device. The capture efficiency as a function of the radiation spot size on the target was estimated by K.Floettmann [Flt93] and can be found in fig.(6.2).

Chapter 3

Quantum fluctuations

Charged particles generate electromagnetic radiation during acceleration. This fact is responsible for the growth of the horizontal emittance along dispersive regions which has to be taken into account in the design of the capture system for the spent beam.

Despite the disadvantage of an increased emittance, it is the presupposition for operating positron sources by creating photons in a periodic magnetic field. While an unpolarized source can be realized with a conventional planar wiggler, a helical undulator is necessary for a polarized source. In the wiggler, the high energy electrons emit photons mainly in the horizontal plane in which the radiated energy cannot cause damage because the aperture is limited only in the vertical direction. The opening angle in the vertical plane is of the order of $1/\gamma \approx 2\mu$rad which is not critical for a comparatively short wiggler. In the case of the helical undulator the particles follow helical trajectories. As shown later, the distribution of the emitted photons is symmetric around the undulator axis. The aperture is limited by the inner radius of the superconducting coil minus the wall thickness of the beam pipe and the space for the liquid helium. Thus, it is not sufficient to guarantee that particles do not hit the wall. It has also to be ensured that the radiated power deposited in the coil does not lead to an intolerable heating. This is particularly critical if a superconducting undulator is to be considered.

An overview of the foundations of quantum emission is given in the first section of this chapter. In the last sections of this chapter the radiation characteristics of a helical undulator and the power deposition inside of it are given following B.M. Kincaide [Kin77].

3.1 Quantum emission of relativistic charged particles

The emission spectrum of a relativistic charged particle can be calculated from the Liénard-Wiechert potentials. From J.D.Jackson [Jack83] one gets

$$\frac{d^2I}{d\omega d\Omega}(\mathbf{n},\omega) = \frac{e^2\omega^2}{16\pi^3\varepsilon_0 c}\left|\int_{-\infty}^{\infty} \mathbf{n}\times(\mathbf{n}\times\boldsymbol{\beta}(t))\exp\left(i\omega\left(t-\frac{\mathbf{n}\cdot\mathbf{r}(t)}{c}\right)\right)dt\right|^2 \qquad (3.1)$$

for the energy radiated into the solid angle interval $d\Omega$ around the unit vector in the direction of observation $\mathbf{n}$, in the frequency range $d\omega$ around ω. The vector $\mathbf{r}(t)$ describes the trajectory of the charged particle and $\boldsymbol{\beta}$ the vector of its velocity normalized to the velocity of light, c. The MKSA-system is used in all following calculations.

For an electron on a circular trajectory with radius ρ one gets

$$\frac{d^2I}{d\omega d\Omega}(\theta,\omega) = \frac{e^2}{12\pi^3\varepsilon_0 c}\left(\frac{\omega\rho}{c}\right)^2\left(\frac{1}{\gamma^2}+\theta^2\right)^2\left[K_{2/3}^2(\xi)+\frac{\theta^2}{(1/\gamma^2)+\theta^2}K_{1/3}^2(\xi)\right], \tag{3.2}$$

where θ is the angle between the observation point and the tangent to the trajectory, measured in the plane normal to that of the plane of movement and tangential to it.

$$\xi = \frac{\omega\rho}{3c}\left(\frac{1}{\gamma^2}+\theta^2\right)^{3/2}. \tag{3.3}$$

Here $K_{1/3}$ and $K_{2/3}$ are the modified Bessel-functions of the order 1/3 and 2/3. Integration of eq.(3.2) over the solid angle leads to the power density spectra [Sands]

$$P(\omega) = \frac{P_\gamma}{\omega_c}\cdot S(\frac{\omega}{\omega_c}) = \frac{4}{9}\,r_e ecB\cdot S(\frac{\omega}{\omega_c}) \tag{3.4}$$

with the classical electron radius r_e and the total radiated power

$$P_\gamma = \frac{2}{3}\frac{r_e e^2 c}{m}\gamma^2 B^2. \tag{3.5}$$

$S(\omega/\omega_c)$ is the spectral function:

$$S(\zeta) = \frac{9\sqrt{3}}{8\pi}\zeta\int_\zeta^\infty K_{5/3}\left(\bar{\zeta}\right)d\bar{\zeta}, \qquad \zeta = \frac{\omega}{\omega_c}, \tag{3.6}$$

and

$$\omega_c = \frac{3}{2}\frac{c\gamma^3}{\rho}, \tag{3.7}$$

where ω_c is called the critical frequency. Integration of $S(\zeta)$ from $\zeta = 0$ to $\zeta = 1$, i.e. the integrated power in the range between zero and ω_c yields $\frac{1}{2}$. Hence the critical frequency divides the radiation spectrum into two regions of equal power emission. The radiation emission is not a continuous process. The number of quanta emitted with energy $u = \hbar\omega$ per unit time and per energy interval can be derived from the power density spectrum. One gets

$$n(u) = \frac{8}{27}\frac{r_e m_0 c}{\hbar^2}\cdot F(\zeta), \qquad F(\zeta) = \frac{1}{\zeta}S(\zeta). \tag{3.8}$$

The normalized power spectrum $S(\zeta)$ and the photon number spectrum $F(\zeta)$ are shown in fig.(3.1).

3.2 Radiation characteristics of a helical undulator

The polarized positron source proposed by [Bal79] is based on a helical magnetic field which produces longitudinally polarized photons. The photons are converted into polarized positrons in a thin target. The helical field can be achieved by a pair of conductors wound to form a double helix. The current in the conductors is equal and of opposite direction. The helical undulator has to be superconducting in order to provide a sufficiently high field strength and

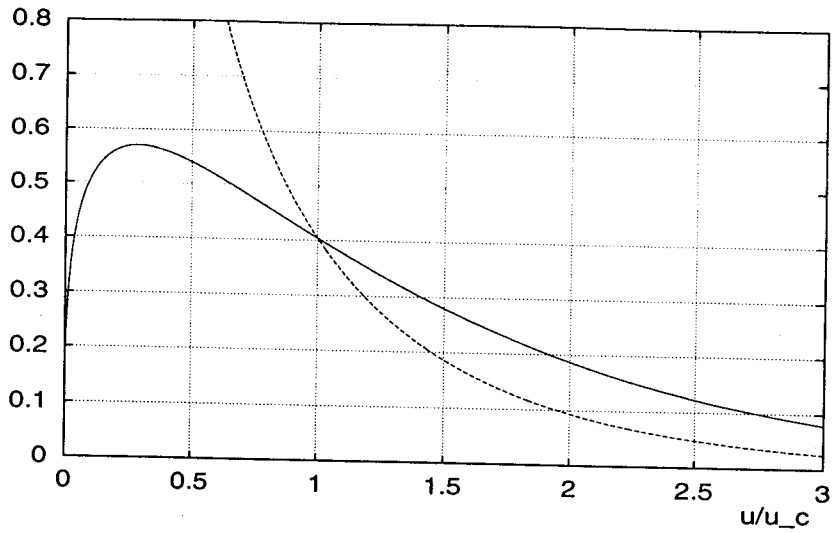

Figure 3.1: *Normalized power spectrum $S(\zeta)$ (solid line) and photon number spectrum $F(\zeta)$ (broken line) as a function of the photon energy in units of the critical energy $u_c = \hbar\omega_c$*

a small period length. Choosing the longitudinal axis as the z-direction, the magnetic field in a helical undulator can be expressed as

$$\mathbf{B}(z) = B_0(\sin(k_u \cdot z), \cos(k_u \cdot z), 0), \tag{3.9}$$

where $k_u = \frac{2\pi}{\lambda_u}$ with the undulator period λ_u. The integration of the equation of motion yields the particle trajectory [Ell90]

$$\mathbf{r}(t) = (r_0 \cdot \sin\left(k_u\bar{\beta}ct\right), r_0 \cdot \cos\left(k_u\bar{\beta}ct\right), \bar{\beta}ct), \tag{3.10}$$

with

$$\bar{\beta} = \beta\sqrt{1 - \frac{K^2}{\gamma^2}} \tag{3.11}$$

and

$$r_0 = \frac{K\lambda_u}{2\pi\gamma}. \tag{3.12}$$

K is called the undulator parameter and is given as:

$$K = \frac{e}{2\pi m_0 c} B_0 \lambda_u, \tag{3.13}$$

where B_0 is the magnetic field. The emission spectra, calculated in [Kin77] can be derived from eq.(3.9), eq.(3.11) and eq.(3.1) as

$$\frac{d^2I}{d\omega d\Omega}(\theta,\omega) = \frac{e^2\omega^2K^2}{4\pi^3\varepsilon_0\omega_u^2\gamma^2 c} \cdot \sum_{n=-\infty}^{\infty} \left(\frac{\sin(N\pi(\omega/\omega_1 - n))}{(\omega/\omega_1 - n)}\right)^2 \cdot \left[J_n'^2(x) + \left(\frac{\gamma\theta}{K} - \frac{n}{x}\right)^2 J_n^2(x)\right], \tag{3.14}$$

where J_n and J_n' is the Bessel function of nth order and its first derivative, respectively,

$$x = \frac{K\omega\theta}{\gamma\omega_u}, \qquad \omega_u = k_u\bar{\beta}c \qquad \text{and} \qquad \omega_1 = \frac{2\gamma^2\omega_u}{1 + K^2 + \gamma^2\theta^2}. \tag{3.15}$$

Here θ denotes the angle between the undulator axis and the vector pointing to the observer. N is the number of undulator periods. Equation (3.14) can be integrated over all frequencies if the number of undulator periods is sufficiently large ($N > 100$). Then the sinc-function inside the sum can be replaced by a δ-function. Hence the angular distribution of the radiated energy follows:

$$\frac{dI}{d\Omega}(\theta) = \frac{8Ne^2\gamma^4\omega_u}{4\pi\varepsilon_0 c}\frac{K^2}{(1+K^2+\gamma^2\theta^2)^3}\cdot\sum_{n=1}^{\infty} n^2\cdot\left[J_n'^2(x_n)+\left(\frac{\gamma\theta}{K}-\frac{n}{x_n}\right)^2 J_n^2(x_n)\right], \qquad (3.16)$$

with

$$x_n = \frac{2Kn\gamma\theta}{1+K^2+\gamma\theta}, \qquad (3.17)$$

The angular distribution of the radiated energy is shown in fig.(3.2) for different values of K.

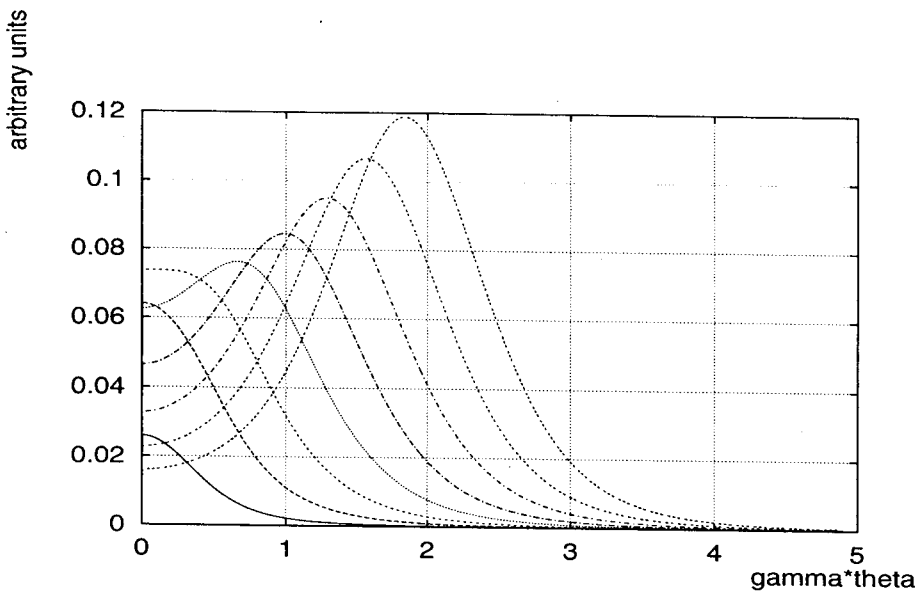

Figure 3.2: *Angular distributions of the energy radiated in a helical undulator, integrated over all frequencies. The distributions are shown for several values of K starting at K=0.25 (the lowest, most left function) to K=2.0 (the highest most right function) in equidistant steps of 0.25.*

3.3 Power deposition inside a helical undulator

In this section the energy deposited inside a helical undulator by a single relativistic electron will be calculated. The undulator is assumed to be superconducting. Therefore one has not only to ensure that particles do not hit the superconducting coil, in addition the energy deposition in the helium due to radiation must be sufficiently low. The first calculations were made assuming a negligible beam height and beam width inside the undulator. This is the case if the electron beam is used before the interaction region, where the emittances are very small. In the spent electron beam, the emittances are larger (see chapters (7) and (8)) and it is to be expected,

that particles passing through the undulator near the coil would deposit more energy than that calculated for on-axis particles. To get an impression of the deposited power for a beam whose envelope is in the order of magnitude of the inner radius of the undulator, some semianalytical calculations will be done at the end of this chapter.

The deposited energy has been estimated numerically by dividing the undulator with length L and inner radius r into $\nu = 100$ equidistant parts. Each of these parts is treated as a single undulator which emits radiation with an angular distribution $dI(\theta)/d\Omega$ following eq.(3.16). The sum of the deposited energy from each part is then formed. Apparently this is not correct for the calculation of the energy deposition into the adjacent part, because in this range, the far field approximation is not valid. However, the energy radiated into this range is negligible. The energy produced in the i^{th} part which is radiated into the wall of a following part with the index j is calculated by:

$$E_{i,j} = 2\pi \int_{\theta_{i,j_{min}}}^{\theta_{i,j_{max}}} \frac{dI}{d\Omega}\left(\tilde{\theta}\right) \sin\tilde{\theta}\, d\tilde{\theta}, \tag{3.18}$$

with the integration limits

$$\theta_{i,j_{max}} = \arctan\left(\frac{r}{L}\frac{\nu}{j-i-1}\right), \quad \theta_{i,j_{min}} = \arctan\left(\frac{r}{L}\frac{\nu}{j-i}\right), \quad i < j. \tag{3.19}$$

The sum of the deposited energy inside the j^{th} part due to the radiation produced in the previous parts (i=1,...,j-1) is calculated according to

$$E_j = \sum_{i=1}^{j-1} E_{i,j}. \tag{3.20}$$

Equation (3.20) refers to an energy deposition of a single electron in the j^{th} part of the undulator. The total deposited power is:

$$P_{tot} = N_p N_b f_{rep} \sum_{j=1}^{j=\nu} E_j. \tag{3.21}$$

Here N_p is the number of particles per bunch, N_b the number of bunches per pulse and f_{rep} the linac repetition frequency. The deposited power is not distributed uniformly. Therefore it is also important to study the power deposited per unit length along the undulator. It has to be ensured that no intolerable local heat load, particularly at the end, could cause a quench. The power per unit length has been obtained from the local energy deposition as follows:

$$\frac{dP_j}{dx} = \frac{\nu}{L} N_p N_b f_{rep} E_j, \quad x = j \cdot L/\nu. \tag{3.22}$$

Figure (3.3) shows the deposited power per unit length as a function of the position inside the undulator for the present TESLA parameters (see tab.(1.1)). The undulator parameter K is chosen to be 1 with an on-axis field B of 0.9 T and a period length λ_u of 12 mm. The inner radius of the undulator r is assumed to be 2.5 mm and the length L is set to 150 m for all calculations. The maximum power deposited per unit length is about 0.7 W/m at the end of the undulator which is not critical.

Figure (3.4) shows the total deposited power which is radiated into the undulator as a function of the inner radius. The maximum of the angular distribution of the radiated energy

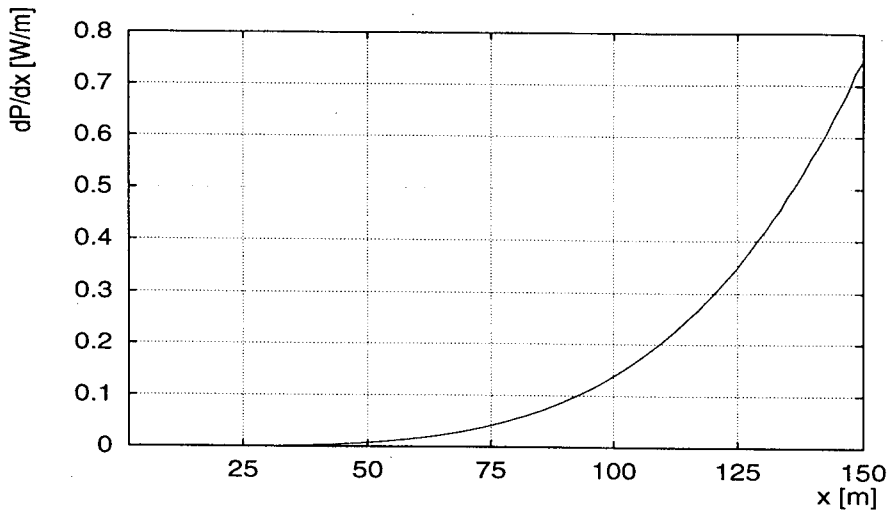

Figure 3.3: *The deposited power per unit length inside a helical undulator for the present TESLA beam parameters (i.e. 250 GeV particle energy, 8.2 MW beam power) and for* $K = 1$ *with* $B = 0.9$ *T,* $\lambda_u = 12$ *mm and an inner radius r=2.5 mm.*

(see fig.(3.2)) is roughly $\theta_{peak} = K/\gamma$. Hence the major fraction of the radiation will leave the undulator and only a small fraction of the energy will be deposited inside, if the condition

$$\frac{r}{L} \gg \frac{K}{\gamma} \tag{3.23}$$

is fulfilled (i.e. the opening angle of the radiation is small compared to the aperture of the undulator). Keeping the electron energy constant, the opening angle of the radiation is determined only by the undulator parameter K. The results in fig.(3.3) and fig.(3.4) are calculated for a magnetic field B of 0.9 T. The opening angle does not change, if the magnetic field is scaled by a factor of ζ and the undulator period by a factor $1/\zeta$. Then the deposited power in the undulator scales with the total radiated power which is given by

$$P_\gamma = \frac{e^4}{6\pi\epsilon_0 m_0{}^2 c} B^2\gamma^2. \tag{3.24}$$

Therefore fig.(3.3) and fig.(3.4) must be scaled with ζ^2 while the shapes of the curves remain constant.

For values of $K < 1$, the results shown in fig.(3.4) and fig.(3.3) do not change significantly. For K =0.5 and the same magnetic field strength, the maximum of of the power deposition per unit length at the end of the undulator is only 6.6 % lower than for K=1 (r=2.5 mm in both cases).

For values of $K > 1$, for example K=2 with parameters as above, the total deposited power rises only to P_{tot}=27 W (instead of $P_{tot} = 22$ W for K=1) The deposited power per unit length is almost the same as shown in fig.(3.3).

Decreasing the radius to 1.5 mm and choosing K=2, however, leads to a dramatic increase of the deposited power by almost a factor of two, compared to an undulator with a radius of 1.5 mm but an undulator parameter of K=1. In this case, the ratio r/L approaches K/γ and the fraction of radiated power deposited inside the undulator is no longer only from the very low energy tails, seen in fig.(3.2).

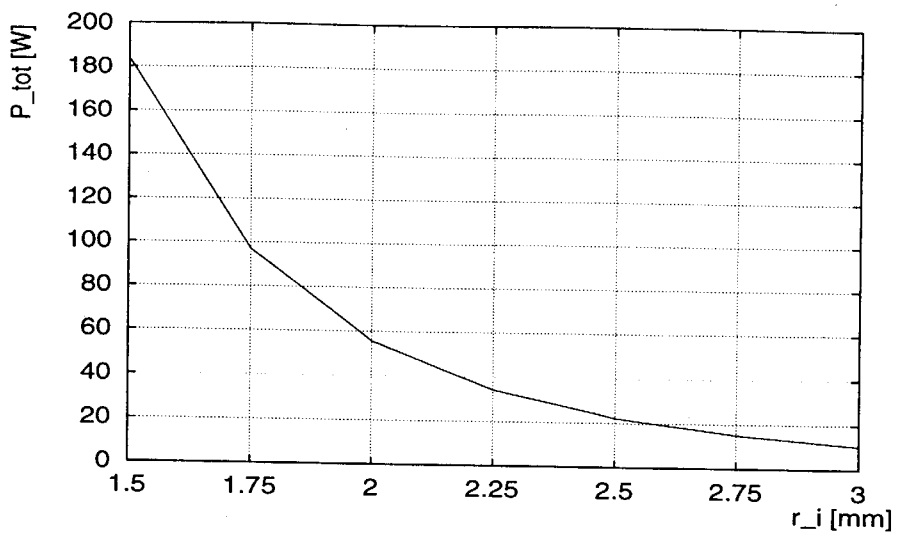

Figure 3.4: *Total deposited power inside a helical undulator as a function of the inner undulator radius. The calculations have been done using the present TESLA parameters and for K=1 with B=0.9 T and λ_u=12 mm.*

The previous simulations were done for the present TESLA beam parameters up-stream of the IP to estimate the amount of the power deposited inside a helical undulator. The results of more general calculations are presented in appendix A. The total deposited energy and the deposited energy per unit length of one single electron passing through an undulator is shown in fig.(A.1) to fig.(A.8) for different values of K. Since the operation of the positron source is also interesting at lower energies (down to 100 GeV), the calculations were done for different initial electron energies.

As mentioned above, the previous results are only valid for electron beams with negligible transverse beam diameters. To estimate the deposited power by a round gaussian beam with a non vanishing diameter, the total deposited power as a function of the inner undulator radius (shown in fig.(3.4)) was convoluted with a two dimensional gaussian density function:

$$\rho_t(r) = \frac{1}{2\pi\sigma^2} e^{-\frac{1}{2}\frac{r^2}{\sigma^2}}, \tag{3.25}$$

where r is the distance to the center of the beam and σ is the standard deviation. The beam with the radius $r_b \equiv \sigma$ was assumed to have no particles outside the distance of $r_b = 3\sigma$ from the longitudinal undulator axis. Hence, the deposited power as a function of the beam radius is calculated according to

$$P_{gauss}(\sigma) = \int_{\phi=0}^{\phi=2\pi} \int_{r_b=0}^{r_b=3\sigma} \rho_t(r_b) \cdot P_{tot}(r_i - r_b) \cdot r_b \, dr_b d\phi. \tag{3.26}$$

Substituting eq.(3.25) and integrating over ϕ leads to

$$P_{gauss}(\sigma) = \frac{1}{\sigma^2} \int_{r_b=0}^{r_b=3\sigma} e^{-\frac{1}{2}\frac{r_b^2}{\sigma^2}} \cdot P_{tot}(r_i - r_b) \cdot r_b \, dr_b, \tag{3.27}$$

where P_{tot} was approximated by linear functions over intervals of $\Delta r = 0.25$ mm in the range from 1.0 mm to 3.0 mm. The total deposited power as a function of the beam diameter is shown in fig.(3.5) for an undulator with an inner radius of $r_i = 2.5$ mm, an electron beam energy of 250 GeV, undulator strength of 0.9 T and a period length of 12 mm. At the maximum beam diameter of $\sigma = 0.5$ mm the deposited power is ≈ 90 W. This is roughly 4.5 times more than for a beam with $\rho_t(r) = \delta(r)$. If one scales the deposited power per unit length, shown in fig.(3.3) with this factor, the maximum of the deposited power per unit length at the end of the undulator is roughly 3.4 W/m which seems still to be reasonable.

More precise estimates of the deposited energy could be done by Monte-Carlo simulations. These numerical simulations have to take into account the initial phase space distributions at the beginning of the undulator and their propagation inside of it.

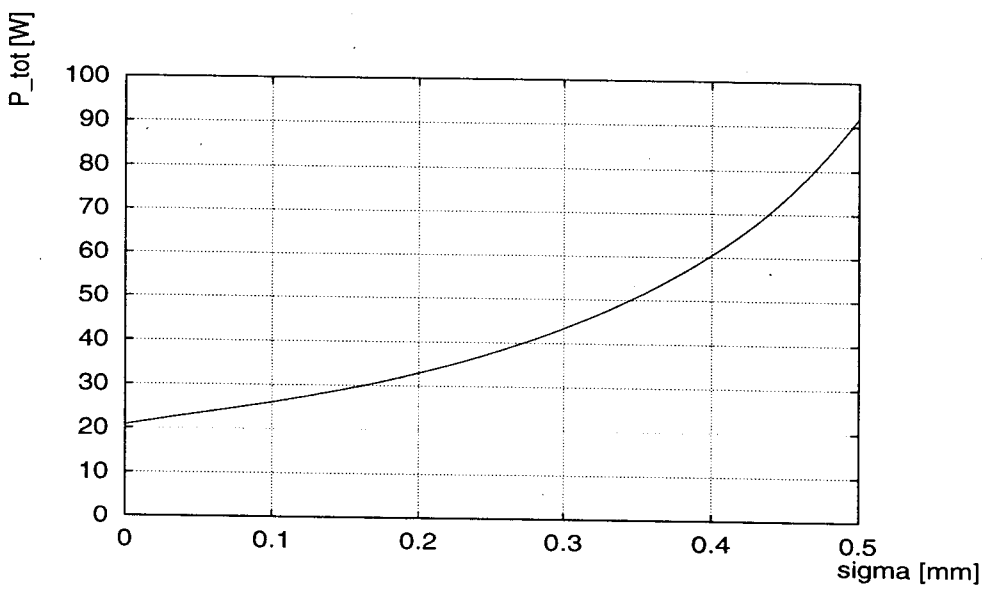

Figure 3.5: *Total deposited power inside a helical undulator as a function of the beam diameter* σ_{beam}. *The calculations have been done using the present TESLA parameters for K=1 with B=0.9 T and* λ_u*=12 mm. The inner radius of the undulator is 2.5 mm.*

Chapter 4

Particle tracking and simulations of photon emission

The realization of the positron source using the spent electron beam requires a simulation of the particle transport along the capture system and through the fields of the final focus quadrupoles, see section (8.1.2). Therefore a tracking program was developed which is able to simulate not only the particle transport described by the usual transport matrix multiplication but can also simulate the statistical process of quantum emission.

In a deflecting element the particles are accelerated perpendicular to their motion. If the deflecting magnetic field is approximately constant over the average length between two quantum emission processes, the emission spectrum is a dipole spectrum as explained in the previous chapter (3).

This condition is fulfilled for particle tracking through standard optical elements as being used in the spent beam capture system (see chapter (8)). The change of the magnetic field over the average emission length is small even in the strong final focus quadrupoles for TESLA. This is not the case for undulator radiation and emission processes during the beam-beam interaction at the interaction point (IP). Thus, in this case the simulation of photon emission requires a different treatment than that in the case of normal tracking through comparably smooth optical elements.

The photon emission in optical elements can be treated like the emission process on circular orbits with an instantaneous bending radius depending on the magnetic field at the position of the particle. The particles may emit photons at any position. For the simulation of the emittance growth due to quantum excitation it has to be ensured that only one photon is emitted per tracking step. This was done by choosing the tracking steps in each optical element (except for drift spaces) in such a way that the average number of emitted quanta per time-step was much less than one. The particle tracking along a beam line with n elements can be expressed by multiplying the initial particle vector $\vec{\mathbf{x}}_{ini,i}$ (with the elements x, x', y, y') gradually with the 4×4 element transfer matrixes $\widehat{M}_j$ according to

$$\vec{\mathbf{x}}_{fin,i} = \prod_{j=1}^{j=n} \widehat{M}_j \, \vec{\mathbf{x}}_{ini,i}. \tag{4.1}$$

Here i is the particle index and $\vec{\mathbf{x}}_{fin,i}$ the final particle vector. A general description of the matrix formalism can be found, for example, in the book by H.Wiedemann [Wie95]. The individual elements are divided into ν slices, i.e. ν elements of the same type with $1/\nu$ of the total length L, with $1/\nu$ of the total deflecting strength ϕ, but with the original quadrupole or

sextupole strength.

$$\vec{\mathbf{x}}_{fin,i} = \prod_{j=1}^{j=n} \prod_{k=1}^{k=\nu} \widehat{M}_{j,k}\, \vec{\mathbf{x}}_{ini,i}\,, \qquad \prod_{k=1}^{k=\nu} \widehat{M}_{j,k} = \widehat{M}_j. \tag{4.2}$$

After each matrix multiplication (except for drift spaces) the magnetic field B in the position of the particles was calculated from the matrix elements. From this, the instantaneous bending radius

$$\rho = \left(\frac{e}{p}B\right)^{-1} \tag{4.3}$$

and the critical energy $u_c = \hbar\omega_c$ are derived. According to M. Sands [Sands] the photon emission rate can be obtained from

$$\frac{d < n >}{dt} = \frac{5 \cdot \sqrt{3}}{6} \cdot \frac{r_e\, e_0\, c}{\hbar} \cdot B. \tag{4.4}$$

Together with the default step size Δs of $c \cdot \Delta t = L/\nu$ this leads to an average number of emitted photons per step of

$$< n >= \frac{1}{c} \frac{d < n >}{dt} \Delta s \tag{4.5}$$

which has to be much smaller than one. In this case the photon emission follows the Poisson distribution and the probability of the number of emitted photons k over one step is given by

$$P(k, < n >) = \frac{< n >^k}{k!} \cdot \exp(- < n >). \tag{4.6}$$

With a default number ν of 30 steps per element the maximum average number of emitted photons per step is typically less than 0.3. Hence the probability of emission of more than one photons per step is only

$$P(k \geq 2, < n >= 0.3) = 1 - P(k = 0 \vee k = 1, < n >= 0.3) = 3.7\%. \tag{4.7}$$

If $< n >$ was greater than 0.3 a message was printed and the tracking process was restarted with an increased number of steps per element, ν.

After computing $< n >$ after each step during the tracking, a random number $r \in [0, 1]$ was taken to decide if a photon was to be emitted in the step. The condition of photon emission was

$$r \leq P(k = 1, < n >). \tag{4.8}$$

In the case of quantum emission, the radiated energy in units of u/u_c was given by a random generator representing the photon number spectrum shown in fig.(3.1). The energy of the emitted photon was subtracted from the energy of the emitting particle. After this was done for all particles, the next tracking step was executed.

This method of simulating quantum emission was also used for the particle tracking through the off-axis final focus quadrupole fields after each step of the Runge-Kutta tracking. This will be explained in more detail in section (8.1.2) for the SBLC.

Chapter 5

Influence of a wiggler on an electron beam

The main subject of the present work is to study the feasibility of a positron source using the spent beam for photon production. As it will be shown in chapter (7), the beam behind the interaction point (IP) has a huge energy spread and large divergence. These properties make it difficult to built an achromatic capture system which provides a safe and stable operation of the positron source. In the case of the SBLC (see chapter (8.1.2)), the quality of the spent beam deteriorates due to the fields of the final focus quadrupoles of the oncoming beam. Due to the crossing angle at the IP, the spent beam passes through the final focus quadrupoles in a region in a region in which the magnetic field has higher order multipole components. Particularly the horizontal emittance is increased by these multipole components. For this reason, no arrangement has been found to realize a polarized positron source using the spent beam for the SBLC.

The problems mentioned above and described in more detail in the chapters (8) and (9.2) can be avoided by operating the positron source using the beam upstream of the IP. In this scheme it must be ensured that the wiggler or undulator does not deteriorate the beam quality unacceptably. In addition, the photon production necessary for the positron source requires a large amount of beam power. This could cause a considerable increase in the operating cost because the energy loss of the beam inside the wiggler or undulator has to be compensated by a higher initial beam energy. These problems will be studied in this chapter.

In the first section the effects of a helical undulator and an ideal wiggler, without manufacturing tolerances, will be studied. The second part of this chapter will treat the emittance growth inside planar wigglers due to manufacturing errors and the resulting dispersion which this generates.

5.1 Effects of a helical undulator and an ideal wiggler

Energy loss

The radiation loss of electrons in a wiggler or a helical undulator is given by [Jack83]:

$$P_\gamma = \frac{dE}{dt} = \frac{dE}{ds} \cdot c = \frac{e^4}{6\pi\epsilon_0 {m_0}^2 c} B^2 \gamma^2. \tag{5.1}$$

Hence it follows, with $\gamma = E/m_0c^2$, that the decrease of the relativistic factor $d\gamma$ per path length ds is

$$\frac{d\gamma}{ds} = -\frac{e^4}{6\pi\epsilon_0 m_0{}^3c^4}B^2\gamma^2 = -\Phi B^2\gamma^2 \quad \left(= \frac{P_\gamma}{m_0c^3}\right) \tag{5.2}$$

with

$$\Phi = \frac{e^4}{6\pi\epsilon_0 m_0{}^3c^4} = 6.466 \cdot 10^{-10}\ T^{-2}m^{-1}. \tag{5.3}$$

Integration of eq.(5.2) leads to the relativistic factor γ as a function of the longitudinal position s inside the wiggler

$$\gamma(s) = \frac{\gamma_0}{1 + \Phi\gamma_0 B_{rms}^2 s} \approx \gamma_0\left(1 - \Phi\gamma_0 B_{rms}^2 s\right) \tag{5.4}$$

where B_{rms} is the rms-value of the magnetic field along the wiggler according to

$$B_{rms}^2 = \frac{1}{\lambda}\int_0^\lambda B^2(\tilde{s})\,d\tilde{s}, \tag{5.5}$$

averaged over one wiggler period with length λ. Thus, for given wiggler parameters, the relation between the energy E_i at the entrance of the wiggler, the wiggler length L and the final energy E_f which is required for the experiments at the interaction point (IP) is

$$E_i = \frac{E_f}{1 - \frac{\phi}{m_0c^2}E_f B_{rms}^2 L}. \tag{5.6}$$

This result is only of interest when the positron source is operated before the IP because the spent beam is dumped after passing through the wiggler or the undulator.

Substituting values according to [Flt93] with a wiggler length of 35 m, $B = 1.7$ T and a final energy of 250 GeV, the required initial energy is 258.3 GeV. Thus, the operating energy has to be 3.31 % higher than the design energy at the IP. Concerning the energy loss these results are valid for both the wiggler and the helical undulator. The absolute value of the magnetic field B_0 does not change for the latter. Therefore B_{rms}^2 in eq.(5.4) has to be replaced by B_0^2. Taking the present values of $L = 100$ m and $B_0 = 0.9$ T for the polarized source, the energy at the entrance of the undulator has to be 2.63 % higher than the required energy of 250 GeV at the IP.

Energy spread due to the wiggler

Two competing processes have to be taken into account when estimating the energy spread generated by a wiggler [Ros91]. First we consider the energy loss as a classical process without statistical fluctuations. The energy loss per unit length inside as wiggler is expressed in eq.(5.2). For a particle with a different energy $\Delta E = m_0c^2\Delta\gamma$, eq.(5.2) can be rewritten to

$$\frac{d}{ds}(\gamma + \Delta\gamma) = -\Phi B^2(\gamma + \Delta\gamma)^2 \approx -\Phi B^2\gamma^2 - 2\Phi B^2\gamma\Delta\gamma, \tag{5.7}$$

if $|\Delta\gamma| \ll \gamma$. From this follows

$$\frac{d}{ds}(\Delta\gamma) = -2\Phi B^2\gamma\Delta\gamma. \tag{5.8}$$

The square of the energy deviation $(\Delta\gamma)^2$ can be derived from eq.(5.8):

$$\frac{d}{ds}(\Delta\gamma)^2 = 2\Delta\gamma\frac{d}{ds}(\Delta\gamma) = -4\Phi B^2\gamma(\Delta\gamma)^2. \tag{5.9}$$

The negative sign in eq.(5.9) shows, that the energy width would decrease along the wiggler if the statistical effects of the quantum emission did not exist.

The growth rate of the energy spread per unit length due to quantum emission can be expressed by [Sands]

$$\frac{d\sigma_E^2}{ds} = \frac{dn}{ds} < u^2 >= \frac{1}{c}\frac{dn}{dt} < u^2 >= \frac{55}{24\sqrt{3}c}u_c P_\gamma, \tag{5.10}$$

with the critical energy (see chapter 3)

$$u_c = \frac{3}{2}\frac{\hbar c\gamma^3}{\rho}. \tag{5.11}$$

Hence it follows, that

$$\frac{d\sigma_\gamma^2}{ds} = \frac{55}{24\sqrt{3}}\frac{u_c P_\gamma}{m_0^2c^5} = \frac{55}{16\sqrt{3}}\frac{\hbar e}{m_0^2c^2}\ \Phi B^3\gamma^4 = \Gamma\Phi B^3\gamma^4 \tag{5.12}$$

with the useful abbreviation

$$\Gamma = \frac{55}{16\sqrt{3}}\frac{e\hbar}{m_0^2c^2} = 4.4963\cdot 10^{-10}T^{-1}. \tag{5.13}$$

Replacing $\Delta\gamma^2$ in eq.(5.9) by the second order moment of the relativistic factor (i.e. σ_γ^2), the two competing effects of the radiative energy damping and the the quantum excitation lead to the inhomogeneous differential equation

$$\frac{d\sigma_\gamma^2}{ds} = \Gamma\Phi B^3\gamma^4 - 4\Phi B^2\gamma\sigma_\gamma^2. \tag{5.14}$$

This equation can be solved by the method of variation of constants. Hence the relative energy spread along the wiggler can be expressed by

$$\frac{\sigma_\gamma}{\gamma} = \frac{\gamma(s)}{\gamma_0}\sqrt{\Phi\Gamma B^3\gamma_0^2\cdot s + \left(\frac{\sigma_{\gamma_0}}{\gamma_0}\right)^2} \tag{5.15}$$

where γ_0 is the initial relativistic factor and σ_{γ_0} the initial energy spread at the beginning of the wiggler.

The growth of the energy spread as a function of the wiggler length is shown in fig.5.1 for a wiggler with $B = 1.7$ T and an electron energy E_{e^-} of 250 GeV (taking into account the different initial energy spread $\Delta E/E$ of $5\cdot 10^{-4}$ for TESLA and of $3.5\cdot 10^{-3}$ for the SBLC). Obviously the wiggler will increase the energy spread considerably particularly in the case of a low initial energy spread. For TESLA, the energy spread at the end of a 35 m long wiggler with the design strength B of 1.7 T is found to be 7 times higher than that at the entrance. Thus, one of the main advantages of TESLA, the very small energy spread of the particles, is lost in the case of operating the positron source upstream of the IP.

For the SBLC, the increase of the energy spread of ≈ 43 % is less than for TESLA. Since a crossing angle of 6 mrad at the IP is foreseen, the bunches have to be twisted around their vertical axis just before the interaction to avoid a luminosity loss. This will be realized by the so called "crab crossing" scheme, explained in section (8.1.2). The initial energy spread $\Delta E/E$ of $3.5 \cdot 10^{-3}$ is caused by an energy deviation of the particles which is correlated to their longitudinal position inside the bunch (the energy width in a infinitely small slice at a fixed longitudinal bunch position is roughly ten times less than the over-all energy spread). This fact, combined with a non-vanishing dispersion at the IP, permits bunch rotation providing the same luminosity as a head on collision. The energy diffusion induced by the wiggler destroys the correlated energy spread along the bunch. Thus increasing of the horizontal beam size and a loss of luminosity result. The design spot size at the IP and the contribution due to the uncorrelated energy spread add up quadratically (see eq.(5.17)). The dispersion at the IP has to provide a bunch rotation by half the crossing angle and can be calculated as follows:

$$D_{IP} = \frac{\sigma_s}{\sigma_E} \cdot \tan\left(\frac{\theta}{2}\right) = \frac{0.3\text{mm}}{3.5 \cdot 10^{-3}} \cdot \tan\left(3 \cdot 10^{-3}\right) = 0.26\text{mm}. \tag{5.16}$$

Here θ denotes the crossing angle at the IP, σ_E the correlated energy spread of all particles before the wiggler and σ_s the rms bunch length. With the dispersion, the effective horizontal rms beam size can be estimated:

$$\sigma_{x_{eff}} = \sqrt{\sigma_{x,\beta}^2 + D_{IP}^2 \sigma_{E,wigg}^2} = \sqrt{(333\text{nm})^2 + (0.26\text{mm} \cdot 0.0035)^2} = 956\text{nm}. \tag{5.17}$$

It follows, that the beam size increases by a factor 2.9 due to the wiggler induced uncorrelated energy spread. The luminosity decreases by the same factor which seems to be unacceptable.

The estimates concerning the growth of the energy spread are based on calculations according to [Sands]. These are valid for $K >> 1$ i.e. the case of wigglers. As shown in a report from E.L.Saladin et al. [Sal96], the energy diffusion is about 15 % higher in the case of a helical undulator for $K \approx 1$. This leads to an uncorrelated energy spread of 0.26 % (including the 15 %) for a helical undulator with B=0.9 T and a length of 100 m. The resulting growth of the beam size at the IP would still be 2.3 times higher than the design value.

Emittance growth due to periodic dispersion inside the wiggler

To a first approximation a wiggler can be considered as a sequence of alternating dipoles . The particle beam performs oscillations around the axis of the wiggler. To provide a maximum amplitude of the oscillation in the middle of one half period, the first poles of the wiggler have to be shorter than the subsequent ones. This is done by choosing the length of the first two alternating poles to be $\tilde{\lambda}_{1,2} = \lambda/\sqrt{32}$. The next pole has a length $\tilde{\lambda}_3$ of $\lambda/4$ with the same field as the second pole. Under the assumption that $\eta_x = \eta_x' = 0$ at the entrance of the wiggler, a periodic dispersion is created which leads to a horizontal emittance growth due to quantum excitation. The maxima of the dispersion and its derivative are given by

$$\hat{\eta_x'} = \frac{\lambda}{4\rho} = \frac{e}{4p}\lambda B, \quad \hat{\eta_x} = \frac{(\lambda/4)^2}{2\rho} = \frac{e}{32p}\lambda^2 B, \tag{5.18}$$

where p is the particle momentum. The emittance growth rate is [Sands] and [Ros91]:

$$\frac{d\varepsilon_x}{ds} \approx \frac{1}{2}\Gamma\Phi\gamma^2(s)\,|B|^3\,\mathcal{H}_x(s), \tag{5.19}$$

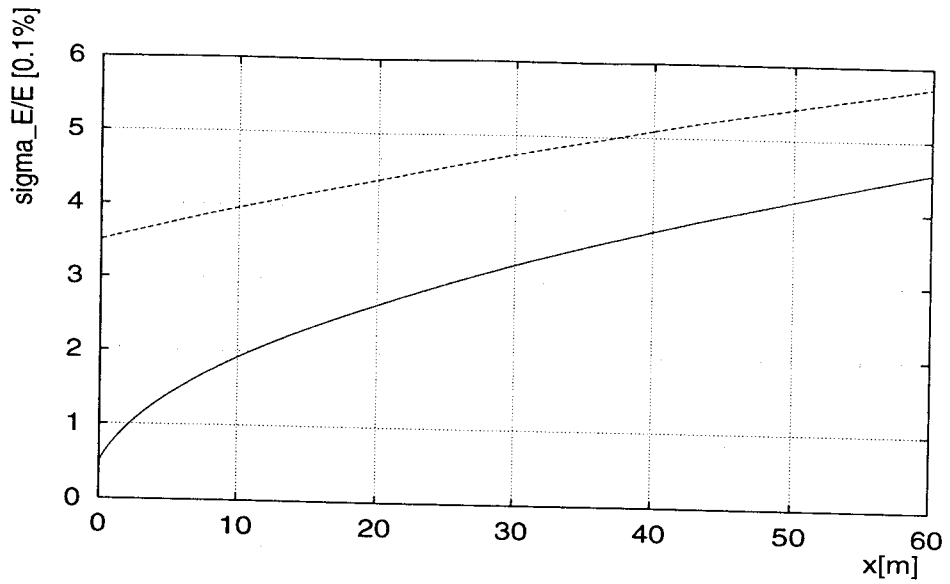

Figure 5.1:
Growth of the energy spread inside a wiggler with B=1.7 T for both linear colliders. The initial energy spread at the beginning of the wiggler was assumed to be $5 \cdot 10^{-4}$ *for TESLA (lower curve) and* $3.5 \cdot 10^{-3}$ *for the SBLC (upper curve).*

with

$$\mathcal{H}_x(s) = \frac{1}{\beta_x}\left(\eta_x^2 + (-\beta_x'\eta_x/2 + \beta_x\eta_x')^2\right). \tag{5.20}$$

Assuming that $\beta_x \approx$ const. along the wiggler and $\eta_x^2/\beta_x \ll \beta_x\eta_x'^2$ (i.e. $\lambda << \beta_x$ inside the wiggler) then

$$\mathcal{H}_x(s) \approx \beta_x(s)\,\eta_x'^2(s). \tag{5.21}$$

Since the β-function is almost constant over one period length λ it follows from eq.(5.19) that

$$\frac{d\varepsilon_x}{ds} \approx \frac{1}{2}\Gamma\Phi\gamma^2|B|^3\beta_x(s)\,\eta'^2{}_{x_{rms}}. \tag{5.22}$$

Due to the first three wiggler poles which are shorter than the other, the dispersion can be treated as a sine-like trajectory inside the wiggler. Then the rms-value of η'_x, following a cosine-like trajectory, can be calculated according to

$$\eta'^2{}_{x_{rms}} = \frac{1}{\lambda}\int_0^{\lambda}\eta_x^2(s)\,ds = \frac{4}{\lambda}\int_0^{\frac{\lambda}{4}}\eta_x^2(s)\,ds = \frac{4}{\lambda}\int_0^{\frac{\lambda}{4}}\left(\hat{\eta}_x' - \frac{s}{\rho}\right)^2 ds = \frac{e^2}{48m_0^2c^2\gamma^2}\lambda^2B^2, \tag{5.23}$$

where $\rho = \frac{e}{p}B$ is the bending radius inside the wiggler . Substituting this result into eq.(5.22) leads to

$$\frac{d\varepsilon_x}{ds} \approx \frac{\Gamma\Phi e^2}{96\,m_0^2c^2}\lambda^2|B|^5\beta_x(s) \tag{5.24}$$

Integrating over the wiggler length L, it follows that

$$\Delta\varepsilon_x(L) = \frac{\Gamma\Phi e^2}{96\,m_0^2c^2}\lambda^2|B|^5\int_0^L\beta_x(\tilde{s})d\tilde{s}. \tag{5.25}$$

With regard to the horizontal β-function the wiggler can be treated as a drift space. Then, with initial conditions $\alpha_{x_0}, \beta_{x_0}, \gamma_{x_0}$, the β-function along the wiggler is given by

$$\beta_x(s) = \beta_{x_0} - 2\alpha_{x_0} s + \gamma_{x_0} s^2 \tag{5.26}$$

and the evaluation of the integral in eq.5.25 yields

$$\Delta\varepsilon_x(L) = \frac{\Gamma\Phi e^2}{96\, m_0^2 c^2} \lambda^2 |B|^5 \left[\beta_{x_0} L - \alpha_{x_0} L^2 + \frac{1}{3}\gamma_{x_0} L^3\right]. \tag{5.27}$$

This result, valid for arbitrary initial conditions, can be simplified for a quick estimate of the emittance growth. The initial optical functions are set to $\beta_{x_0} = L$ and $\alpha_{x_0} = 1$ and so the β-functions are symmetric with respect to the center of the wiggler. Hence it follows, with $\gamma_{x_0} = (1 + \alpha_{x_0}^2)/\beta_{x_0} = 2/L$ from eq.(5.27), that

$$\Delta\varepsilon_x(L) = \frac{\Gamma\Phi e^2}{96\, m_0^2 c^2} \lambda^2 |B|^5 \cdot \frac{2}{3} L^2 = \frac{\Gamma\Phi e^2}{144\, m_0^2 c^2} \lambda^2 |B|^5 L^2. \tag{5.28}$$

With $B = 1.7$ T, $\lambda = 50$ mm and $L = 35$ m, the horizontal emittance growth is

$$\Delta\varepsilon_x = 2.95 \cdot 10^{-8} \text{ mm mrad}. \tag{5.29}$$

Thus, the contributions to the emittance growth due to the periodic dispersion in an ideal wiggler are negligible.

5.2 Influence of manufacturing tolerances

Until now an ideal wiggler has been assumed. Manufacturing errors prevent the dispersion canceling from period to period. Errors in the magnetic pole strength and in the lengths of the half-periods can cause a growth of the horizontal dispersion. Photon emission in dispersive regions, however, lead to an increase of the emittance. Therefore these effects must be studied to ensure a sufficiently low beam emittance at the interaction point. Twists of the magnetic poles are also possible. This would lead to vertical dispersion and an increase in the vertical emittance. In the following calculations the effects of coupling between the horizontal and vertical planes (for example due to octupole terms) have not been considered because the gap height g is much smaller than the period length λ. In this case the wiggler can be treated as a sequence of alternating dipoles, each with length $\lambda/2$. The horizontal transfer matrix per half period is then

$$\mathbf{M}_{\lambda/2} = \begin{pmatrix} \cos\chi & \rho\sin\chi & \rho(1-\cos\chi) \\ -\frac{1}{\rho}\sin\chi & \cos\chi & \sin\chi \end{pmatrix} \approx \begin{pmatrix} 1 & \lambda/2 & 0 \\ 0 & 1 & \lambda/2\rho \end{pmatrix} \tag{5.30}$$

using $|\chi| = \left|\frac{\lambda}{2\rho}\right| \ll 1$ and $1/\rho^2 \ll 1$. The horizontal dispersion and its derivative after the half period $(i+1)$ are given by

$$\begin{aligned} \eta_{x_{i+1\lambda/2}} &= \eta_{x_{i\lambda/2}} + \tfrac{\lambda}{2}\eta'_{x_{i\lambda/2}}, \\ \eta'_{x_{i+1\lambda/2}} &= \eta'_{x_{i\lambda/2}} + \tfrac{\lambda}{2\rho}. \end{aligned} \tag{5.31}$$

The standard deviations of the wiggler strength and the period length due to manufacturing errors are called $\sigma_B$and σ_λ. Hence the standard deviation in the error kicks of the dispersion (i.e. $< \Delta\eta_x'^2 >$) can be obtained as follows:

$$\begin{aligned}\sigma_{\eta_x'} &= \tfrac{e}{2p}\sqrt{\left(\tfrac{\partial}{\partial B}\lambda B\right)^2\sigma_B^2 + \left(\tfrac{\partial}{\partial\lambda}\lambda B\right)^2\sigma_\lambda^2} \\ &= \tfrac{e}{2p}\sqrt{\lambda^2\sigma_B^2 + B^2\sigma_\lambda^2} \\ &= \tfrac{e}{2p}\lambda B\sqrt{\delta_B^2 + \delta_\lambda^2}\end{aligned} \tag{5.32}$$

where the relative deviations are $\delta_B = \frac{\sigma_B}{B}$ and $\delta_\lambda = \frac{\sigma_\lambda}{\lambda}$.

These errors are uncorrelated and the rms-value of η_x' after i half periods is proportional to $\sqrt{i}$. When $i = 2s/\lambda$, it follows that

$$\eta'_{x_{rms}}(s) = \frac{e}{p}\, B\, \sqrt{\frac{\lambda}{2}\left(\delta_B^2 + \delta_\lambda^2\right)}\ \ \sqrt{s} \tag{5.33}$$

and

$$\eta_{x_{rms}}(s) = \frac{2}{3}\,\frac{e}{p}\, B\, \sqrt{\frac{\lambda}{2}\left(\delta_B^2 + \delta_\lambda^2\right)}\ \ \sqrt{s^3}. \tag{5.34}$$

This analytic result is compared with results from tracking simulations for a wiggler magnet with relative manufacturing deviations in δ_λ and δ_B of 1%. This is comparable to present manufacturing accuracies. The dispersion has been calculated along the wiggler by matrix multiplication following eq.(5.30) with randomly distributed values of λ and B. The comparison between the analytical estimates and the simulation shows good agreement. Equations (5.33) and (5.34) have been used to make predictions about the emittance growth due to such manufacturing errors. In this first approach the energy loss inside the wiggler has been neglected. A mean $\bar{\beta}_x$ was taken and α_x was assumed to be zero inside the wiggler, leading to

$$\mathcal{H}_x \approx \frac{\eta_x^2}{\bar{\beta}_x} + \bar{\beta}_x\eta_x'^2 \tag{5.35}$$

which yields, together with eq.(5.19),

$$\Delta\varepsilon_x(s) = \frac{1}{2}\Gamma\Phi\gamma_0^2\,|B|^3\int_0^L \mathcal{H}_x(\tilde{s})d\tilde{s}. \tag{5.36}$$

Substituting eq.(5.33) and eq.(5.34) one obtains after integration

$$\Delta\varepsilon_x(s) = \frac{e^2\lambda}{4p^2}B^5\ \left(\delta_B^2 + \delta_\lambda^2\right)\ \Gamma\Phi\gamma_0^2\ \left(\frac{L^4}{9\bar{\beta}_x} + \frac{\bar{\beta}_x L^2}{2}\right). \tag{5.37}$$

Taking, for example, the design values for the unpolarized source with a length L of 35 m (which is not optimized for use upstream of the IP) one gets, with $\delta_\lambda = \delta_B = 1\%$ and $\bar{\beta}_x = 35$ m, an emittance growth $\Delta\varepsilon_x$ of $9 \cdot 10^{-8}$ mm mrad. This contribution is negligible compared to the horizontal design emittance.

Horizontal field components arise if the magnetic poles are twisted around the longitudinal wiggler axis. They create a vertical dispersion according to eq. (5.31). Since the pitch angle ϕ of the poles is much smaller than unity, it follows that for the horizontal field

$$B_H = B\sin\phi \approx B\cdot\phi. \tag{5.38}$$

The dispersion kick per half period is then

$$\Delta\sigma_{\eta'_y} = \frac{e}{2p} B\lambda\phi, \tag{5.39}$$

and the standard deviation for the vertical derivative of the dispersion η'_y can be obtained from

$$\begin{aligned}\sigma_{\eta'_y} &= \tfrac{e}{2p}\sqrt{\left(\tfrac{\partial}{\partial B}\lambda B\phi\right)^2\sigma_B^2 + \left(\tfrac{\partial}{\partial\lambda}\lambda B\phi\right)^2\sigma_\lambda^2 + \left(\tfrac{\partial}{\partial\phi}\lambda B\phi\right)^2\sigma_\phi^2} \\ &= \tfrac{e}{2p}\sqrt{\lambda^2\phi^2\sigma_B^2 + B^2\phi^2\sigma_\lambda^2 + B^2\lambda^2\sigma_\phi^2} \\ &= \tfrac{e}{2p}\sigma_\phi\lambda B\sqrt{1+\delta_B^2+\delta_\lambda^2},\end{aligned} \tag{5.40}$$

where ϕ^2 is replaced by σ_ϕ^2. Following the same reasoning which led to eqs. (5.33) and (5.34), one obtains

$$\eta'_{y_{rms}}(s) = \frac{e}{p}\, B\sigma_\phi \sqrt{\frac{\lambda}{2}(1+\delta_\lambda^2+\delta_B^2)}\ \sqrt{s} \tag{5.41}$$

$$\eta_{y_{rms}}(s) = \frac{2e}{3p}\, B\sigma_\phi \sqrt{\frac{\lambda}{2}(1+\delta_\lambda^2+\delta_B^2)}\ \sqrt{s^3} \tag{5.42}$$

This result can be used together with eq.(5.19) to determine the vertical emittance growth.

$$\Delta\varepsilon_y(L) = \frac{e^2\lambda}{4p^2}|B|^5\sigma_\phi^2\left(1+\delta_\lambda^2++\delta_B^2\right)\Gamma\Phi\gamma_0^2\left(\frac{L^4}{9\bar{\beta}_y}+\frac{\bar{\beta}_y L^2}{2}\right), \tag{5.43}$$

After substituting the same values as for the horizontal emittance growth, with an additional $\sigma_\phi = 1$ mrad, one obtains a vertical emittance increase of

$$\Delta\varepsilon_y = 6.6\cdot 10^{-9}\ \text{mm mrad}. \tag{5.44}$$

The vertical emittance growth by roughly 1 % of the design value can be neglected.

In summary one can say that the energy spread due to quantum emission is the dominating phenomena in deterioration of the beam quality. For TESLA the initially very small energy spread is increased by a factor of almost 7. For the SBLC a correlation between the energy and the longitudinal position inside the bunch is needed for the crab crossing. This correlation is destroyed by the wiggler. Thus, in the case of the SBLC the energy spread would lead to an increase of the beam size at the IP and to a loss of luminosity.

Chapter 6

Operation of a wiggler-based positron source at low energies

The investigations of positron sources in [Flt93] were made for a design energy of the electron beam of 250 GeV. During the commissioning of the linac and for operating the linac at lower center of mass energies it is necessary to know the minimum possible electron energy which can be used to drive a wiggler-based positron source. The parameters for the positron source are based on the requirement that one electron has to produce at least one positron accepted by the injector linac. In the work of K.Floettmann, the parameters have been chosen such that a safety factor of 2 is foreseen in the positron production [Flt93]. In order to estimate the optimum wiggler parameters and the feasibility of low energy operation of the positron source, numerous coupled effects have to be taken into account. The consequences of varying individual parameters on the net positron yield are difficult to predict.

1. The positron yield per wiggler unit length and per electron $\mathcal{Y}_{e+}$ depends on the number and the average energy E_γ of the photons produced inside the wiggler. As explained in chapter (3) the photon emission rate $\mathcal{N}_\gamma$ depends on the magnetic field strength B.

   The photons are focused on a thin target at a certain distance behind the wiggler where they are converted into e^+e^- pairs. The number of positrons which leave the target can be obtained by integration of the positron energy spectrum

$$\frac{N_{e+}}{dE}(E) = \int_E^\infty \frac{dN_\gamma}{d\tilde{E}} \frac{1}{\tilde{E}} S\left(\tilde{E}\right) d\tilde{E} \cdot t, \tag{6.1}$$

   in which t is the target thickness in units of radiation length and $S(E)$, defined in [Flt93], represents the probability for positron production per radiation length as a function of the photon energy: The total number of positrons can be obtained by integrating eq.(6.1)

$$\begin{aligned} S(E) &= 0 && \text{for } E \leq 1.6 \text{ MeV} \\ S(E) &= 0.14 \ln\left(1.5 E_{[MeV]}\right) - 0.117 && \text{for } 1.6 \text{ MeV} \leq E \leq 400 \text{ MeV} \\ S(E) &= \tfrac{7}{9} && \text{for } E > 400 \text{ MeV} \end{aligned}$$

   over all energies. It follows that

$$\mathcal{Y}_{e+} = \int_{E=0}^\infty \frac{N_{e+}}{dE} dE. \tag{6.2}$$

The number of positrons produced per meter of wiggler and per electron is shown as a function of the electron energy for different wiggler strengths in fig.(6.1). The satu-

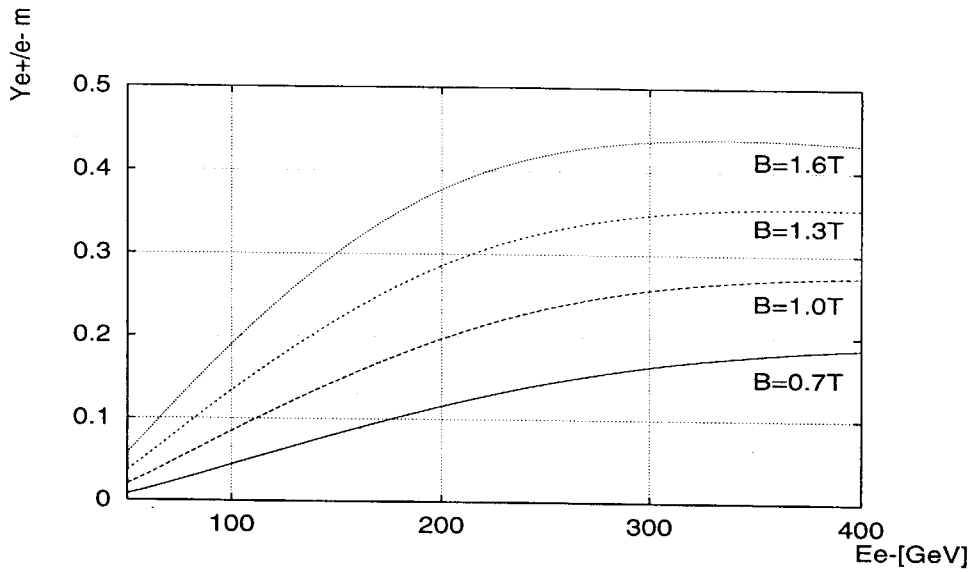

Figure 6.1: *Total number of positrons per unit length of wiggler produced in a thin target* $(0.4X_0)$ *as a function of the electron energy* E_{e^-} *for different wiggler strengths* $B = 0.7, 1.0, 1.3, 1.6\ T$.

ration of the positron yield at high e^- energy is a result of the constant cross section of pair production at photon energies above 400 MeV. For a given wiggler strength B, the critical energy (and the maximum of the power spectrum plotted in fig.(3.1)) of the radiation grows with the second power of the relativistic factor. The positron yield grows with the electron energy until the emitted photon power below 400 MeV is very small. Subsequently an increase of the electron energy causes only a negligible growth of the positron yield although the photon energy is rising.

2. Behind the target the positrons are collected in a capture section consisting of a solenoid and guided into the first accelerating structure. The efficiency η_c of this capture system depends on the photon beam spot size Δ at the conversion target. The capture efficiency as a function of spot size has been estimated in [Flt93] using the **EGS4** shower simulation program. The result can be parameterized with a third order polynomial

$$\eta_c\left(\Delta_{[mm]}\right) = 0.2147 + 0.00755\Delta_{[mm]} - 0.0851\Delta^2_{[mm]} + 2.748\ 10^{-9}\Delta^3_{[mm]}, \qquad (6.3)$$

which is plotted in fig.(6.2). The photon spot size depends on the wiggler length L and the distance D between wiggler and target. The spot size on the target results from a superposition of the radiation produced along the path through the wiggler, at different distances from the target. Furthermore the spot size depends on the electron energy, the wiggler strength and on the period length λ. The periodic orbit of the electrons inside the wiggler is determined by the period length and the wiggler strength. The maximum deflection angle is

$$\phi_{max} = \frac{\dot{e}}{4p}\lambda B. \qquad (6.4)$$

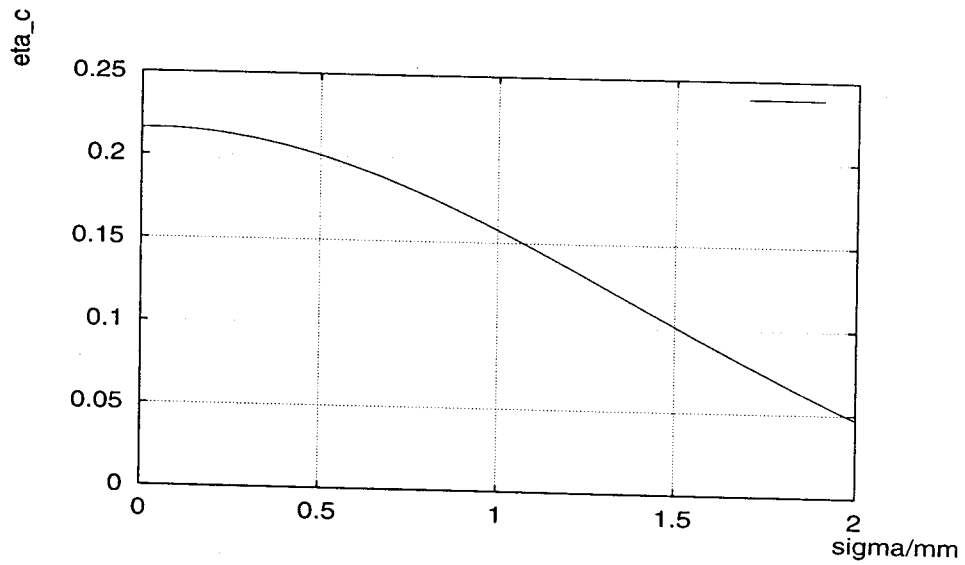

Figure 6.2: *Efficiency of the positron capture optics behind the target as a function of the radiation spot size* Δ.

An increased wiggler strength leads to a higher positron yield in the target but to a lower capture efficiency due to the larger spot size. A higher electron energy would increase the capture efficiency and also the positron yield.

3. From eq.(6.4) it follows that the period length has to be as short as possible to provide a small radiation spot size on the conversion target. The wiggler is built using hybrid technology, i.e. the wiggler consists of a combination of permanent magnets and iron poles. The period length and the gap height of the wiggler affects its field strength in a way which has been parametrized in [Hal83]:

$$B_{max} = 3.33 \exp\left(-\frac{g}{\lambda}\left[5.47 - 1.8\frac{g}{\lambda}\right]\right), \quad 0.07 \leq g/\lambda \leq 0.7. \tag{6.5}$$

Thus, the period length for a certain wiggler strength can be estimated by inverting eq.(6.5). With $B_{rms} = \frac{1}{\sqrt{2}} B_{max}$ one gets

$$\lambda_B = \frac{g}{1.52 - \sqrt{2.31 + 0.56 \ln\left(0.42 B_{rms}\right)}}. \tag{6.6}$$

Fig.(6.3) shows the dependence of the period length λ_B as a function of the required rms-wiggler strength for a fixed gap height of $g = 4$ mm. Hence it follows that an increased wiggler strength (which would lead to a higher positron yield inside the target) is related to a longer period length and finally to a lower η_c.

To investigate the feasibility of operation of the positron source at low energies the total positron yield is estimated as follows:

The separation region in which the photon beam is separated from the electron beam, i.e. the distance D from the end of the wiggler to the target, has been chosen to be as short as

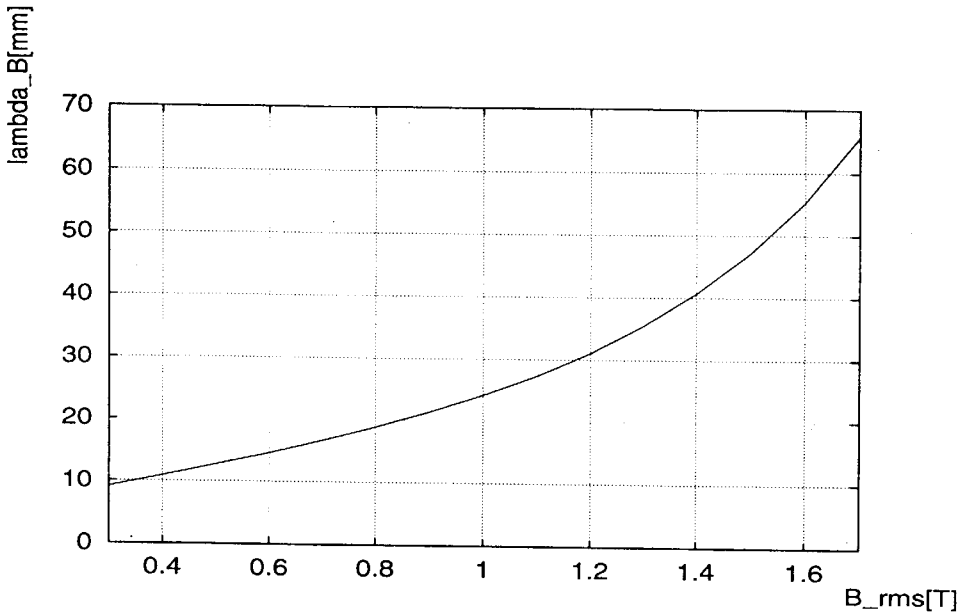

Figure 6.3: *Required period length as a function of a given wiggler strength B_{rms} from the inverted Hallbach parametrization with a gap height of 4 mm.*

possible but long enough to provide a clean beam separation. A value of $D = 50$ m has been chosen for all the following calculations.

The gap height g should be as small as possible to minimize the period length for a given wiggler strength and should leave enough space for the beam and the vacuum pipe. A value of 4 mm was chosen.

The calculations are made for rms wiggler strengths B_{rms} of 0.7, 1.0, 1.3, and 1.6 T, and the electron energy in the range of 50...400 GeV Then the maximum positron yield $\mathcal{Y}_{e^+_{max}}$ is calculated starting from the end of the wiggler:

The wiggler (with a still unknown length) is assumed to consist of identical parts each one meter in length. The spot size of the radiation in this part is estimated. The radiation spot size on the target is used to determine the capture efficiency η_C for the positrons produced by the first wiggler part. The product of the capture efficiency with the number of positrons per electron per meter wiggler $\eta_C \cdot \mathcal{Y}_{e^+}$ yields the contribution of this first wiggler part to the entire positron yield. Then further parts are added. Their contributions to the positron yield are calculated in the same way as for the first meter of the wiggler. From a certain point on, a longer wiggler does not make sense anymore because the radiation spot size on the target increases with the distance to the target. Then, since the capture efficiency decreases, the growth of the total positron yield is negligible while only the heat load on the target increases. The maximum yield of positrons per electron along the length of the wiggler $\mathcal{Y}_{e^+_{max}}$ can be expressed by

$$\mathcal{Y}_{e^+_{max}}(E_{e^-}, B_{rms}) = \mathcal{Y}_{e^+}(E_{e^-}, B_{rms}) \cdot \int_{D}^{L_{wigg}+D} \eta_c(\Delta(\tilde{s}))\, d\tilde{s}, \tag{6.7}$$

where $\mathcal{Y}_{e^+}(E_{e^-}, B_{rms})$ is the electron yield per electron per meter of wiggler depending on the electron energy E_{e^-} and the wiggler strength B. L_{wigg} is the wiggler length for which the spot size on the target has increased such that the capture efficiency for this part of the wiggler has decreased to 5 %.

$$\eta_c(\Delta(L_{wigg} + D)) = 5\% \Leftrightarrow \Delta(L_{wigg} + D) = 2\text{mm}. \tag{6.8}$$

It is assumed that no benefit can be obtained from extending the wiggler further as the ratio of the positron yield to the heat load inside the target then becomes less and less attractive and eventually intolerable.

The maximum positron yield per electron and the corresponding wiggler lengths are shown in fig.(6.4) and (6.5), respectively. One can see that it is possible to drive the source with a beam energy of roughly 100 GeV. The corresponding wiggler length would be around 280 m with a magnetic field of 0.7 T. This design would lead to a safety factor of two in the stability of the positron production, i.e. that one electron passing through such a wiggler would produce two positrons. The most reasonable choice at this energy is a roughly 100 m long wiggler with an rms-strength of 1.0 T, resulting in a yield of 1.2 positrons per electron. This should be enough to ensure a reliable operation. If the number of 1.2 positrons per electron were to be required as a lower limit for positron production, then is concluded that there would be no solution for $E_{e^-} \leq 100$ GeV with B > 1.0 T.

The results from this chapter have been calculated for a fixed distance $D = 50$ m between the end of the wiggler and the target. The electrons must be separated carefully from the photon beam along this region to avoid a deterioration of the beam quality. However, this is only important in the case of operation of the source upstream from the IP.

As described in more detail in chapter (8), the beam after the IP has to be captured and transported to the wiggler, faking into consideration the wiggler-specific emittance requirements. This is not possible for the whole beam but, as will be shown later, for roughly 85 % of the particles. If the positron yield for that spent beam capture efficiency shall be estimated from the previous calculations, the effective positron yield per electron shown $\mathcal{Y}_{e^+_{max}}$ in fig.(6.4) has to be multiplied with a factor of 0.85 by keeping the same corresponding wiggler length shown in fig.(6.5). An operation of the wiggler-based positron source at low energies then would be more difficult.

However, the spent beam will be dumped after passing through the wiggler. Therefore the separation length can be chosen as short as possible because there is no need to take the beam properties into account. A sufficient separation of 0.3 m can be realized over a distance D of 18.25 m with a magnetic field B of 1.5 T. Since the spot size on the target is proportional to D, the effect of the lower positron yield from the spent beam is compensated by the higher efficiency of the positron capture optics η_c behind the target.

In conclusion, a reasonable lower limit for the operating energy of the collider with a full e^+-intensity is given by $E_{cm} \geq 200$ GeV.

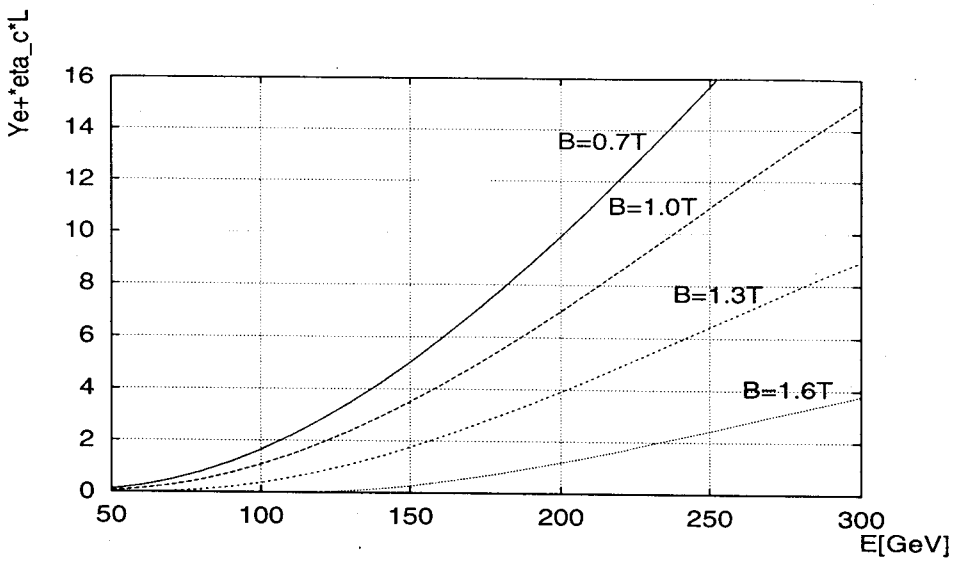

Figure 6.4: *Maximum positron yield per electron as a function of incident electron energy for rms wiggler strengths B_{rms} of 0.7, 1.0, 1.3 and 1.6 T. The lower fields seem to be advantageous on a first sight, but they are connected with unrealistic wiggler lengths, see fig.(6.5).*

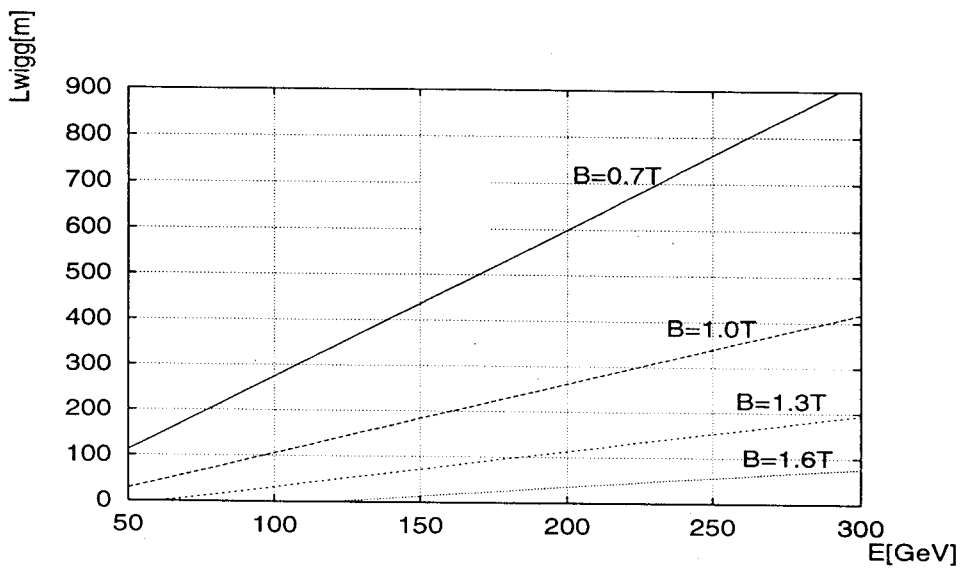

Figure 6.5: *Wiggler length corresponding to the maximum positron yield shown in fig 6.4 as a function of the electron energy for rms wiggler strength B_{rms} of 0.7, 1.0, 1.3, 1.6 T.*

Chapter 7

Beam properties behind the interaction point

For the realization of a positron source operating with the spent beam it is essential to investigate the beam properties behind the interaction point (IP). During the collision, the beam properties change dramatically because the particles are deflected by the strong electromagnetic forces of the opposing beam. In the first part of this chapter the disruption effect and the horizontal phase space distribution will be described. In the second section the energy distribution after the interaction due to beamstrahlung will be discussed.

7.1 Disruption

Depending on the bunch charge, the rms-beam extensions σ_x, σ_y and on the bunch length σ_s, the beam particles can either be deflected smoothly during the interaction or actually perform oscillations around the longitudinal bunch axis. The latter effect is called disruption and can be quantified by the so-called disruption parameter defined by R.Hollebeek[Hol81]

$$D_{x,y} = \frac{2r_e N \sigma_s}{\gamma \sigma_{x,y} (\sigma_x + \sigma_y)}, \tag{7.1}$$

where N is the number of particles per bunch, $r_e = e^2/4\pi\epsilon_0 m_e c^2$, the classical electron radius and γ the relativistic factor. The value for the horizontal disruption parameterD_x is ≈ 0.3. The vertical disruption parameter D_y is 17.5 for TESLA and 6.6 for the SBLC based on the present parameters at the IP. For $D < 1$, the particles are weakly deflected during the interaction but as D increases the particles perform sine-like oscillations around the longitudinal bunch axis. The deflection during the interaction causes a broadening of the angular distribution. The maximum disruption angle $\hat{\Theta}$ has been estimated numerically as a function of the beam parameters by K.Yokoya and P.Chen [Yok91]. For flat beams $\hat{\Theta}$ can be expressed by

$$\hat{\Theta}_{x,y} = \frac{2r_e N}{\gamma \sigma_x} \frac{k_{x,y}}{\sqrt[6]{1 + \left(\frac{D_{x,y}}{2}\right)^5}}, \tag{7.2}$$

where the parameters $k_x \approx 0.75$ and $k_y \approx 1.25$. The beam size remains nearly constant or even decreases due to the focusing pinch effect. This leads to an increase of the luminosity which can be expressed by the luminosity enhancement factor $H_D = L/L_0$ which is usually in the range between 1 and 2 for the next generation of linear colliders. Numerical calculations for

beam-beam phenomena in linear colliders have been carried out by [Yok91]. For the following investigations presented here data sets of 12000 particles were created with a beam-beam simulation program by R. Brinkmann [Bri92] using the parameters at the interaction point (IP). Shown in figs.(7.1) and (7.2) are the phase space distributions in both the horizontal and vertical planes for TESLA and for the SBLC. The different shapes are due to the flatness of the beam and can be explained by the change in the electromagnetic force as a function of the

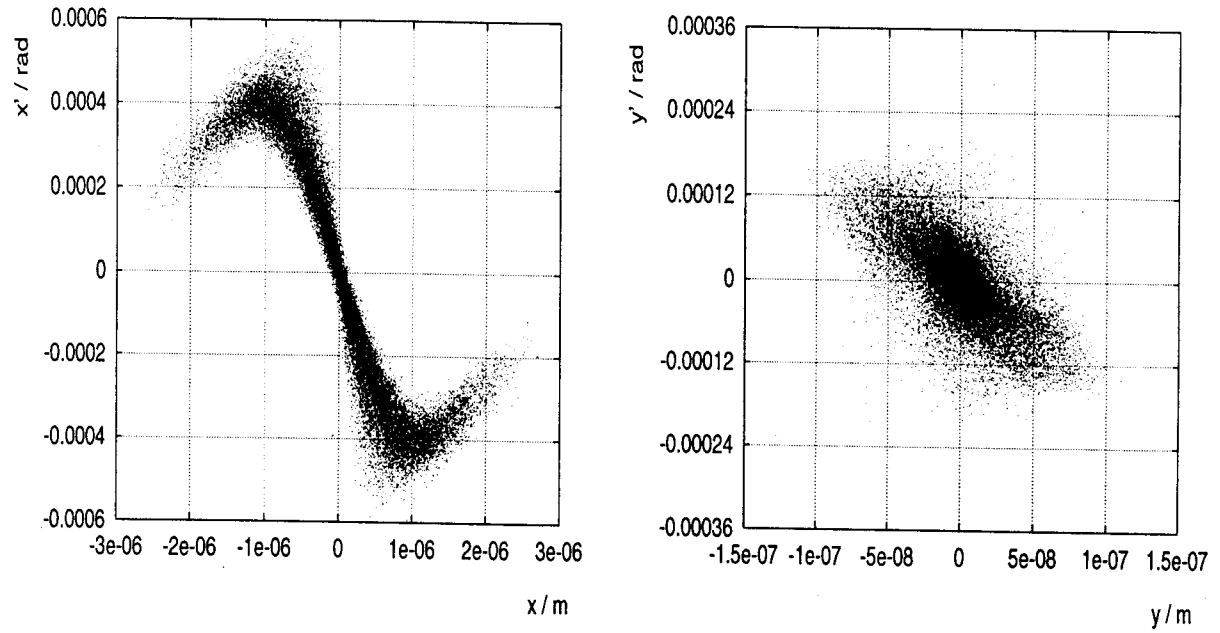

Figure 7.1: *Horizontal and vertical phase space distributions behind the interaction point of TESLA.*
Left: Horizontal phase space. Particles on-axis are not deflected by the oncoming beam. The deflection increases with the distance to the bunch center due to the net electromagnetic force. After a maximum has been reached, the kick strength decreases with increasing distance.
Right: Vertical phase space. Since the beams are flat, the vertical kick decreases for $y \approx \sigma_x \gg \sigma_y$ *only. At these amplitudes the population is negligible. Therefore the vertical phase space distribution does not exhibit the S-shape seen in the horizontal plane.*

distance from the bunch center, as calculated in [Yok91]. It has been found for flat beams with $\sigma_y \ll \sigma_x$, that the electromagnetic force as a function of the distance to the bunch center can be expressed by

$$F_x(x) \propto -\frac{1}{\sigma_x} e^{\frac{-x^2}{2\sigma_x^2}} \int_0^{\frac{x}{\sigma_x}} e^{\frac{\tilde{x}^2}{2}} d\tilde{x}, \tag{7.3}$$

and

$$F_y(x,y) \propto -\frac{1}{\sigma_x} e^{\frac{-x^2}{2\sigma_x^2}} \int_0^{\frac{y}{\sigma_y}} e^{-\frac{\tilde{x}^2}{2}} d\tilde{x}, \quad |y| \ll \sigma_x. \tag{7.4}$$

The horizontal component of the electromagnetic force is plotted as a function of the horizontal distance from the bunch axis in fig.(7.3). During the bunch crossing the beam particles receive kicks whose strength is related to the strength of the electromagnetic force. The force depends on the initial displacement of the particles. With increasing displacement the kick strength rises according to fig.(7.3) until the maximum is reached. For particles at displacements greater than

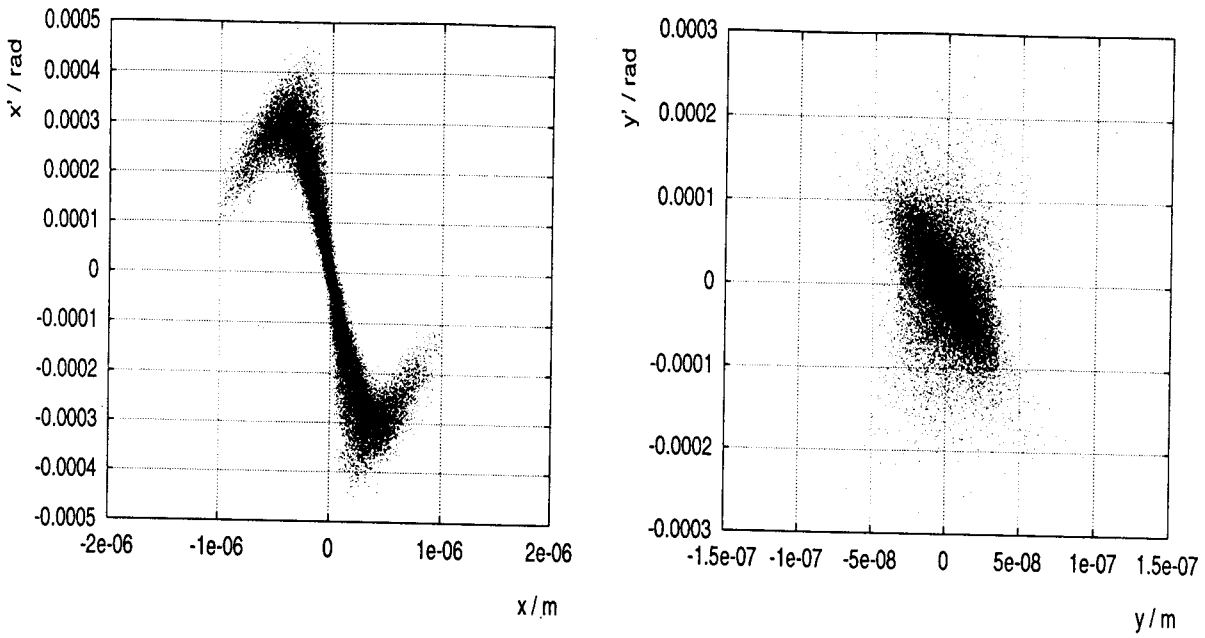

Figure 7.2: *The horizontal (left) and vertical (right) phase space distributions after the interaction for the SBLC, showing qualitatively the same behaviour as for TESLA (fig.7.1).*

about one sigma, the relative kick strength decreases and there is less deflection in the tails. This is the cause for the S-shape in the pictures on the left of fig.(7.1) and fig.(7.2).

In the vertical plane the deflecting component of the vertical force is a function of the integral of eq.(7.4) which is the monotonous error function. Therefore the vertical phase space distribution does not show the curved structure seen in the horizontal plane.

The beam properties after the interaction point are given in tab.(7.1). The emittances and optical functions are obtained from Lapostolle's definition [Lap71], as explained in appendix B.

7.2 Energy spread

During the interaction the particles emit synchrotron radiation, the so-called beamstrahlung in the strong electromagnetic field of the opposing beam. The typical photon energy reaches a range where the quasi-classical treatment of quantum emission explained in chapter (3) is no longer valid. Thus, the description of the emission process has to take into account quantum electrodynamical (QED) corrections. An important value to characterize the beamstrahlung is the parameter

$$\Upsilon = \frac{2}{3}\frac{\hbar\omega_c}{E} = \frac{\lambda_e\gamma^2}{\rho}, \tag{7.5}$$

which quantifies the ratio of the emitted photon energy to the particle energy E. The critical frequency ω_c is defined in chapter (3), λ_e is the electron Compton wave length and ρ the local bending radius of the particle trajectory. The parameter Υ is not constant during the interaction. For gaussian beams the average value of the beamstrahlung parameter can be estimated at [Yok91]

$$\Upsilon_{avg} = \frac{5}{6}\frac{Nr_e^2\gamma}{\alpha\sigma_z(\sigma_x+\sigma_y)} = \frac{5}{24\pi\varepsilon_0}\frac{e^2\hbar}{m_0^2c^3}\frac{N\gamma}{\sigma_z(\sigma_x+\sigma_y)}, \tag{7.6}$$

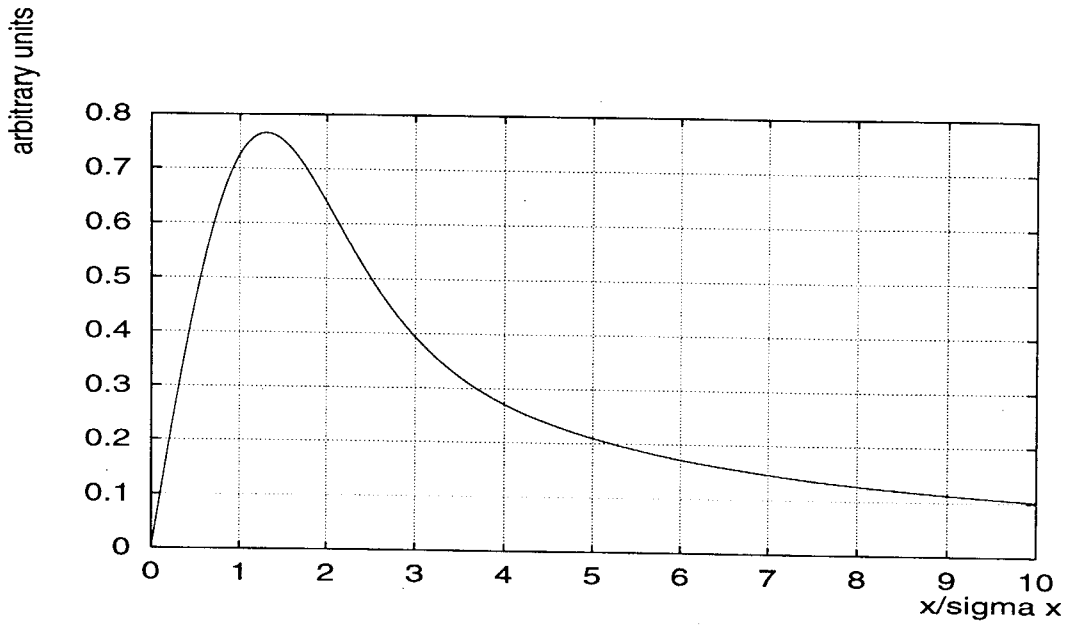

Figure 7.3: *The horizontal component of the attractive electromagnetic force as a function of the distance from the bunch center for flat beams following eq.(7.3).*

where N is the number of particles per bunch, r_e the classical electron radius and α the fine structure constant. For $\Upsilon \ll 1$ the emission follows the quasi-classical description. If $\Upsilon \geq 1$ a quantum electrodynamical formulation is necessary because the typical photon energy is comparable to the initial particle energy.

The emission process in this range has been calculated by Sokolov and Ternov [Sok68], taking into account the recoil of the particles. The photon number spectrum is given by

$$\frac{dn}{d\omega}(\omega) = \frac{\alpha}{\sqrt{3}\pi\gamma^2}\left[\int_x^\infty K_{5/3}(\tilde{x})d\tilde{x} + \frac{\omega\hbar}{E}\frac{\omega\hbar}{E-\omega\hbar}K_{2/3}(x)\right], \tag{7.7}$$

where $K_{5/3}$ and $K_{2/3}$ are the modified bessel functions of the order 5/3 and 2/3, respectively, and

$$x = \frac{\omega}{\omega_c}\frac{E}{E-\omega\hbar}. \tag{7.8}$$

A simulation of quantum emission according to eq.(7.7) is difficult. The photon emission rate cannot be expressed in a way as in the quasi-classical case (eq.(4.4)). A random generator providing the photon energy would be difficult to realize because the electron energy is an argument of the photon number spectrum, eq.(7.7).

For both SBLC and TESLA the values of Υ_{avg} are ≈ 0.05. The maximum value of Υ can reach twice this average value. In this case the quantum emission can be treated using the classical method as a first approximation with a correction depending on the energy of the incident electron.

The mean energy loss δ_E of the particles inside the bunch can be estimated according to [Yok91]:

$$\delta_E \approx 0.86\frac{r_e^3 N^2\gamma}{\sigma_z(\sigma_x+\sigma_y)^2}U_1(\Upsilon_{avg}). \tag{7.9}$$

$U_1(\Upsilon_{avg})$ is a function obtained from numerical calculations. The energy deviation after the interaction is not a gaussian distribution but is asymmetric with a low-energy tail containing

particles which loose up to 80% of their initial energy. The energy distributions after the interaction for TESLA and the SBLC are shown in figs.(7.4) and (7.5).

For the SBLC the center of the distribution is much broader than in the case for TESLA. The reason is the initial energy spread before the IP which is a factor of ≈ 6 higher for the SBLC due to the influence of wake fields on the beam during the acceleration. The SBLC energy distribution before the IP is not a gaussian distribution but shows a double peak. The energy deviation of the particles in the SBLC is linearly correlated with their longitudinal position in the bunches. This makes it possible to realize a head-on penetration of the bunches, although a crossing angle of 6 mrad is foreseen. The final focus optics provides a dispersion at the IP such that the bunches are tilted by half the crossing angle in the direction of the oncoming beam. This method, the so-called crab crossing, compensates for the luminosity loss which would occur in the case of an interaction with a non zero crossing angle. The Twiss parameters are undefined after the interaction. However, the emittances and the optical functions can be reasonably matched to the phase space distributions [Ros92],[Buo94]. As shown in tab.(7.1) the matched beta-functions (explained in appendix (B) after the interaction are very small and the beam divergence is large. This leads to a considerable growth of the beta-functions over a comparably small distance according to

$$\beta(s) = \beta_0 - 2\alpha_0 s + \frac{1+\alpha_0^2}{\beta_0} s^2 \approx \frac{1+\alpha_0^2}{\beta_0} s^2. \tag{7.10}$$

In the TESLA case the spent beam has to pass the final-focus doublet of the oncoming beam which is 3 m away from the IP. The beta-functions after the IP are very small (tab.(7.1)). This leads, together with eq.(7.10), to a horizontal beta-function of ≈ 85000 m inside the doublet. The first quadrupole is horizontally defocusing. As explained in more detail in section (8.2.1), the linear chromaticity created by a quadrupole is given by

$$\xi_C = \pm \frac{1}{4\pi} \int k(s)\beta(s)\, ds, \tag{7.11}$$

where the positive sign stands for the horizontal and the negative for the vertical chromaticity. Together with the strong final focus quadrupoles (with a focal length of ≈ 3 m) and taking into account an average β of ≈ 50000 m, we obtain a linear chromaticity in the order of $\xi_{C_x} \approx 8000$ which would cause a horizontal emittance growth by a factor of about a thousand due to the very broad energy distribution. In the vertical plane the resulting chromaticity is not as high but it still deteriorates the emittance by a factor of roughly 100 if not corrected.

The situation in the SBLC is different because, due to the crossing angle, the spent beam does not enter the final focus quadrupoles along the longitudinal axis. So the final focus quadrupoles for the oncoming beam have no focusing effect on the spent beam although their nonlinear magnetic field deteriorates the beam emittances. These effects will be explained in more detail in section (8.1.2).

		SBLC	TESLA
$\varepsilon_x/\varepsilon_y$	[10^{-5}mm mrad]	3.45 /0.088	11.3/0.12
β_x/β_y	[mm]	3.10 /0.34	6.06/0.66
α_x/α_y		1.88/0.49	1.94/0.93
σ_x/σ_y	[nm]	327.0/17.3	827.5/28.1
σ'_x/σ'_y	[mrad]	0.225/0.057	0.298/0.058
mean energy loss δ_E	[%]	2.76	2.44
energy spread σ_E	[%]	4.89	4.68

Table 7.1: *Beam properties after the IP for the SBLC and TESLA*

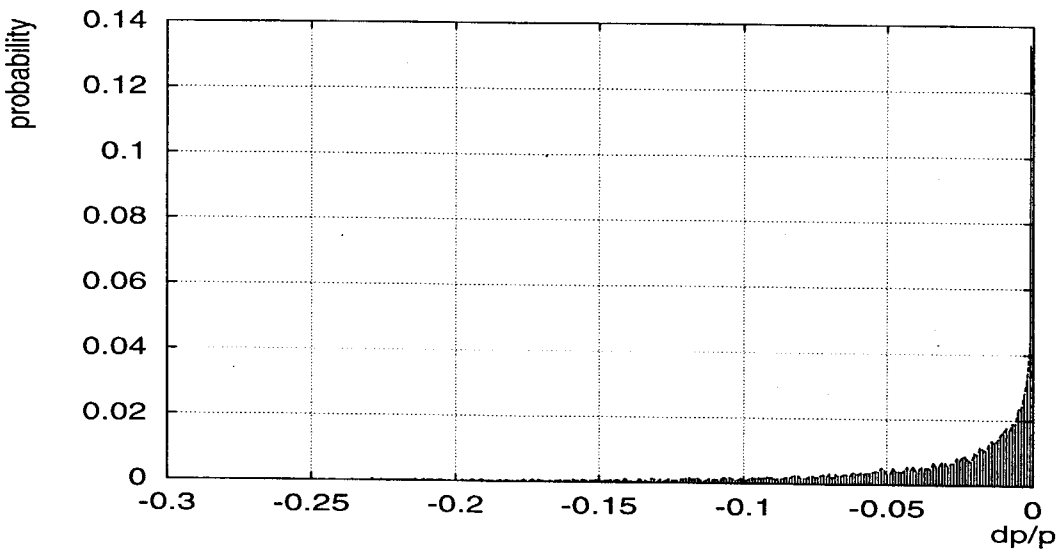

Figure 7.4: *Energy distribution of the disrupted beam for the TESLA linear collider.*

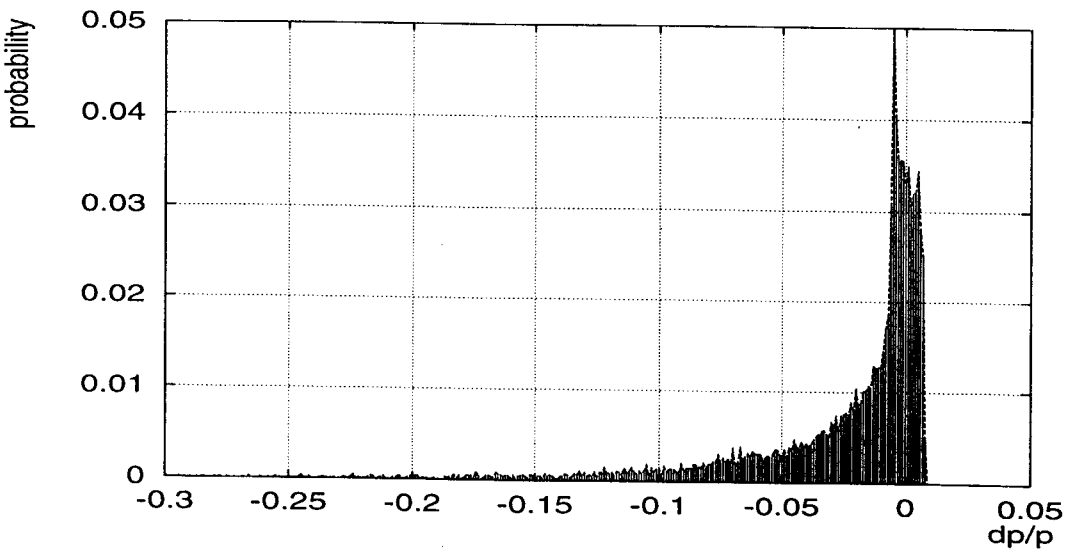

Figure 7.5: *Energy distribution of the disrupted beam for the SBLC. The broader distribution compared with fig.(7.4) is caused by the larger initial energy spread ($\Delta E/E \approx 0.35\%$) and the effects of wake potentials.*

Chapter 8

The unpolarized positron source operated with the spent beam

The realization of the positron sources after the interaction requires a careful handling of the spent beam in order to fulfill the emittance requirements explained in chapter (2). The spent beam has first to be separated from the oncoming beam to avoid parasitic interactions. This separation will be done in different ways for the two linear collider schemes.

In the TESLA case the long bunch spacing allows head-on collisions. Therefore, the spent beam has to be separated in the same beam line as the oncoming one. The deflecting device has to separate the spent beam without influencing the incident beam. A spent beam extraction system and a collimation system for the beamstrahlung have been developed by A.Drozhdin [Dro94] and are described in section (8.1.1). After the two beams have been separated from each other, the generated dispersion has to be matched to the following optics section. Since chromatic aberrations, caused by the strong focusing elements after the IP, deteriorate the beam properties unacceptably, the capture system has to be supplied with a chromaticity correction section. The general principle for chromaticity correction will be explained in section (8.2.1). The layout for the TESLA chromaticity correction system will be described in section (8.2.2). It is not possible to build a chromaticity correction section with an infinite energy bandwidth. Therefore one has to scrape off a considerable fraction of the spent beam. The beam collimators have to be positioned in such a way that the deposited beam power (of the order of 1.7−3.0 MW) is distributed over a long distance. A sketch of the spent beam capture system with regard to the oncoming positron beam is shown in fig.(8.1) for TESLA. The collimators, distributed along the whole capture system, are not shown in this figure.

For the SBLC, the structure of the capture system is almost the same as shown in fig.(8.1). A crossing angle of 6 mrad is foreseen at the interaction point to separate the spent beam from the oncoming positron beam. The main chromatic elements are not the final focus quadrupoles for the oncoming beam but a half-quadrupole doublet behind them. In the following part of the capture system, the optical functions are matched to the beginning of the chromaticity correction section which is a little bit more complicated than for TESLA. The problems related to the beam separation for the SBLC are explained in section (8.1.2). The chromaticity correction system for the SBLC will be described in section (8.2.3).

Behind the chromaticity correction section, the beam is lead through the wiggler to produce high energy photons. After the wiggler, the electron beam is deflected into a dump.

For a cost efficient way of integrating the capture system and the positron source into the collider layout, the collimation system, the wiggler with the target and the following positron

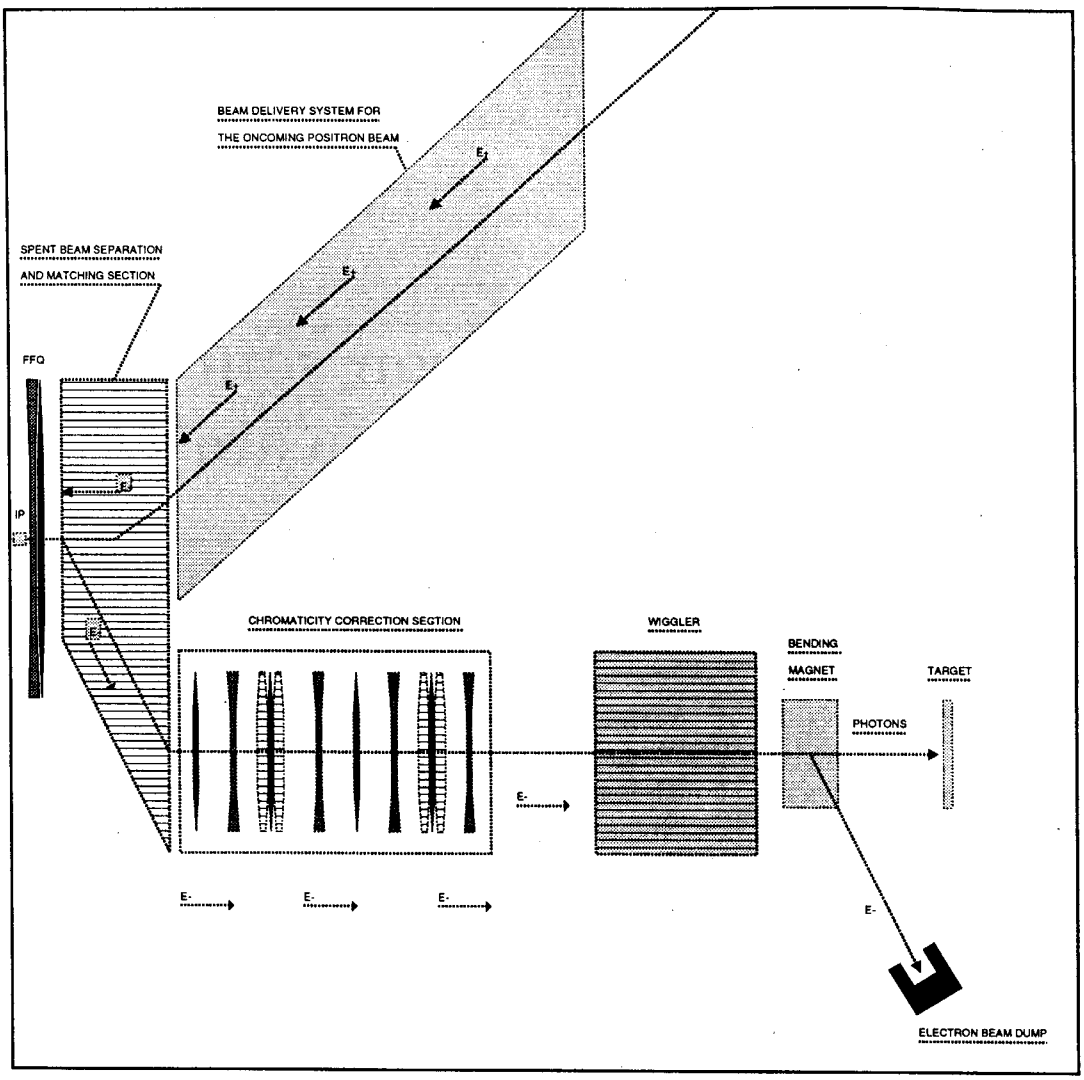

Figure 8.1:
Sketch of the spent beam capture system (lower branch) with regard to the oncoming positron beam (upper branch) for TESLA. The single components are described in the text. The collimators, distributed along the whole capture system, are not shown in this picture.

capture optics have to fit into the tunnel of the on-coming positron beam. The capture optics were designed using the beam optics program **COMFORT** [Woo83] taking into account the boundary conditions of the tunnel design and the peculiarities of the beam after the interaction. The optics program was extended in a way which enables one not only to study and to fit the beam optics functions but also the positions of the optical elements along the beam line in a 2-dimensional Cartesian coordinate system. An additional graphic routine was developed which uses the geometrical **COMFORT**-output to plot the positions relative positions of two beam lines. Furthermore, a **COMFORT**-based routine was created as an interface to the versatile commercial program system **GDS** (Graphic Data System [Mei95]), which allows a 3-dimensional simulation of the linac tunnel including the beam optics elements. This feature will become more important in the future for the development of the tunnel layout particularly near the detector region.

The design steps for the spent beam capture system are as follows: After estimating the

spent beam properties using the beam-beam simulation program the optical functions were matched to the beginning of the achromatic section, the structure of which is explained in section (8.2.1). The dipole strength inside the FODO cells of the achromatic section have been chosen taking into account the tunnel geometry and to provide an optimum result of the chromaticity correction. The particle ensemble was tracked through this tentative capture system using the tracking program **TRAFLUC** which was developed especially for this purpose. The tracking routine is steered by **COMFORT**-output files which can be obtained by calling **COMFORT** with a certain option. The tracking program allows for simulations including the quantum excitation effects. After estimating the emittance growth due to quantum fluctuations the optimization of the beam line can be started once again.

8.1 Beam separation after the IP and the dispersion matching section

8.1.1 TESLA

Due to the large bunch spacing of 708 ns the disrupted electron bunch meets the next oncoming positron bunch at a distance of 106 m from the interaction point (IP). This long distance permits a spent beam separation without a crossing angle. After passing through the final focus doublet of the oncoming beam the spent beam is focused by the final focus quadrupoles (which are strong focusing for the oncoming positron beam as well as for the disrupted beam) at a point 142.5 m from the IP. An electromagnetic separator is proposed to extract the spent beam along the first 27.5 m behind the IP. The separator consists of electrostatic and magnetic deflectors combined in the same unit to provide deflection of the outgoing beam without affecting the incoming beam [Nap93]. The separator consists of two parts of 10 m in length. The first one begins 7.5 m downstream of the IP.

Downstream the second separator at a distance of 32 m the separation between the two beams is sufficiently large to provide a further deflection by a set of septum magnets with different strength and apertures. At the entrance of the first septum magnet a 2 m long aluminum shield is placed to protect the septum from the beamstrahlung produced during the interaction and from spent beam particles in the halo of the beam. Tab.(8.1) shows the parameters of the spent beam extraction devices. The scheme of the extraction system created by A.Drozhdin [Dro94] is shown in fig.(8.2). A bending magnet is placed 54.1 m after the last

Device	Distance from IP [m]	Length [m]	Horizontal aperture [mm]	Vertical aperture [mm]	Magnetic field [T]	Electrostatic field [kV/cm]
Separator	7.5	10.0	50	80	0.016	48
Separator	17.5	10.0	50	80	0.010	30
Septum	59.5	4.0	60	30	0.08	-
Septum	63.5	4.0	60	30	0.12	-
Septum	67.5	8.0	80	30	0.12	-

Table 8.1: *Parameters for the TESLA spent beam extraction system developed by A.Drozhdin.*

septum magnet i.e. 129.6 m behind the IP in order to match the dispersion to zero together with a following quadrupole doublet and a further bending magnet inside the first FODO cell of the chromaticity correction section. These components are not shown in fig.(8.2).

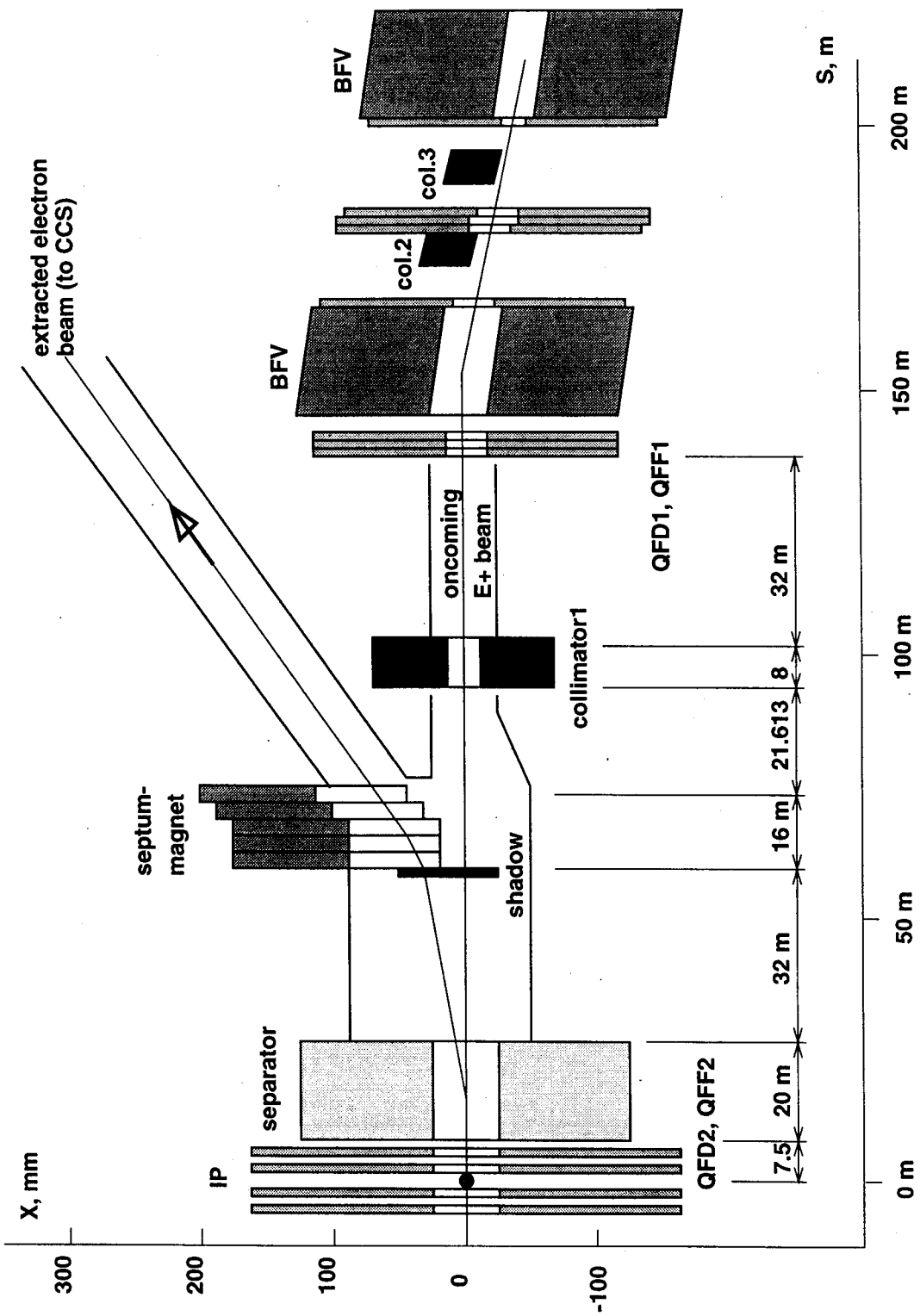

Figure 8.2:*Spent beam extraction system developed by A.Drozhdin.*

8.1.2 SBLC

With a bunch spacing of only 6 ns, parasitic interactions would occur already 0.9 m behind the IP. Hence, a beam separation without a crossing angle at collision is not possible. To optimize the crossing angle one has to take into account the luminosity reduction. To overcome the luminosity loss due to a crossing angle, the bunches can be rotated in the horizontal plane such that they penetrate the on-coming bunch head-on (i.e. the symmetry axes of both bunches are parallel). This method is called crab crossing and can be realized by introducing an energy distribution correlated with the longitudinal position of the particles in the bunch. If the energy deviation rises linearly with increasing distance from the bunch center, a rotation around only the vertical bunch axis can be provided with a non-vanishing dispersion at the interaction point. The crab crossing becomes more difficult with an increasing crossing angle. The separation between the two beams has to be great enough after 90 cm. It has to be ensured that the maximum disrupted particles even in the beam halo do not hit the oncoming bunch. Furthermore, the spent beam as well as the beamstrahlung has to pass through the final focus quadrupoles without damaging them. The crossing angle at the interaction point affects, that the spent beam enters the final focus quadrupoles for the oncoming positron beam displaced from the longitudinal axis (see fig.(8.4)). If the crossing angle is not great enough, the spent beam particles or photons of the beamstrahlung could destroy the pole tip region of the first final focus quadrupole. In the present state of the SBLC layout, a crossing angle of 6 mrad has been chosen to provide a sufficient beam separation and a feasible dispersive crab crossing.

In order to achieve the high gradient in the last final focus quadrupole before the interaction point (i.e. the first one after the interaction), there is no freedom making its aperture as large as possible. The quadrupole strength is k=0.357 m^{-2}, the magnetic field gradient $g \approx 300$ T/m. This leads to an aperture in the range of some mm. The first quadrupole after the interaction point has been designed by St.Wipf [Wip97] taking into account also the radiation emitted by the strongly focused particles upstream of the interaction point [1]. This radiation requires an aperture as large as possible beyond the pole tips. Shown in fig.(8.3) is 1/8 of the cross section of the first final focus quadrupole. Due to the crossing angle the spent beam enters the first final focus quadrupole approximately 13 mm displaced from the axis in a position beyond the pole tips (see fig.(8.4)). In this region, the field is not that of a simple focusing magnetic field gradient, but a superposition of higher order magnetic multipoles.

To estimate the effect of these fields on the spent beam, a field analysis was done with the program **OPERA-2d** from the company Vector Fields Ltd. The vertical magnetic field strength of the first final focus quadrupole as a function of the distance from the longitudinal quadrupole axis is shown in fig.(8.5). The beam receives an additional deflection due to the strong dipole component of the field which varies between roughly $1.0 - 1.6$ T. As shown later, this stronger beam separation, which seems to be advantageous at first glance, is related to an unacceptable emittance dilution due to quantum excitation.

For the second final focus quadrupole, the requirements are not that tight because the required strength is 28 % less than that for the first quadrupole. In addition, the offset of the spent beam is sufficiently large that it can pass safely through the spacious region between the pole tips and the copper conductor. The design of the second final focus quadrupole after the interaction point was developed by Ch. MacDowell [McD90] and has been scaled to provide the required aperture. The cross section of 1/8 of the second focusing final focus quadrupole is

[1] The non-disrupted beam before the IP is strongly focused by the final focus quadrupoles. The radiation emitted due to this strong quadrupole fields has a considerable energy which could also destroy the pole tip region of the downstream final focus quadrupoles.

shown in fig.(8.6). The vertical magnetic field as a function of the distance from the longitudinal quadrupole axis is shown in fig.(8.7).

The particles are tracked through the magnetic field to investigate whether the aperture is large enough even for particles in the low energy tail of the energy spectra and to investigate the influence of the off-axis fields on the beam.

A tracking routine was developed which simulates the transport of a beam through arbitrary magnetic fields. The **OPERA-2d** output was written into a field map with a mesh size of 0.1 mm. The magnetic field components have been calculated with a two dimensional linear interpolation between the data points. For a point $(\tilde{x}, \tilde{y})$ within the four grid points $(x_1, y_1) \cdots (x_2, y_2)$ with $x_1 \leq \tilde{x} \leq x_2$ and $y_1 \leq \tilde{y} \leq y_2$ the magnetic field is calculated according to

$$B_x(\tilde{x}, \tilde{y}) = a_{11} + a_{12}\tilde{x} + a_{13}\tilde{y} + a_{14}\tilde{x}\tilde{y} \tag{8.1}$$

and

$$B_y(\tilde{x}, \tilde{y}) = a_{21} + a_{22}\tilde{x} + a_{23}\tilde{y} + a_{24}\tilde{x}\tilde{y} \tag{8.2}$$

where the coefficients are obtained from

$$\begin{pmatrix} a_{11} & a_{21} \\ a_{12} & a_{22} \\ a_{13} & a_{23} \\ a_{14} & a_{24} \end{pmatrix} = \begin{pmatrix} 1 & x_1 & y_1 & x_1 y_1 \\ 1 & x_1 & y_2 & x_1 y_2 \\ 1 & x_2 & y_1 & x_2 y_1 \\ 1 & x_2 & y_2 & x_2 y_2 \end{pmatrix}^{-1} \cdot \begin{pmatrix} B_x(x_1, y_1) & B_y(x_1, y_1) \\ B_x(x_1, y_2) & B_y(x_1, y_2) \\ B_x(x_2, y_1) & B_y(x_2, y_1) \\ B_x(x_2, y_2) & B_y(x_2, y_2) \end{pmatrix} \tag{8.3}$$

The particles were tracked through the final focus quadrupole fields using the Runge-Kutta method. To estimate the statistical effect of quantum excitation the longitudinal step size Δs was chosen such that the average number of emitted quanta per step was much lower than one. The photon emission follows the poisson distribution and the probability that more than one photon is emitted per step is very low. The coordinates of the j^{th} particle in the $i + 1^{th}$ step are calculated according to

$$x_{i+1,j} = x'_{i,j} \cdot \Delta s + \frac{1}{2} \cdot \frac{e\,c}{E_{i,j}} \cdot B_y(x_{i,j}, y_{i,j}) \cdot \Delta s^2 \tag{8.4}$$

and

$$y_{i+1,j} = y'_{i,j} \cdot \Delta s - \frac{1}{2} \cdot \frac{e\,c}{E_{i,j}} \cdot B_x(x_{i,j}, y_{i,j}) \cdot \Delta s^2. \tag{8.5}$$

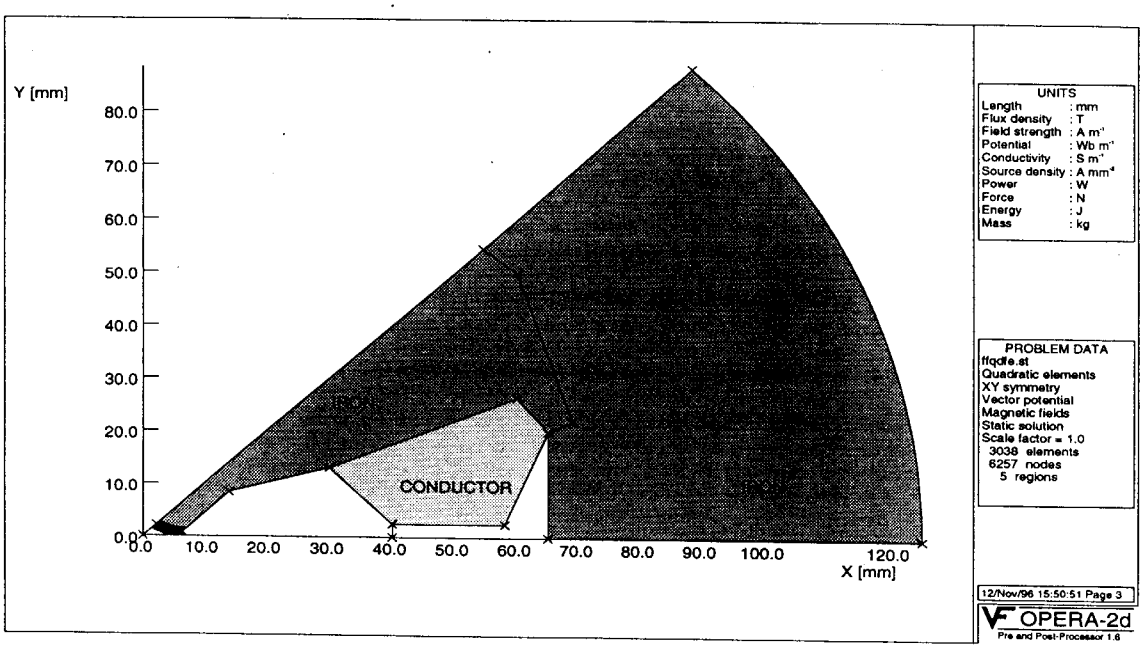

Figure 8.3: *Cross section of 1/8 of the first, horizontally defocusing final focus quadrupole.*

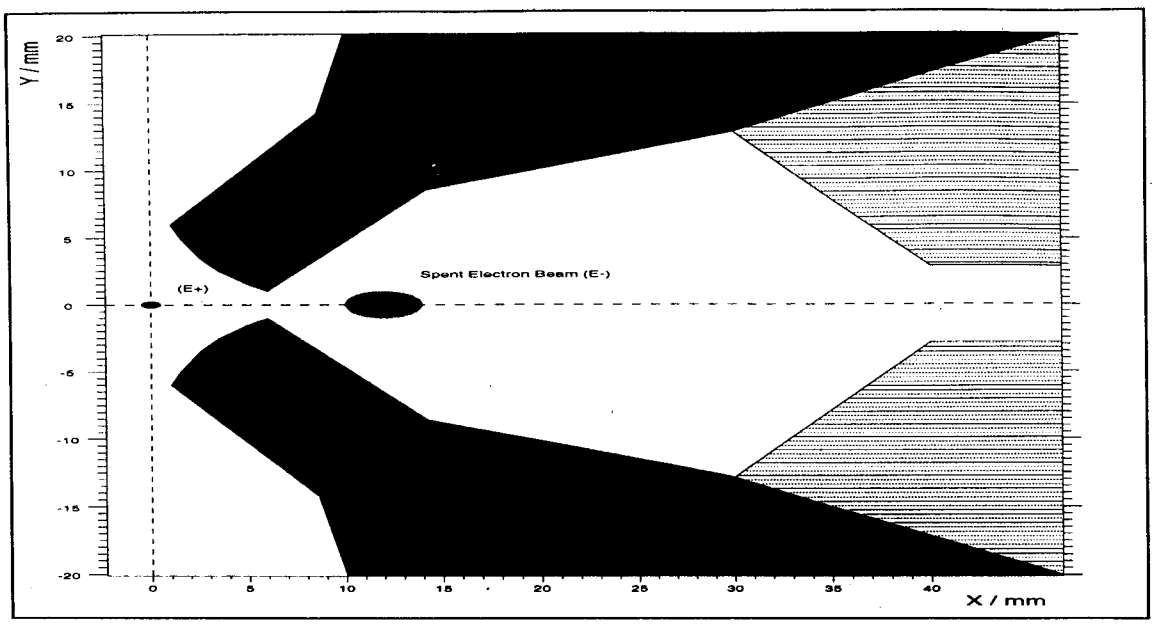

Figure 8.4:
Pole tip region of 1/2 of the first final focus quadrupole (seen from the IP). The hatched region shows the conductor, the solid region the iron. The oncoming positron beam is in the origin of the coordinate system. The ellipsoid 12 mm displaced from the origin shows the spent electron beam at the entry of the first final focus quadrupole. The vertical magnetic field component along the horizontal axis is shown in fig.(8.5). In this position, the magnetic field has higher order multipole components which increase the beam emittance.

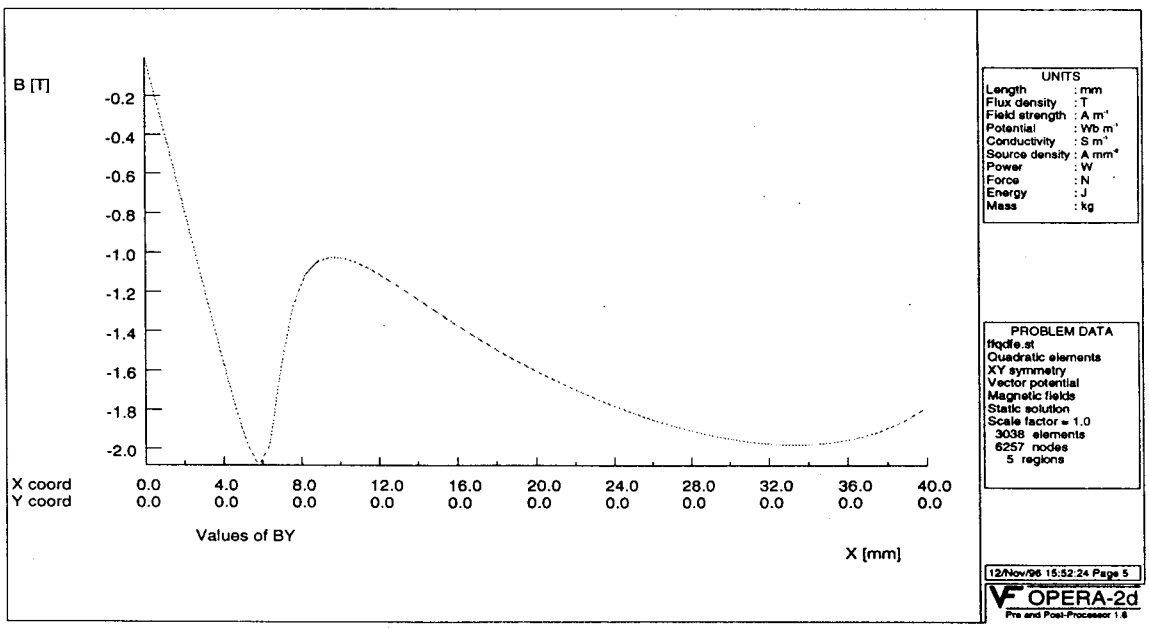

Figure 8.5:
Vertical magnetic field as a function of distance from the longitudinal symmetry axis. The spent beam enters the first final focus quadrupole with a horizontal offset of 12mm.

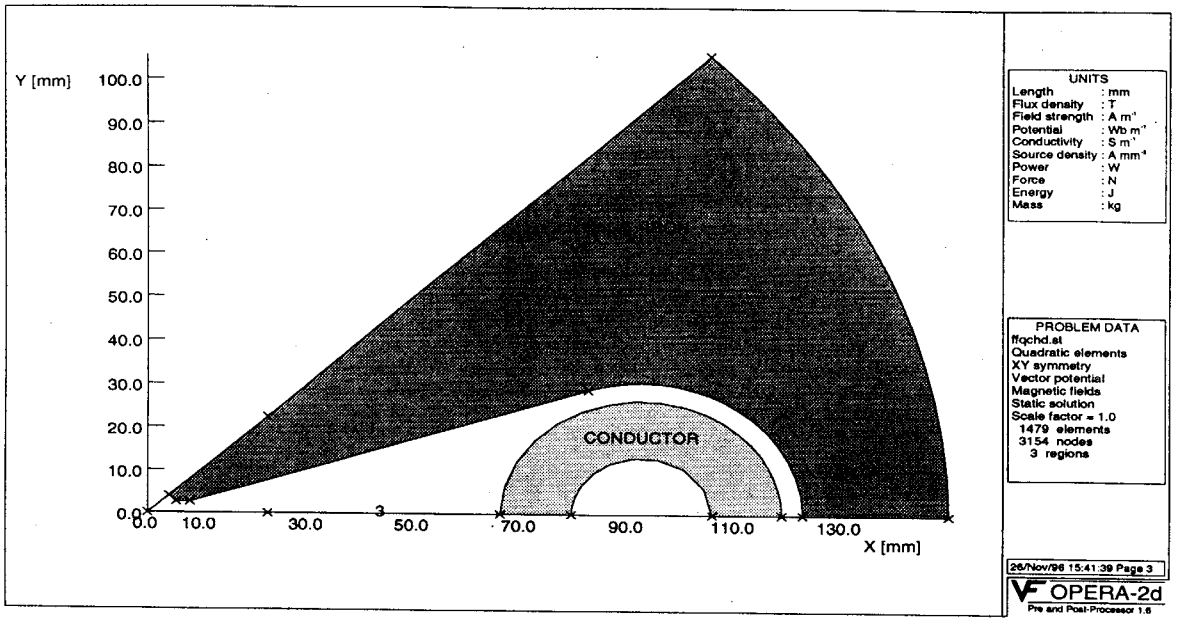

Figure 8.6: *Cross section of 1/8 of the second, horizontally focusing final focus quadrupole.*

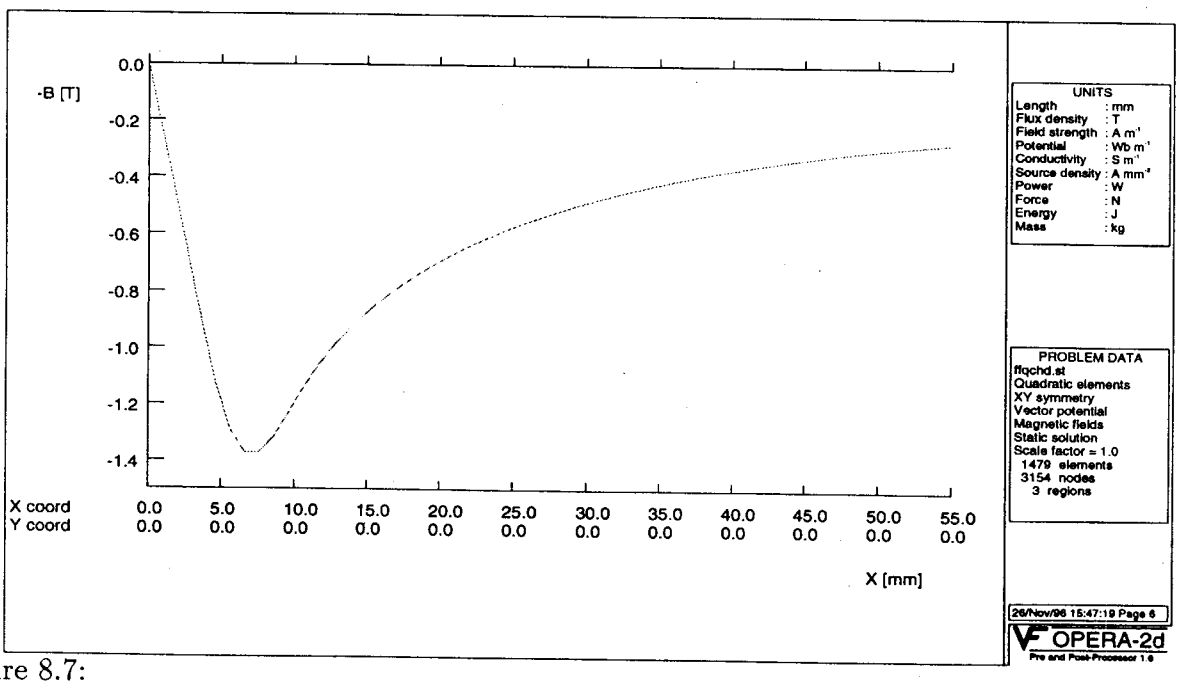

Figure 8.7:
Vertical magnetic field as a function of distance from the longitudinal symmetry axis. The spent beam enters the second final focus quadrupole with a horizontal offset of 30 mm.

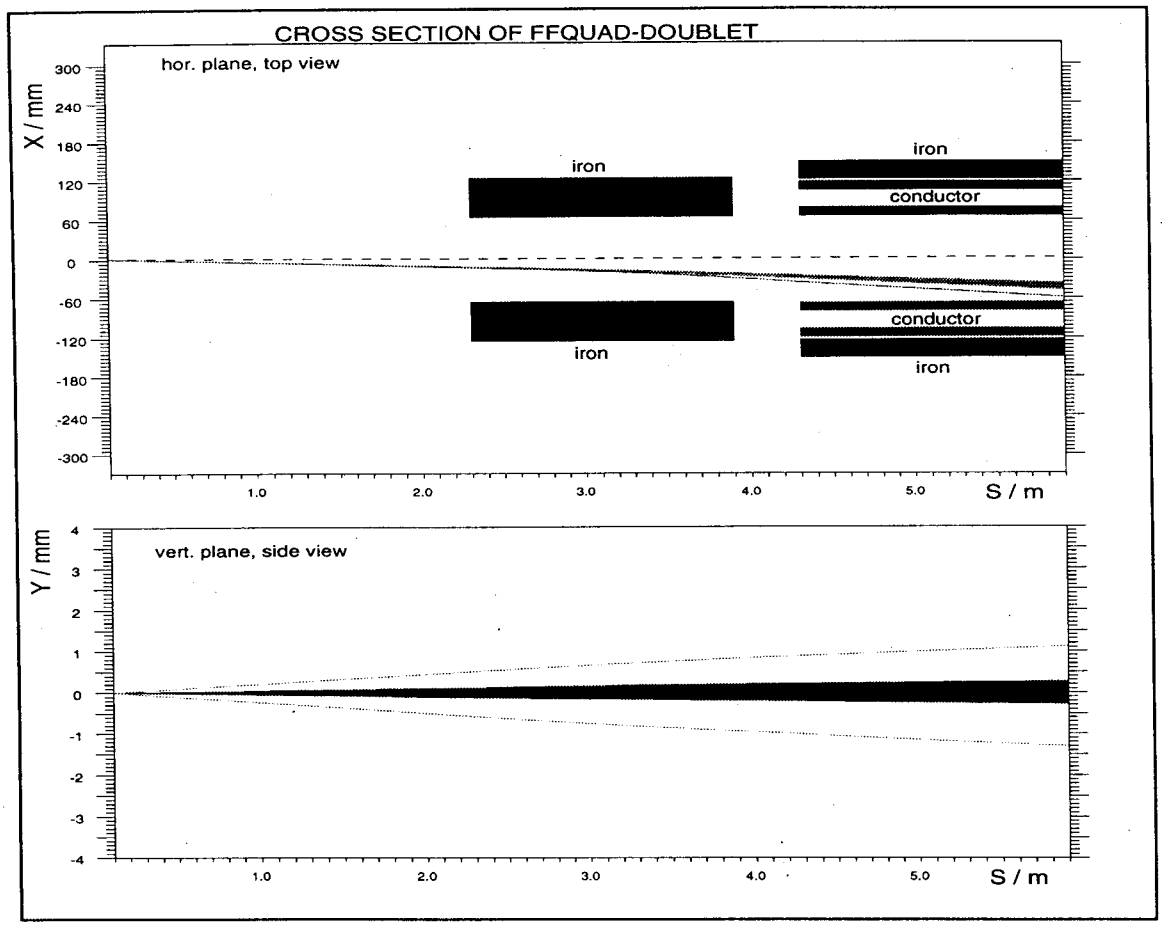

Figure 8.8:
Beam propagation through the final focus quadrupoles (FFQ's). Shown in the upper picture is the horizontal cross section of the FFQ's with the view point from above and the path of the spent beam through them. The single line represents a trajectory with an energy loss of 80 % of the initial energy. The lower picture shows the vertical beam height. The grey area represents the $\pm 1\sigma$ extension of the beam, the single lines show the vertical beam envelope (roughly $\pm 3\sigma$).

The upper picture in fig.(8.8) shows the path of the particles through the final focus quadrupoles in the horizontal symmetry plane. In addition to the data set from the beam-beam simulation program, a test particle with an energy deviation of 80 % was tracked to represent the low energy tail of the energy distribution shown in fig.(7.5). Even this particle, represented by the single trajectory in the upper picture of fig.(8.8), does not hit the second quadrupole. The filled area in the lower picture in fig.(8.8) indicates the vertical rms-beam size and single lines indicate the vertical beam envelope. The separation angle has increased to 8.53 mm due to the strong dipole component of the first final focus quadrupole. The distance between the spent beam and the given beam is roughly 4.2 cm. Further properties of the particle ensemble representing the whole beam (and subsets with a lower energy deviation) have been analyzed at the exit of the final focus quadrupoles and are collected in tab.(8.2). The emittances after passing the final focus quadrupoles are increased compared to the emittances directly after the interaction point. In the horizontal plane, the emittance is too high to fulfill the requirements for the polarized source, even if the undulator could be positioned directly behind the final focus quadrupoles. The origin of the emittance growth is analyzed in the

following part of this section. The idea is to compensate the emittance dilution in the beamline downstream of the final focus quadrupoles.

The properties of the spent beam after passing through the final focus quadrupoles are analyzed according to the energy distribution of the particles. First the whole beam is analyzed. The linear dispersion is calculated as explained in appendix (B) and subtracted from the horizontal phase space distribution. Then the emittances and optical functions are computed using Lapostolles method (appendix (B)). In the next step, only particles with a smaller energy deviation are considered. The optical functions and emittances for this ensemble are calculated as explained above. This is repeated with increasing energy cuts. After each step in the energy cut, the remaining particle ensemble is smaller, containing less particles than before. Shown in fig.(8.9) is the dependence of the remaining fraction of the spent beam from the energy cut.

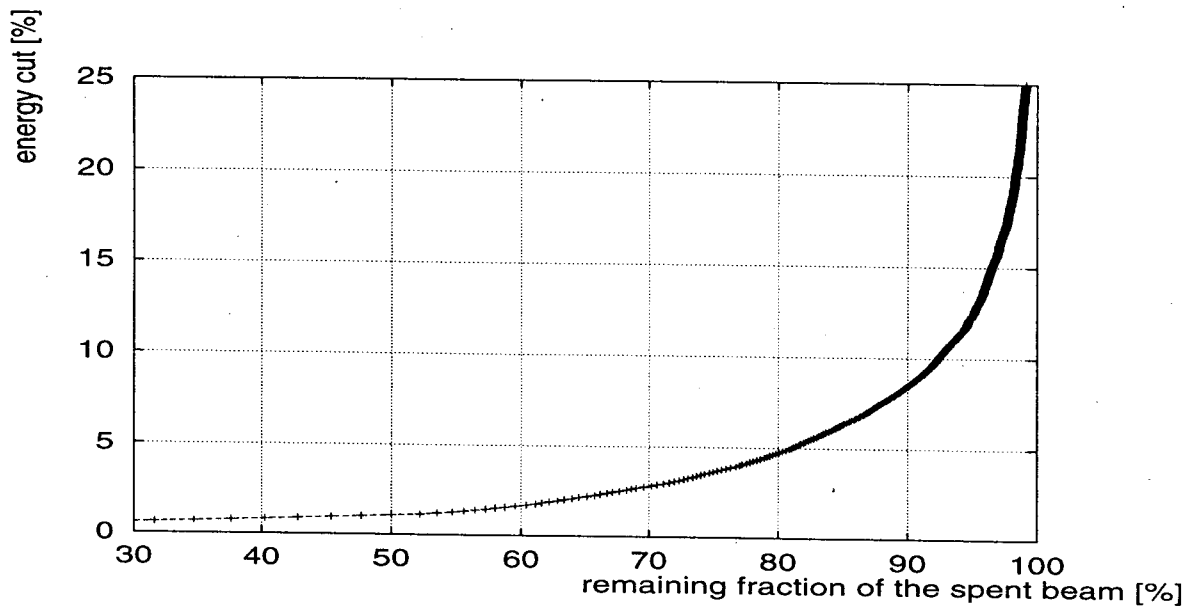

Figure 8.9: *Remaining fraction of the spent beam as a function of the energy cut for the SBLC. This figure is useful in combination with fig.(8.10) and fig.(8.11).*

The energy dependence of the horizontal and vertical emittances at the exit of the final focus quadrupoles are shown in figs. (8.10) and (8.11). The fraction of particles in these subsets are written on the abscissa of figs. (8.10) and (8.11). The corresponding energy cut on the spent beam is shown in fig.(8.9). This analysis was done to study the reasons for the emittance increase of the spent beam while passing through the final focus quadrupoles. The idea was to find a way to reverse the emittance growth in the downstream beamline if its origin is known.

As seen in fig.(8.10), the horizontal emittance requirements for the polarized positron source are not fulfilled for even 30 % of the beam. The origin of the emittance growth has been investigated by representing the influence of the nonlinear fields by sequences of optical elements. A particle set consisting of 90 particles was generated as explained later in chapter (8.2.1). These particles, representing the beam properties downstream of the IP, were tracked from the IP through the first final focus quadrupole using the Runge-Kutta method. The energy dependent optical functions have been calculated and stored. The test ensemble was tracked further through the 0.4 m drift space between the final focus quadrupoles and then through

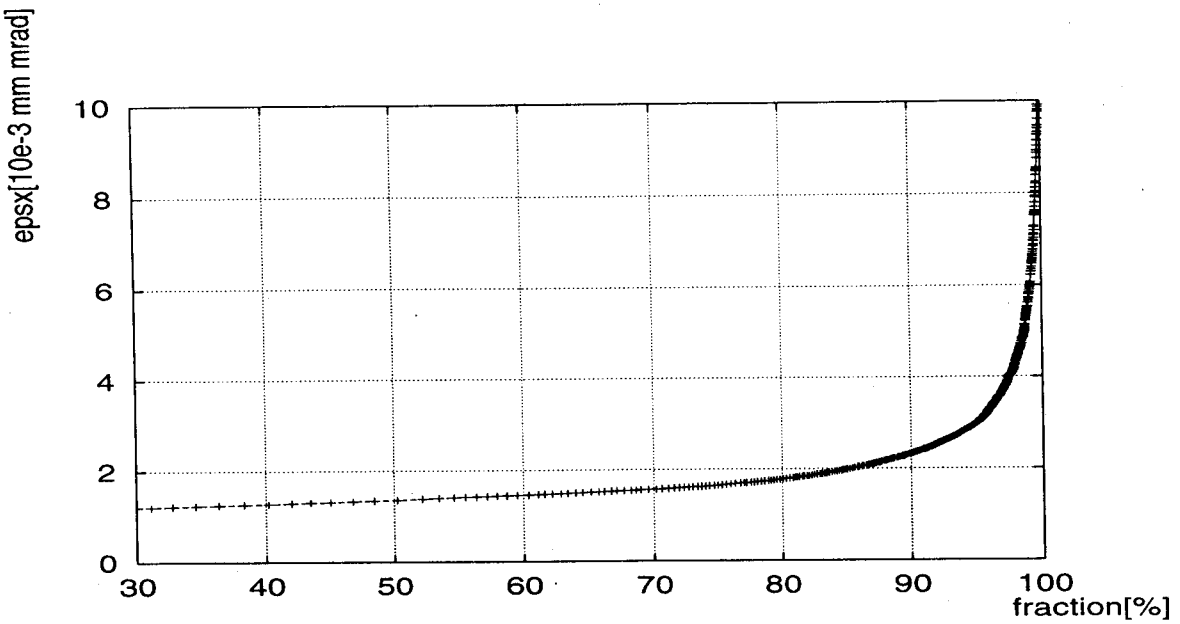

Figure 8.10: *Horizontal emittance as a function of the energy dependent fraction of the spent beam at the end of the final focus quadrupoles. The corresponding energy cut can be obtained from fig.(8.9).*

the second final focus quadrupole. The optical functions were once again calculated and stored again.

Each final focus quadrupole was replaced by four combined-function magnets of 0.3 m length alternating with sextupoles of 0.1 m (see tab.(8.3)). The combined-function magnets are to represent the dipole and quadrupole components of the inhomogeneous final focus quadrupoles. In the first step the test ensemble has been tracked through the 2.2 m drift space and the sequence of combined function magnets and sextupoles representing the first final focus quadrupole. The strengths of these elements have been assumed to be a linear function of their longitudinal positions. This was the simplest way simulate the variation of the multipole components along the

	Units	Full ensemble	$\lvert\Delta p/p\rvert < 0.08$	$\lvert\Delta p/p\rvert < 0.03$
β_x / β_y	[m]	295.61/278.76	990.43/381.68	1342.5/413.0
α_x / α_y		-62.12/-35.20	-207.51/-48.52	-280.8/-53.0
ε_x/ ε_y	[10^{-3}mm mrad]	7.795/0.274	2.241/0.194	1.58/0.16
η_x	[mm]	8.53	7.63	3.68
η'_x	[mrad]	2.64	2.33	1.49
$< x >$	[mm]	41.91	41.81	41.74
$< x' >$	[mrad]	8.09	8.06	8.04

Table 8.2: *Beam properties at the end of the final focus quadrupoles for the whole beam and for subsets of the beam consisting of particles which have lost not more than 8 % respectively 3 % of their initial energy.*

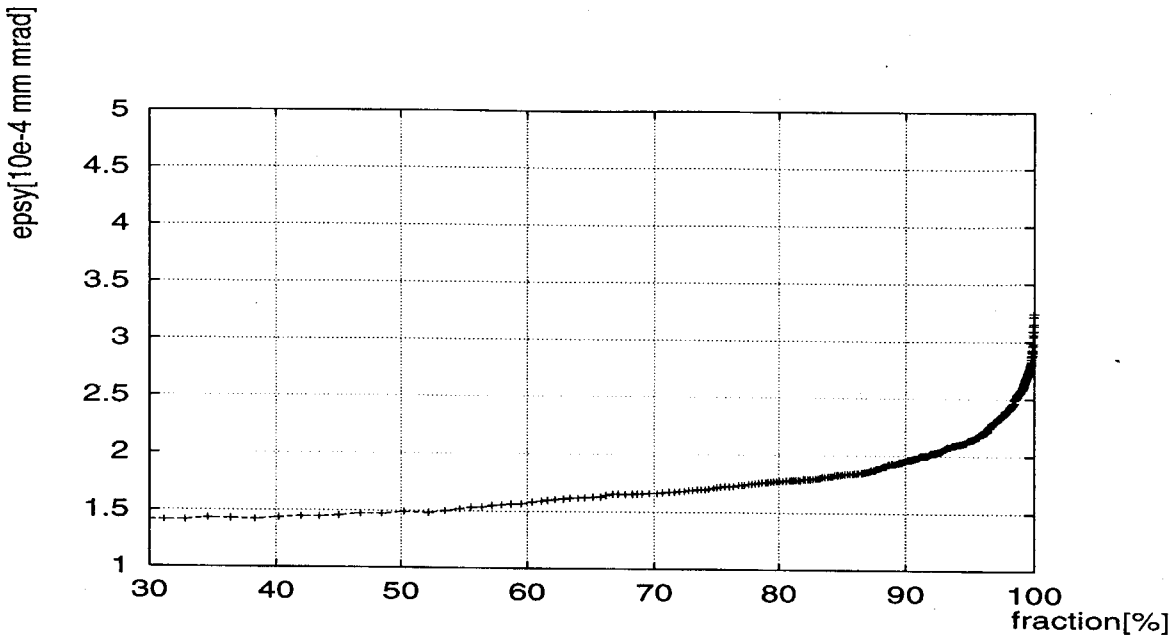

Figure 8.11: *Vertical emittance as a function of the energy dependent fraction of the beam at the end of the final focus quadrupoles. The corresponding energy cut can be obtained from fig.(8.9).*

spent beam path through the final focus quadrupoles by keeping the number of fitting parameters as small as possible. As the starting values for the parameter optimization, the strengths were estimated taking the field strength and their slopes in the beam path positions out of fig.(8.5). Thus, the first final focus quadrupole was described by the following six parameters: Four parameters for the linear functions for the deflection strength and quadrupole strength of the combined function magnets and two further parameters for the strength of the sextupoles following each combined function magnet.

The particles were tracked through the eight elements representing the first final focus quadrupole. At the end of each tracking process, the energy dependent beam properties were estimated and compared with the results of the Runge-Kutta tracking through the first final focus quadrupole. Then the tracking process through the elements started again with a different set of parameters. The variation of the parameters and the number of repetitions of the tracking process were steered using the Simplex-algorithm [Pre92]. The fitting process was stopped, when the difference between the Runge-Kutta results and the results from the tracking through the elements was minimized (relative deviation of less than a few tenth of a percent). In the second step, the parameters for the second final focus quadrupole were estimated in the same way.

Shown in tab.(8.3) are the strength of the elements replacing the final focus quadrupoles. The element strengths were obtained using the two times six parameters which have been found by the fit. With these optical elements it is possible to classify the sources of the emittance dilution, which can be divided into three groups:

- Due to the deflection of the beam the electrons emit synchrotron radiation leading to a horizontal emittance growth. Since the quantum emission is a statistical process, this emittance growth cannot be compensated in the downstream beamline. The vertical

	Element Type	Distance from IP [m]	Element length [m]	Deflection angle [mrad]	Quadrupole strength k [m^{-2}]	Sextupole strength m [m^{-3}]
	Drift	2.2	2.2	-	-	-
FFQ1	Comb. Function	2.5	0.3	-0.464	0.105	-
	Sextupole	2.6	0.1	-	-	-10.542
	Comb. Function	2.9	0.3	-0.612	0.091	-
	Sextupole	3.0	0.1	-	-	-10.996
	Comb. Function	3.3	0.3	-0.760	0.077	-
	Sextupole	3.4	0.1	-	-	-11.451
	Comb. Function	3.7	0.3	-0.908	0.064	-
	Sextupole	3.8	0.1	-	-	-11.906
	Drift	4.2	0.4	-	-	-
FFQ2	Comb. Function	4.5	0.3	0.201	0.025	-
	Sextupole	4.6	0.1	-	-	-3.161
	Comb. Function	4.9	0.3	0.185	0.020	-
	Sextupole	5.0	0.1	-	-	-2.584
	Comb. Function	5.3	0.3	0.169	0.015	-
	Sextupole	5.4	0.1	-	-	-2.001
	Comb. Function	5.7	0.3	0.153	0.009	-
	Sextupole	5.8	0.1	-	-	-1.433

Table 8.3: *Strength of the elements simulating the properties of the nonlinear field effects of the final focus quadrupoles.*

emittance is not affected because of the absence of vertical deflection.

- The horizontally defocusing and vertically focusing quadrupole components are the source of energy-dependent kicks. This chromatic error affects independently both the vertical and the horizontal emittances. The chromaticity can be corrected in the downstream achromatic section together with the geometric aberrations (see below).

- Geometric aberrations are produced by the sextupole components of the fields. Even if the particles had no energy deviation, the ensemble would suffer an emittance increase because of the kicks the particles obtain depending on the distance to the bunch center. These second-order effects provide coupling between the horizontal and vertical phase space.

The effects mentioned above are, of course, not completely independent. For example, with a strongly focusing quadrupole component, the beam diameter remains comparatively small along the path through the final focus quadrupoles. As a result, the geometric effects produced by the sextupole components are reduced because they grow with increasing beam diameter.

An additional complication in the analysis of the origin of the emittance growth is the nonlinear character of the dispersion and the chromaticity for large energy deviations. Even if the dipole components are only considered without the effects due to quantum excitation, the emittances after subtraction of the linear dispersion rise to $6.2 \cdot 10^{-4}$mm mrad for a sub-ensemble which has lost not more than 8 % of its initial energy. To further untangle the contributions of the different effects responsible for the emittance growth, a subset of the original ensemble was taken with energy deviations only between $\pm 0.1\%$. For this ensemble, the horizontal emittance

after the final focus quadrupoles (after subtraction of the linear dispersion, see appendix (B)) was still the same as that after tracking the particles through a drift space of the same length.

	ε_x [10^{-4}mm mrad]	ε_y [10^{-6}mm mrad]
Initial emittances after the IP	0.349	0.684
Only dipoles components	6.14	0.684
Only quadrupole components	0.561	24.23
Only sextupole components	9.851	182.4

Table 8.4: *Final emittances due to the different field components of the final focus quadrupoles (FFQ's). The results include the effect of quantum fluctuation.*

Tab.(8.4) shows the results of tracking these particles through only certain elements representing the final focus quadrupoles. To study for instance the effect of only the dipole component on the spent beam, all quadrupole strengths and sextupole strengths were set to zero (see tab.(8.3)). It can be seen in tab.(8.4) that the main contribution to the emittance growth in both the horizontal and the vertical planes is caused by the sextupole components of the final focus quadrupole fields. The effect of linear chromaticity is relatively small in the horizontal plane but increases the vertical emittance by a factor of roughly 40. The chromatic and geometric aberrations (i.e. the effect of the one directional kicks due to the sextupole components of the magnetic field) can be compensated later in the downstream beam line.

An important result is obtained by tracking the particles through only the dipole components of the field, including the effects of quantum excitation. The horizontal emittance is increased by a factor of approximately 17 compared to the initial emittance after the IP. Thus, the horizontal emittance requirement of $5 \cdot 10^{-10}$mm mrad for the polarized positron source is already exceeded. Because of its statistical character, the emittance growth caused by quantum excitation cannot be compensated. Hence it follows that in the case of the SBLC the polarized source using the spent electron beam cannot be realized with the present design of the final focus quadrupoles.

Concerning the unpolarized positron source the vertical emittance requirements are not critical. The demands on the horizontal emittance of $2 \cdot 10^{-2}$mm mrad can be fulfilled for roughly 85% of the particles under the assumption that no further emittance blow-up is created along the downstream beam line.

The matching section is continued with a doublet of half-quadrupoles each of length 3.5 m in a distance of 10 m after the last final focus quadrupole to focus the beam as soon as possible. The dispersion is matched to zero using a 3 m long bending magnet located 41 m after the doublet. A pair of quadrupoles is placed 26 m downstream to ensure the correct phase advance between the following achromatic elements and the main chromaticity producing elements.

8.2 The chromaticity correction section

8.2.1 Methods of chromaticity correction

Chromatic effects are caused by the energy dependence of the strength of beam optics elements. In bending magnets the particles are deflected by a constant magnetic field. The deflection angle of the particles is a function of the deviation of their energy. In a quadrupole the beam

is focused or defocused depending on the sign of the magnetic field gradient. If Δs is the quadrupole length, the focal length of this lens,

$$f = \frac{1}{k\,\Delta s}, \tag{8.6}$$

depends on the deviation of the energy of the particles from the design energy. The quadrupole strength k in eq.(8.6) is defined as

$$k = k\,(\Delta p/p_0) = \frac{e}{p} g = \frac{e}{p_0}\left(1 - \frac{\Delta p}{p_0} + \frac{1}{2}\frac{\Delta p^2}{p_0^2} - + \cdots\right) g. \tag{8.7}$$

Here g is the magnetic field gradient. Due to a quadrupole the particles obtain kicks whose strengths grow linearly with the distance from the bunch axis. The beam diameter remains almost constant if the focal length f is much greater than the quadrupole length Δs (thin lens approximation).

The focusing effect of a quadrupole on a particle beam can be considered as a turn of the phase space distribution. To illustrate the chromatic effect of a quadrupole on a beam containing particles with an energy deviation, a data set of 600 particles was created. The energy deviation of each of 200 particles was set to $\Delta p/p = 0.05, 0.0$ and -0.05, respectively. Shown in the left picture of fig.(8.12) is the initial phase space distribution. The beam is tracked through a strong horizontally focusing quadrupol and further to the focal point roughly 3.8 m behind it. The horizontal phase space distribution in this position is shown in the right picture of fig.(8.12). Only the subset containing particles with $\Delta p/p = 0.0$ is actually in a focal point. The particles are located on the x'-axis. The particle subsets with an energy deviation of $\Delta p/p = \pm 5$ % have a different shape in the phase space. The low energy subset has already passed through the focal point and diverges whereas the high energy subset is still 0.2 m before the focal point.

The emittances for each energy subset of the beam is still the same as at the beginning. The overall emittance of the complete beam, i.e. the phase space area of the whole ensemble has increased by a factor of roughly 100. As described in appendix B, the emittance can be estimated by the second order moments of the phase space distribution [Lap71].

$$\varepsilon_x = \sqrt{\overline{x^2}\,\overline{x'^2} - \overline{xx'}^2} \tag{8.8}$$

with

$$\overline{xx'} = \frac{1}{N}\sum_{i=1}^{N}(x_i - \overline{x})(x_i' - \overline{x'}), \quad \overline{x^2} = \frac{1}{N}\sum_{i=1}^{N}(x_i - \overline{x})^2, \quad \overline{x'^2} = \frac{1}{N}\sum_{i=1}^{N}(x_i' - \overline{x'})^2, \tag{8.9}$$

The emittance increase due to chromaticity can be expressed by the energy dependent change of the second order moments caused by the quadrupole. As calculated in [Buo94], the relative emittance growth can be expressed by

$$\frac{\Delta\varepsilon}{\varepsilon} = \frac{1}{2}\xi^2\overline{\delta^2}, \quad \xi = k_0 \Delta s \beta. \tag{8.10}$$

Here $\overline{\delta^2}$ denotes the variance of the energy deviation. The first focusing elements after the IP are very strong and the β-functions inside them are huge. This leads to huge chromatic effects and an intolerable increase of the emittances. This blow-up of the emittance has to

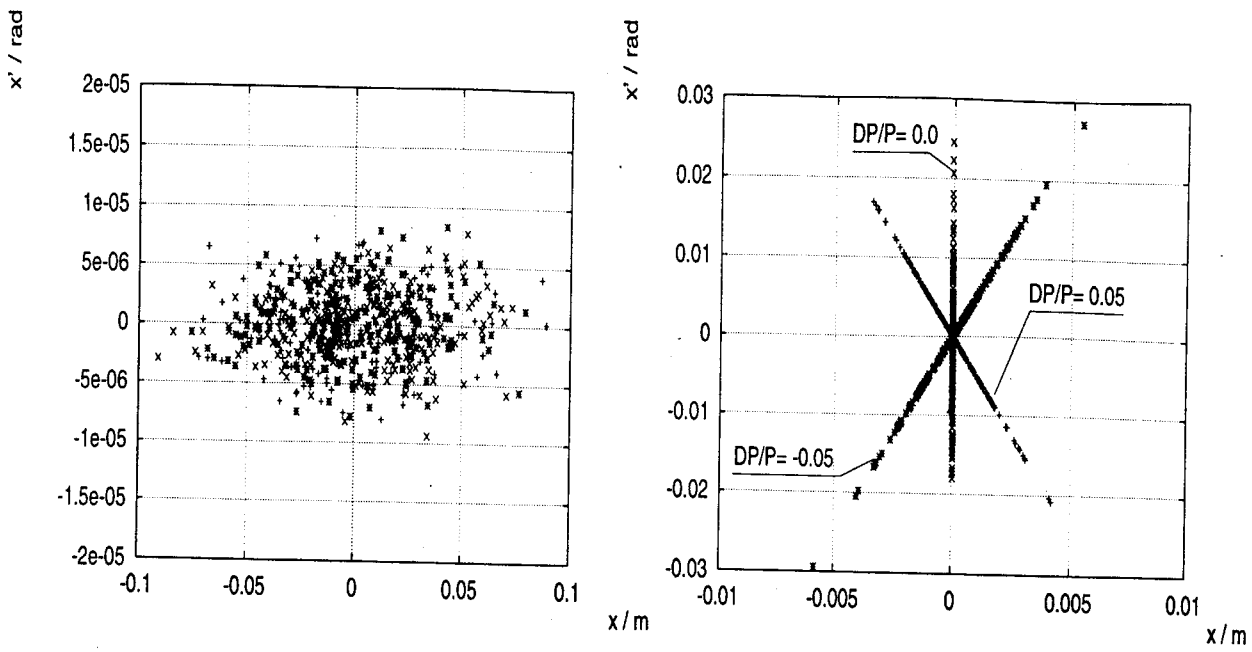

Figure 8.12:
Left: Horizontal phase space distribution containing 600 particles with an energy deviation of $\Delta p/p = 0.05, 0.0$ *and* -0.05 *(200 particles each) before the quadrupole.*
Right: Horizontal phase space distribution of the initial data set (left picture) after passing a strong horizontally focusing quadrupole and a drift space to the focal point. Only the particle subset with $\Delta p/p = 0.0$ *is actually in a focal point. The subsets with energy deviation have a different shape.*

be compensated, which can be done with sextupoles positioned in suitable positions in the downstream beam line. Since the chromaticity is a focusing error due to the particle energy deviation, the principle of chromaticity correction is to design dispersive regions where beam optics elements have an energy dependent focal length. A sextupole provides a linear increase of the local gradient from the horizontal displacement. Thus, the focusing strength increases with the distance from the axis. Off-energy particles have an energy dependent distance from the axis due to the horizontal dispersion following

$$\Delta x = \eta_x \frac{\Delta p}{p_0}. \tag{8.11}$$

Then the local focusing strength inside of a sextupole is

$$k_{sext} = m\eta_x \frac{\Delta p}{p_0}, \quad m = \frac{e}{p_0}\frac{\partial B_y^2}{\partial x^2}. \tag{8.12}$$

As shown by P.J.Bryant and K.Johnson [Bry94] the chromaticity produced along beam line can be expressed by

$$\xi_{C_x} = -\frac{1}{4\pi}\int [\left(\rho_0^{-2}(s) - k(s)\right)\beta_x(s) + m(s)\,\eta_x(s)\,\beta_x(s) + \cdots$$

$$\cdots + \rho_0^{-1}(s)\,(2\beta_x(s)\,\eta_x(s)\,k(s) + 2\alpha_x(s)\,\eta'(s) - \gamma_x(s)\,\eta_x(s))]ds \tag{8.13}$$

for the horizontal plane and by

$$\xi_{C_y} = -\frac{1}{4\pi}\int [k(s)\,\beta_y(s) - m(s)\,\eta_x(s)\,\beta_y(s)\cdots$$

$$\cdots - \rho_0^{-1}(s)\,\eta_x(s)\,(k(s)\,\beta_y(s) + \gamma_y(s))]ds \tag{8.14}$$

for the vertical chromaticity taking into account the main chromaticity creating elements. A complete evaluation for ξ_{C_x} and ξ_{C_y} including the edge focusing effect of rectangular bending magnets can also be found in [Bry94].

Geometric aberrations and sextupole positions

As explained in the previous section, sextupoles are required for chromaticity correction. The magnetic field pattern of these optical elements have also negative effects on a particle beam passing through it. The magnetic field components of a normal sextupole are [Ros92]

$$B_x(x,y) = g\,xy, \quad B_y(x,y) = \frac{1}{2}g(x^2 - y^2). \tag{8.15}$$

If flat beams are considered, i.e. $y \ll x$ for all particles, the dominating effect of a sextupole is caused by the vertical magnetic field component which grows quadratically with the horizontal distance to the symmetry axis. The particles passing through a sextupole will obtain uni-directional kicks, the strength of which has also a second order dependence on the sextupole center. After passing a sextupole the phase space distributions of particle beam have a curved shape. This effect is called geometric aberration and leads to an increase of the rms-emittance (eq.(8.8)). Geometric effects of sextupoles are not taken into account in eq.(8.13) and eq.(8.14). An effective way to get rid of chromatic effects without increasing the emittance by geometric aberrations is to split the chromaticity correcting elements in such a way that the phase advance between them is π. This was first proposed by K.L.Brown and R.V.Servranckx [Bro80]. Without changing the dispersion and the β-function at the position of the sextupoles, the chromaticity can be compensated by choosing the sextupole strength according to eq.(8.13) and eq.(8.14) (the sextupole strength will be determined in a more practical way described later). The advantage of this scheme is that the geometric aberrations generated in one sextupole are canceled in the next. The vertical chromaticity is corrected in the same scheme using sextupoles of opposite polarity.

The main chromatic elements in the spent beam capture systems described in the following sections are the first focusing elements behind the IP. For TESLA, this is the final focus doublet for the oncoming beam. In the SBLC, the inhomogeneous final focus quadrupole fields have only a negligible focusing effect on the spent beam. The chromaticity is created mainly by the half-quadrupole doublet located 10 m downstream the final focus quadrupoles. In both linear collider schemes it is not possible to compensate the chromaticity locally at the point of origin even if the geometric aberrations were not be important. One reason is the absence of space near these focusing elements. Furthermore in the TESLA case there is no dispersion near the final focus quadrupoles. In addition, the effects of a sextupole on the incoming beam would be intolerable.

The sketch of the chromaticity correction section for TESLA is shown in fig.(8.13). Located after the initial beam separation and matching section, the chromaticity correction section consists of a magnet lattice very similar to the achromatic final focus system for the incoming

beam developed by R.Brinkmann [Bri90]. The chromaticity correction sections for each plane are constructed using four FODO cells with a phase advanced of $\pi/2$ each. The sextupoles are positioned near the quadrupoles where the β-functions are huge. The matching section provides a phase advance of $\pi/2$ between the final focus quadrupoles (denoted as FFQ in fig.(8.13)) and the beginning of the chromaticity correction section. Thus, the conditions for correcting the chromaticity without generating geometric aberrations are fulfilled (i.e. a advance of an integer multiple of π between the main chromatic elements and the main sextupoles).

The horizontal periodic dispersion in the horizontal chromaticity correction system has its peaks in the same position as the horizontal β-function. The dispersion is created by a bending magnets of the same length and strength inside each FODO cell. Hence the horizontal chromaticity correction section is supplied with two pairs of bending magnets with a pairwise phase advance of π. The dispersion generated in the first bending magnet of a pair is cancelled in the second.

In the case of the SBLC, the chromaticity correction section consists not only of a horizontal but also a vertical chromaticity correction section, the structure of which is almost the same. The location of the maximum vertical β-function is inside the vertical focusing quadrupoles. In those elements the horizontal dispersion is increased. Thus, the horizontal dispersion maxima are located in different positions from the vertical β-peaks. For this reason the vertical chromaticity correction system, which is necessary for the SBLC spent beam capture system, contains stronger main sextupoles compared to the horizontal chromaticity correction section.

Optimization of the sextupole strength

With a complete layout of the capture system (taking into account the geometric boundary conditions), the optical functions are matched and the positions of the sextupoles of the chromaticity correction section are determined as described above. The strengths of the sextupoles were not computed in an algebraic way using eq.(8.13) and eq.(8.14), but have been obtained from a fitting program which optimizes the emittances at the end of the achromatic system. This optimization program, developed specifically to minimize the chromatic effects, is based on particle tracking through the capture optics. Starting with a set of particles, the properties of which are described later, the tracking was done by optimizing the sextupole strength using the SIMPLEX-Algorithm. The sextupole strengths have been considered as parameters of the function

$$F = G_x \varepsilon_x + G_y \varepsilon_y \tag{8.16}$$

which is computed after each complete tracking through the chromaticity correction section. G_x and G_y are weight factors to steer the fitting process and to adapt the optimization to the emittance requirements at the end of the chromaticity correction section with respect to the initial values of ε_x and ε_y.

Due to limitations in computation time the beam is represented by a few particles. The goal energy bandwidth of the chromaticity correction section, $|\Delta p/p| < 0.08$, was divided into 10 equidistant intervals. As a first attempt, each energy was represented by a set of 4 test trajectories weighted according to the asymmetric energy distributions shown in fig.(7.4) and fig.(7.5). The sets of 4 test trajectories were sufficient to provide the correct initial conditions of the optical functions α, β and γ and of the emittances ε in each plane for each energy bin. For each plane the 4 particles were positioned in a rectangle parallel to the axes with the coordinate points $(\sigma_{x,y}, \sigma_{x',y'})$,....,$(-\sigma_{x,y}, -\sigma_{x',y'})$ according to [Buo94]

$$\sigma_{x,y} = \sqrt{\frac{1}{2}\varepsilon_{x,y}\left(\beta_{x,y} + \gamma_{x,y} + \frac{2\alpha_{x,y}}{\sin 2\phi_{x,y}}\right)} \tag{8.17}$$

and

$$\sigma_{x',y'} = \sqrt{\frac{1}{2}\varepsilon_{x,y}\left(\beta_{x,y} + \gamma_{x,y} - \frac{2\alpha_{x,y}}{\sin 2\phi_{x,y}}\right)} \tag{8.18}$$

with

$$\phi_{x,y} = \frac{1}{2}\arctan\left(\frac{2\alpha_{x,y}}{\beta_{x,y} - \gamma_{x,y}}\right) \tag{8.19}$$

to provide the correct emittances. These rectangles were then turned under the angle of ϕ_x and ϕ_y, respectively, so that the initial values of α, β and γ were also fulfilled. These 40 particles were tracked by the fitting program while optimizing the sextupole strength to achieve the minimum rms-emittance.

The results of this program were checked with a simulation using the entire ensemble. It was found that the chromatic fit described above was not reliable in many cases, particular for the SBLC. Despite the low emittances obtained for the 40-particle ensemble at the end of the chromatic fit, the result for the whole beam was sometimes inconsistent. The reason for this is that the horizontal phase space distributions shown in fig.(7.1) and fig.(7.2) are too complicated to be sufficiently described by only four particles per energy interval. As explained above, the fit chooses the sextupole strength in such a way that particle trajectories starting from the same initial phase space positions pass through the chromaticity correction section such that their phase space positions at the end are identical, regardless of their energy deviation. The phase space distribution of the whole beam showed, that particles with the same initial conditions as those of the 40-particle ensemble actually did not have energy dependent phase space positions. However, the particles in the curved tail of the S-formed horizontal phase space distribution showed an energy dependent spread. Thus, the method of minimizing the chromaticity as described above was not incorrect but not applicable with respect to the beam properties after the IP. Nevertheless, the optimization process was always started as explained above. The results of the fit were used as the values for a more sophisticated fitting method. The advantage is a lower computation time.

To overcome this problem, the phase space coordinates of the test trajectories have been chosen following the geometrical form of the phase space distributions after the IP, as shown in fig.(7.1) and fig.(7.2). This is particularly important in the case of the horizontal phase space. The beam after the IP has been analyzed by a program in which the initial test trajectories are aligned as shown in fig.(8.14), in the extreme positions of the phase space distributions. These phase space distributions are not able to describe the initial conditions after the IP sufficiently well. For this reason each test trajectory was supplied with two additional weight factors representing the horizontal and vertical phase space densities of the complete ensemble in the environment of the test particles. The rms-emittance has been calculated using the weighted statistical moments according to

$$\varepsilon_z = \sqrt{\frac{\left(\sum_{i=1}^{n} g_{z_i} g_{\Delta p_i} \cdot z_i^2\right) \cdot \left(\sum_{i=1}^{n} g_{z_i} g_{\Delta p_i} \cdot z_i'^2\right) - \left(\sum_{i=1}^{n} g_{z_i} g_{\Delta p_i} \cdot z_i z_i'\right)^2}{\left(\sum_{i=1}^{n} g_{z_i} g_{\Delta p_i}\right)^2}} \tag{8.20}$$

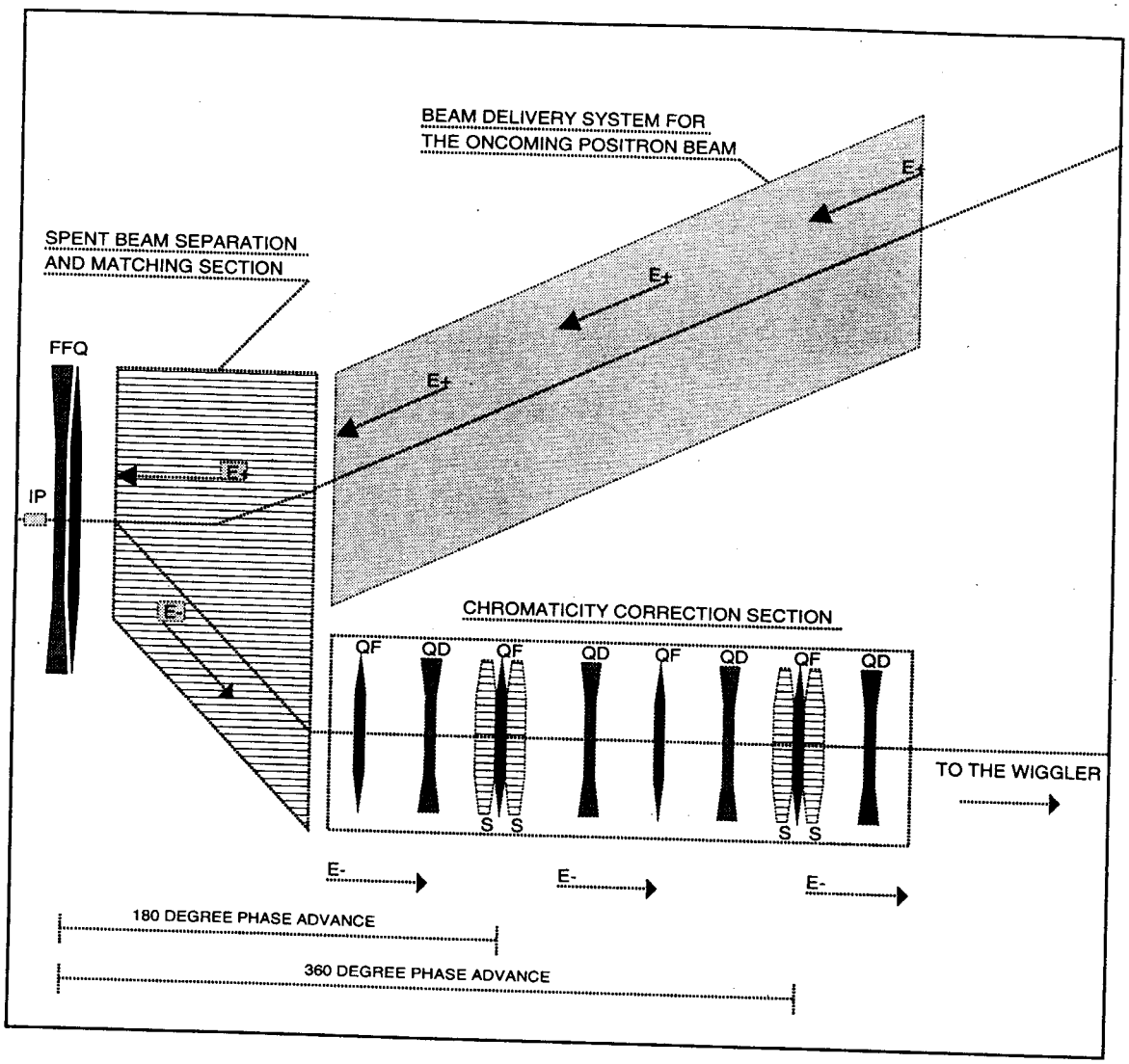

Figure 8.13:
Sketch of the chromaticity correction section for the spent electron beam for TESLA. The system, consisting of four FODO cells with 90 degree phase advance each, corrects only the horizontal chromaticity. The bending magnets, required to produce the periodic dispersion and the sextupoles for the local chromaticity correction, are not shown. The sextupoles in the chromaticity correction section are signed with S, *the focusing quadrupoles with* QF *and defocusing quadrupoles with* QD.

where z is used to denote both the vertical and horizontal coordinates, g_{z_i} are the phase space density weights and $g_{\Delta p_i}$ are the energy weight factors. The optimization process was started by tracking the test data set through the capture system minimizing the emittances at the end, according to eq.(8.20).

The best results have been achieved by using the 40 particle data set for a first optimization. After the optimum sextupole strengths have been estimated, the fit was started again taking the output from the first run as the input for the second, using the 90 particle data set.

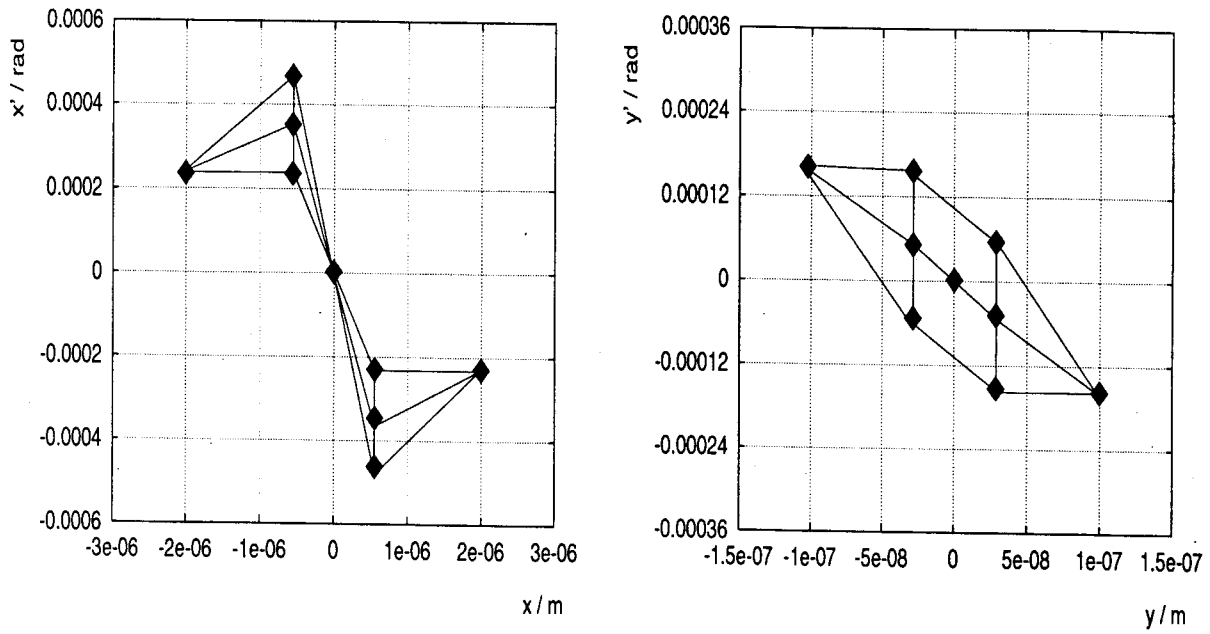

Figure 8.14: *Horizontal (left) and vertical (right) phase space distributions of the chromatic fit ensemble after the interaction for TESLA. The 9 particles of each of the 10 energies representing the asymmetric energy distribution shown in fig.(7.4) follow the phase space distributions in fig.(7.1).*

8.2.2 The chromaticity correction section and the beam transport through the wiggler for TESLA

The spent beam capture system for TESLA consists of the 142.5 m long separation and matching section described in section (8.1.1), the chromaticity correction section and the transfer line from the end of the achromatic section to the beginning of the wiggler. After the IP, the emittances are $1.13 \cdot 10^{-4}$ mm mrad horizontally and $1.2 \cdot 10^{-6}$ mm mrad vertically. Even for the polarized positron source, the vertical emittance is a factor of roughly 400 less than required whereas the horizontal emittance is only a factor 4.5 smaller than the required $5 \cdot 10^{-4}$mm mrad.

Therefore the achromatic section was based on only a horizontal chromaticity correction system in order to shorten the capture system. The consequence is a growth of the vertical rms emittance along the spent beam capture system. The main chromatic elements, responsible for the emittance increase of the spent electron beam, are the final focus quadrupoles for the oncoming positron beam. The need to separate the spent beam from the oncoming beam

creates dispersion. The optics functions from the IP to the end of the chromaticity correction section are shown in fig.(8.15). The quadrupole doublet between the last septum magnet and the chromaticity correction section provides the correct phase advance of $\pi/2$ between the final focus quadrupoles and the beginning of the achromatic section. The dispersion created in this region cannot be compensated until the beginning of the chromaticity correction section without deflecting the beam back into the direction of the oncoming beam.

The following achromatic section consists of four FODO cells of 90 m in length and with a phase advance of $\pi/2$ per cell. The second bending magnet BH3, located inside the first FODO cell, compensates the dispersion together with the last dipole BCOM inside the matching section. The main bending magnets (called BH, see fig.(8.15)) inside the FODO cell then have the same deflection strength of 1.57 mrad and length of 41.625 m. Thus, the magnetic field is very weak ($B = 0.03$ T) and the emittance growth due to quantum excitation is negligible. The phase advance of π between the first and third main dipole ensures that the dispersion created in the first dipole is canceled in the third although the magnetic field has the same sign. The second dispersion bump was created using the second and fourth dipole. The superposition of these bumps provides a periodic dispersion which vanishes at the end of the chromaticity correction section. At the end of the chromaticity correction section the spent beam has a reasonable distance of approximately 1.3 m from the final focus system [Nap94] of the oncoming beam. The beam line for the spent beam (together with the continuation of the optics and the wiggler) and for the given beam are shown in fig.(8.16).

The main sextupoles, used to compensate the chromaticity generated in the final focus quadrupoles, are located in the maximum positions of the the horizontal beta function. In addition, the chromaticity correction section is supplied with sextupoles compensating the local chromaticity of the focusing elements inside the FODO cells. The chromaticity of this complete beam line was minimized as described in the previous sections. The whole particle ensemble from the beam-beam simulation program was tracked through the beam line including the simulation of quantum emission. The data set was analyzed at the end of the chromaticity correction section by considering energy dependent subsets of the whole ensemble.

This analysis started with the energy interval $\bar{E} \pm \Delta E_{max}$ where $\bar{E}$ denotes the average energy and ΔE_{max} the maximum energy deviation of the particles. The first step was to estimate the properties of the complete data set. After computing the emittances and optical functions, the limit of the energy cut was decreased and the process was started again. The horizontal and vertical emittances are shown in fig.(8.18) and fig.(8.19) as a function of the percentage of the particle ensemble related to energy cut.

The emittance decreases tremendously as the fraction is decreased from 100 % to 70 % (the 70 % corresponds to an energy cut of 3.5 %). Then the emittance remains nearly constant for smaller beam fractions. The emittance does not show an energy dependence in this region but is determined by the emittance growth due to quantum excitation and remaining geometrical aberrations which cannot be compensated. For a subset containing ≈ 60 % of the spent beam, the horizontal emittance ε_x is $4.53 \cdot 10^{-4}$ mm mrad. The vertical emittance of $9.83 \cdot 10^{-5}$ mm mrad is negligible. Hence the emittance requirements for the polarized positron source using a helical undulator are fulfilled. This option will be discussed in more detail in chapter 10.

The nearly constant emittance for spent beam fractions of less than roughly 60 % seems to be strange at first sight. One might expect that the emittance would decrease more strongly by decreasing the fraction of the beam. This is correct if the cuts had been done by reducing the phase space area. In this case, the emittances would decrease more strongly with the beam fraction. From this point of view very tight emittance requirements could be fulfilled by keeping

a comparably large fraction of the beam. However, this is impractical because the unwanted fraction of the beam has to be collimated preferably along the drift spaces between the IP and the end of the capture system. As seen in fig.(8.15) and fig.(8.16), there is only limited space available between these elements. Furthermore, the chromaticity here is not corrected and the dispersion is non zero along the whole chromaticity correction section. Thus, the portion of the beam (signed by a phase space cut and not by an energy cut) to be scraped off is always hidden by the energy dependent shifts (due to dispersion) and twists (due to chromaticity) of the phase space distributions. These effects dominate the beam size along the chromaticity correction section.

The most effective way to get the maximum amount of the spent beam for positron production is to determine the energy dependent fraction of the beam that fulfills the requirements for the positron source at the end of the chromaticity correction section. As seen in fig.(8.19), the vertical emittance is not a problem. From fig.(8.18) one sees that the horizontal emittance requirements can be fulfilled for roughly 87 % of the spent beam, which corresponds to an energy cut $\Delta E/E$ of ≈ 7 %. With this information the tracking was repeated. It is relatively easy to tag the particles based on their energy deviation. The phase space distributions at the end of the drift spaces are plotted from fig.(8.20) to fig.(8.25).

The ensemble is divided using two symbols: One indicates the particles which are to be used for positron production and the other, particles which are to be collimated. Figure (8.26) and fig.(8.27) show the development of the horizontal and vertical emittances along the spent beam capture system (with the continuation of the chromaticity correction section through the wiggler) for particles with $|\Delta E/E| < 0.07$ without collimation.

Starting from the IP, the positions and the apertures of the the collimators were carefully positioned along the capture system. The goal was to distribute the collimated beam power as uniformly as possible. An additional point was to keep the beam envelope in reasonable limits. After the collimator positions were fixed such that only the particles with an energy loss of $|\Delta E/E| < 0.07$ could pass through the capture system, the optics functions and emittances to focus the beam through the wiggler were needed. The capture optics were continued with a drift space of 20 m and two quadrupole doublets with a distance of 18.7 m between them. The beam is focused such that the radiation emitted by a 35 m long wiggler hits the target in at focal point 20 m behind the wiggler, i.e. 60 m behind the last quadrupole doublet. Thus, the electron beam can be separated from the wiggler-radiation over a distance of 20 m between the end of the wiggler and the target. A magnetic field of 1.15 T is required to achieve a separation of 0.3 m between the electron beam and the radiation (due to the energy loss during the interaction and inside the wiggler, the particles have only an energy of 235 GeV). The horizontal radiation spot size on the target is roughly 0.9 mm which is greater than the required spot size of 0.7 mm. The effect of a lower capture efficiency is compensated by the vertical radiation spot size of 0.5 mm (see fig.(6.2)). The beam line between the end of the chromaticity correction section and the beginning of the wiggler is supplied with two additional collimators in order to optimize the system and to avoid that particles hit the wiggler. The efficiency of the capture system was found to be 84.3 %. The collimator positions and the beam power to be collimated along the capture system are collected in tab.(8.5). The horizontal and vertical beam envelopes which contain 84.3 % of the spent beam used for the positron production are shown in fig.(8.28) and fig.(8.29).

It can be concluded that the efficiency of the capture system under design conditions is high enough to operate the unpolarized positron source using the spent beam. The problems introduced by a disturbance at the IP will be discussed in chapter (9).

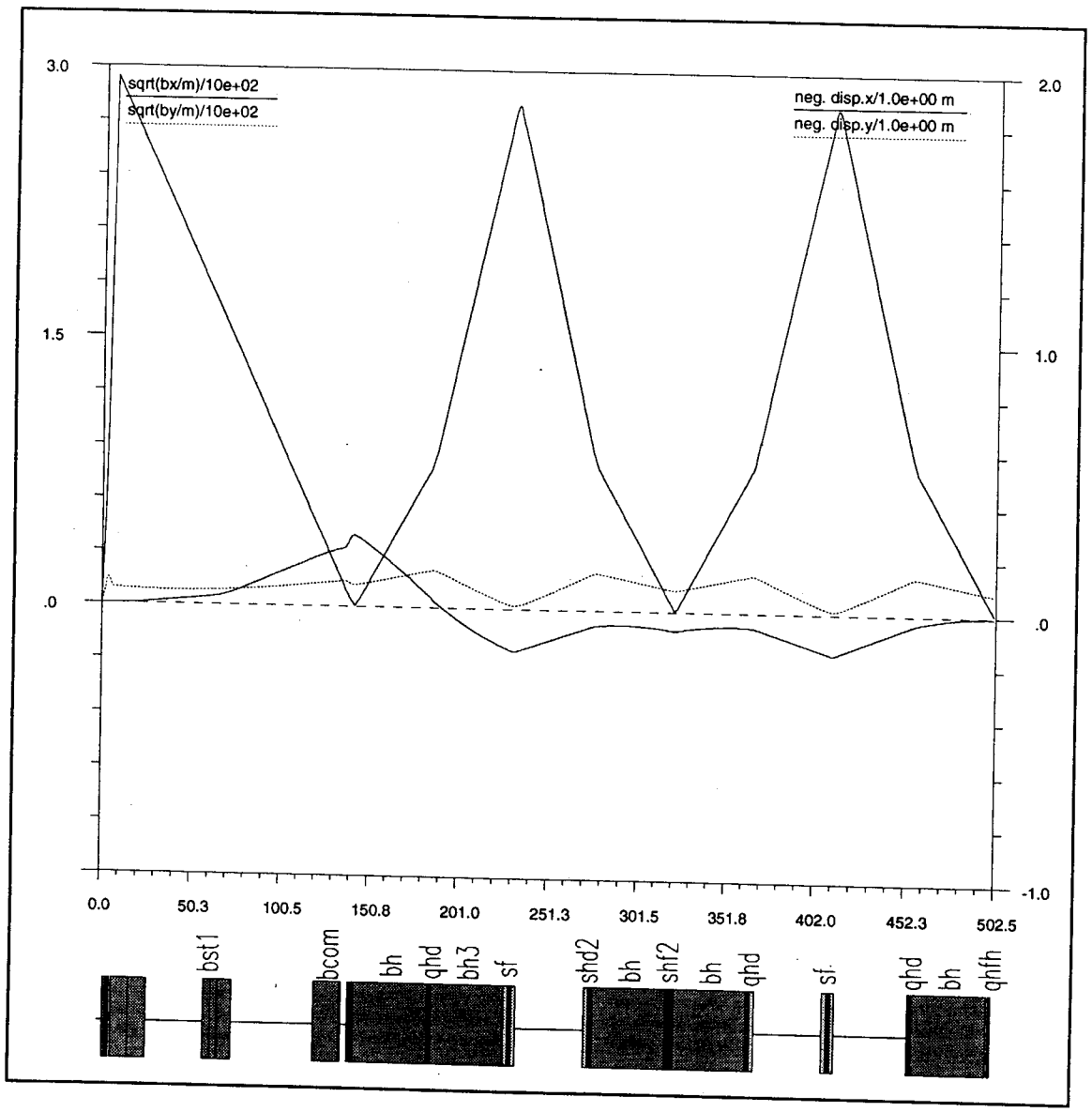

Figure 8.15:
β-functions and dispersion functions for the TESLA spent beam optics from the IP to the end of the chromaticity correction section. The bottom line symbolizes the optical components and includes labels which have been used in the COMFORT input.

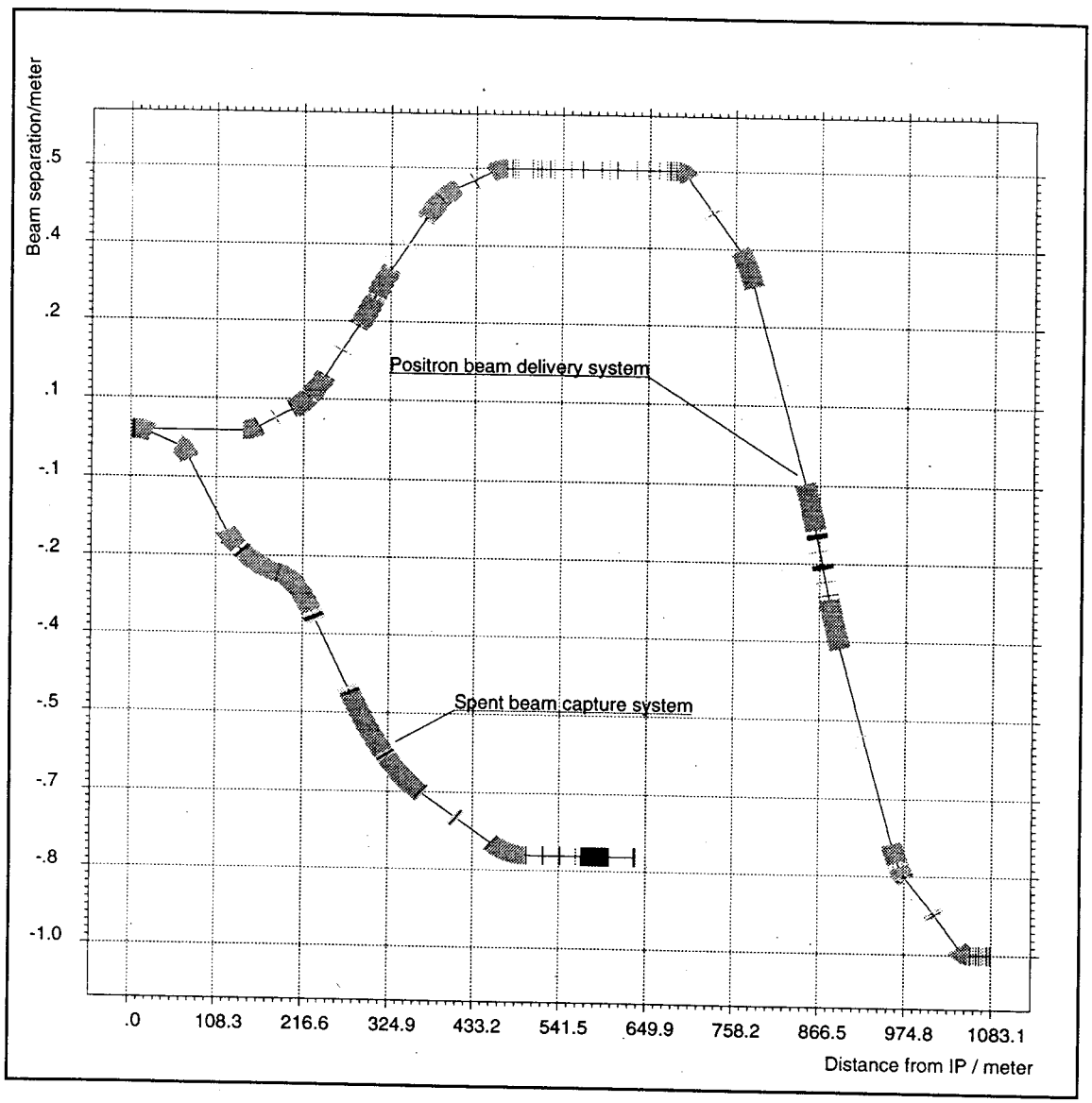

Figure 8.16:
Spent beam capture system for TESLA continued with the 35 m long wiggler (lower branch), and the oncoming positron beam (upper branch).

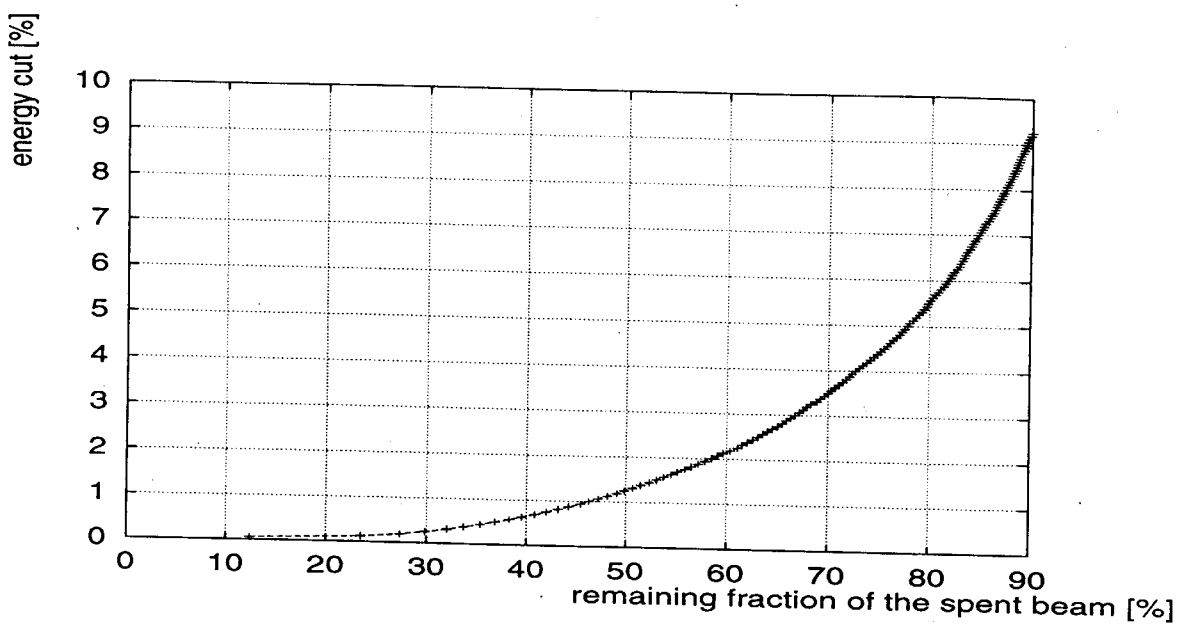

Figure 8.17: *Remaining fraction of the spent beam as a function of the energy cut at the end of the TESLA chromaticity correction section. This figure is useful in combination with fig.(8.18) and fig.(8.19).*

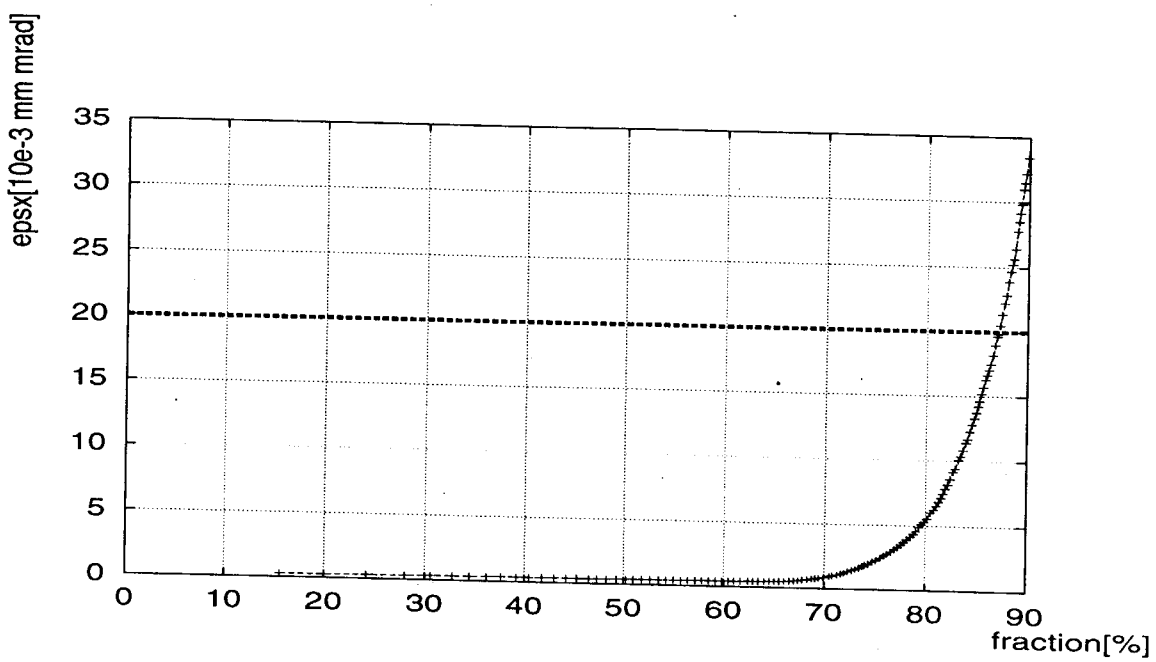

Figure 8.18: *Horizontal emittance as a function of the remaining fraction of the spent beam at the end of the chromaticity correction section. The energy cut, corresponding to the spent beam fraction is shown in fig.(8.17) The emittance requirements (shown by the thick line) for the unpolarized source are fulfilled for a* ≈ 87 *% of all particles. This fraction corresponds to an energy cut* $|\Delta E/E| < 0.07$.

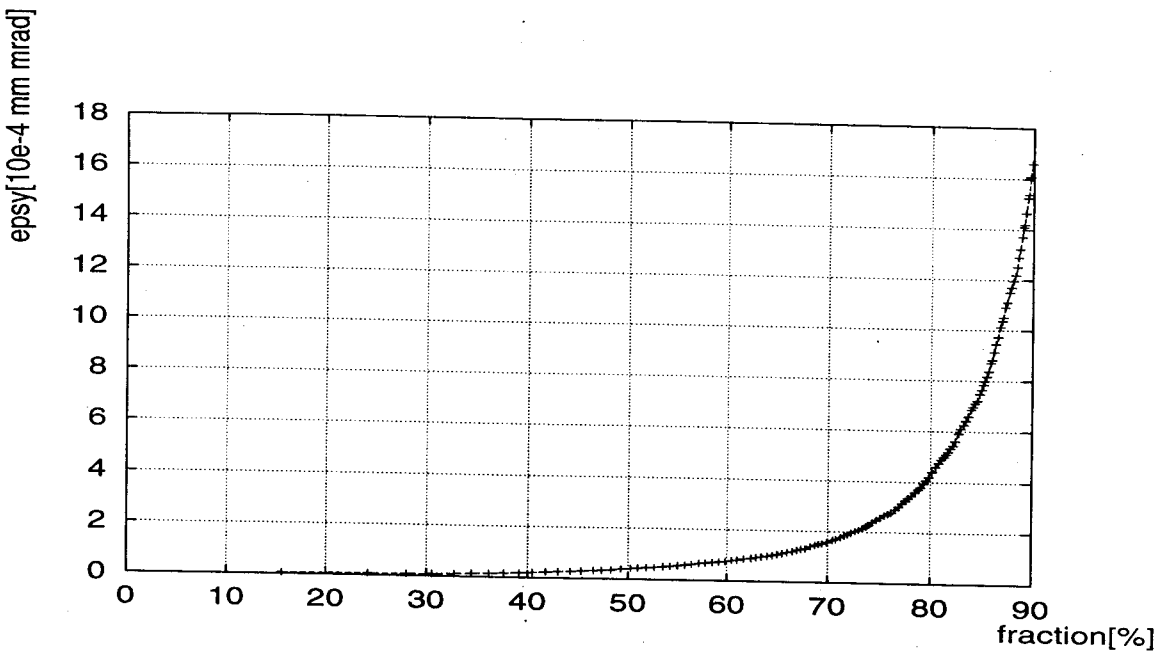

Figure 8.19: *Vertical emittance as a function of the remaining fraction of the spent beam at the end of the chromaticity correction section. The energy cut, corresponding to the spent beam fraction is shown in fig.(8.17)*

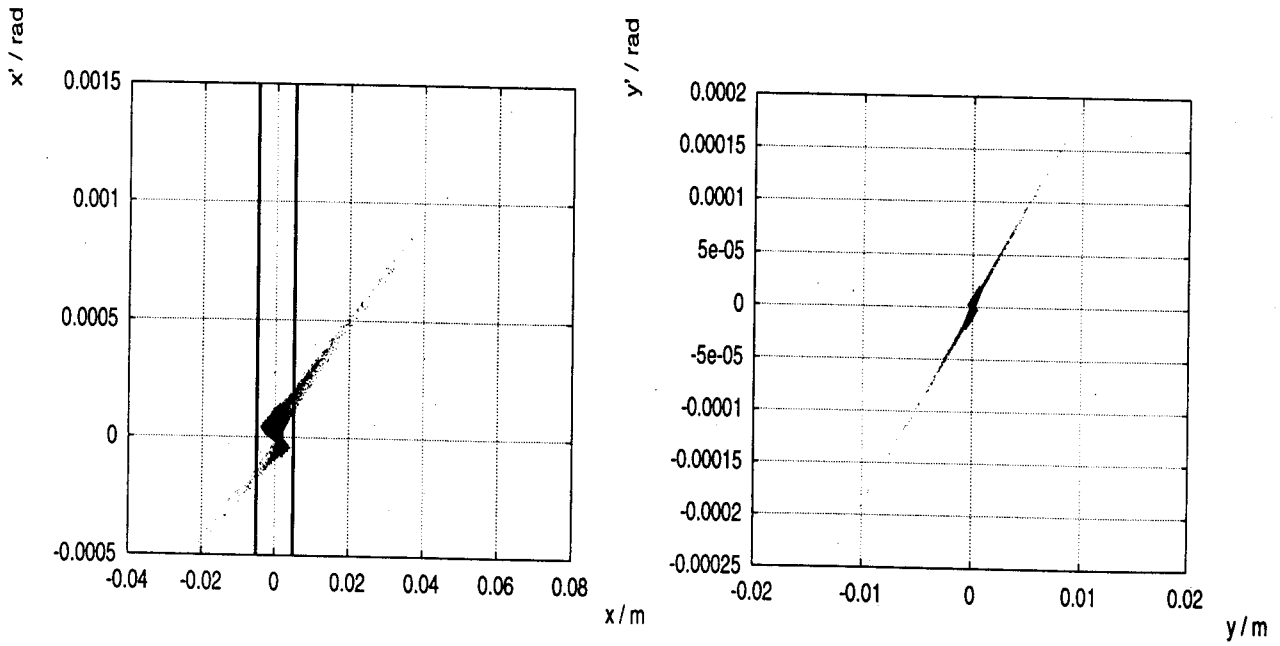

Figure 8.20:
Left: Horizontal phase space at the end of the first collimator region between 27.51 and 59.51 m behind the IP. Right: Vertical phase space in the same position.

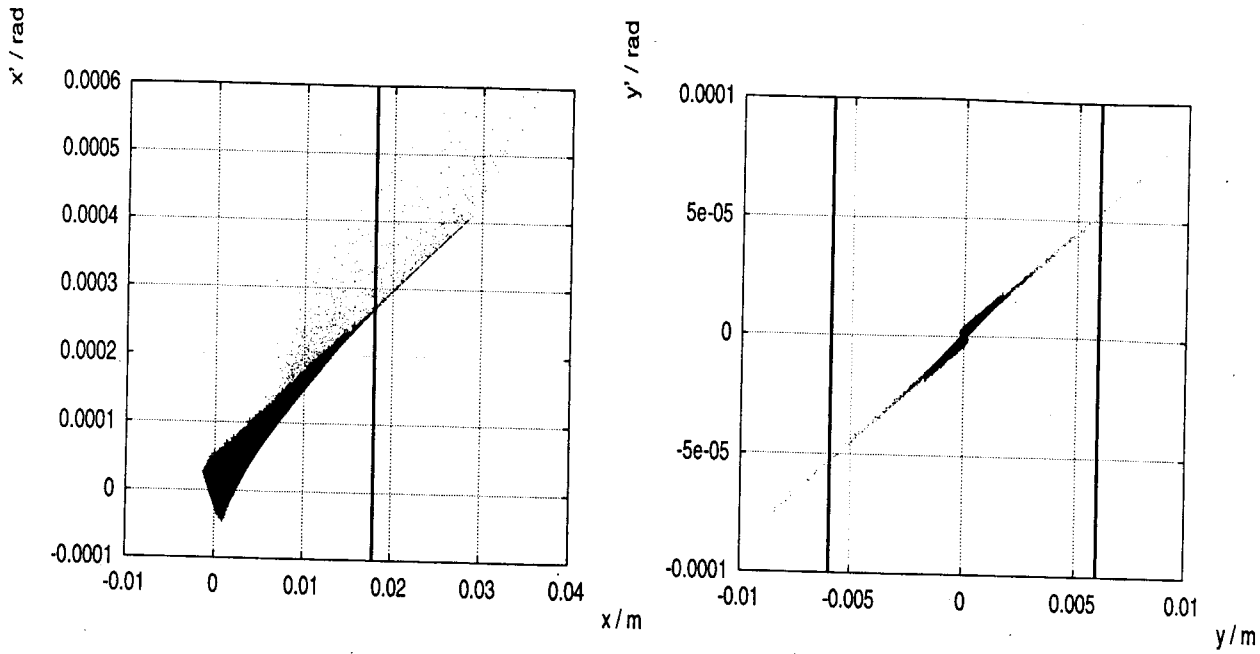

Figure 8.21:
Left: Horizontal phase space at the end of the 2nd collimator region between 75.51 and 122.12 m behind the IP. Right: Vertical phase space in the same position.

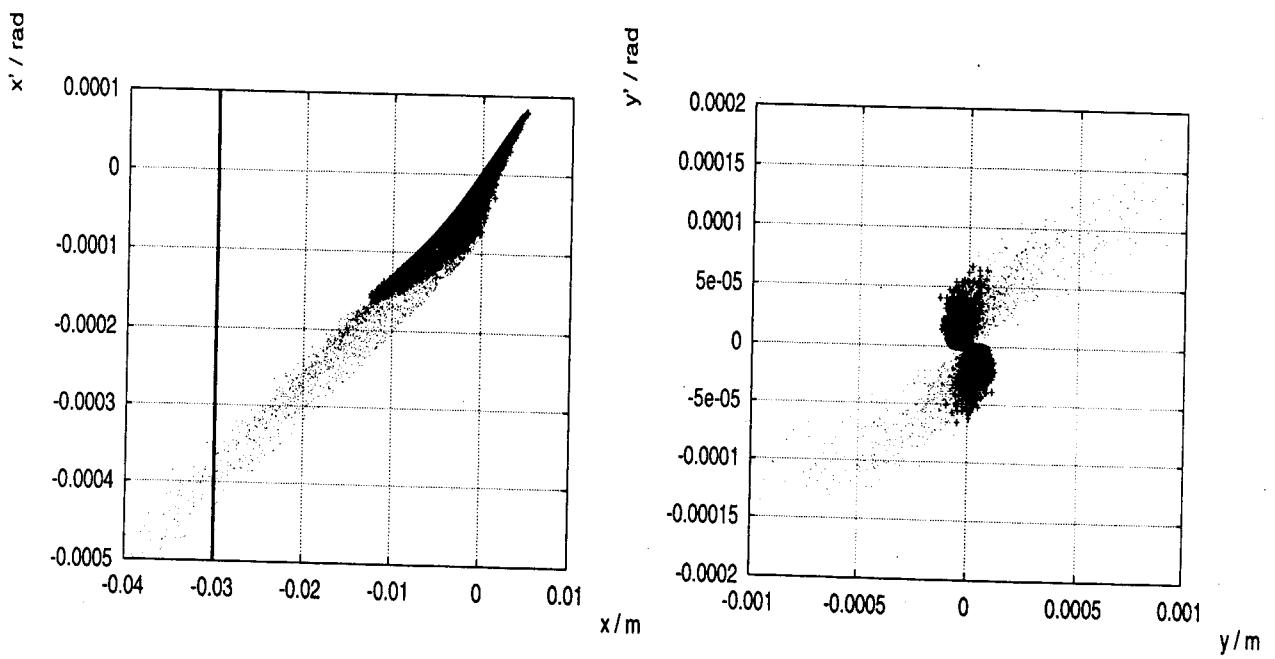

Figure 8.22:
Left: Horizontal phase space at the end of the 3rd collimator region between 188.64 and 229.14 m behind the IP. Right: Vertical phase space in the same position.

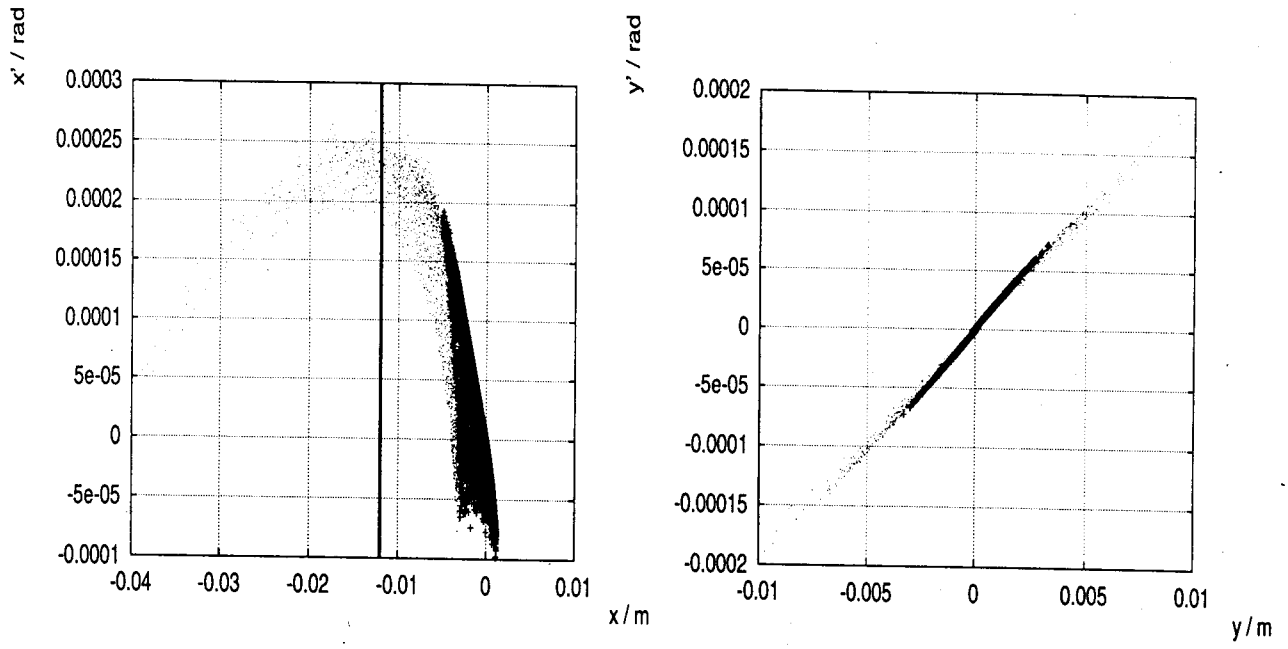

Figure 8.23:
Left: Horizontal phase space at the end of the 4th collimator region between 235.89 and 274.14 m behind the IP. Right: Vertical phase space in the same position.

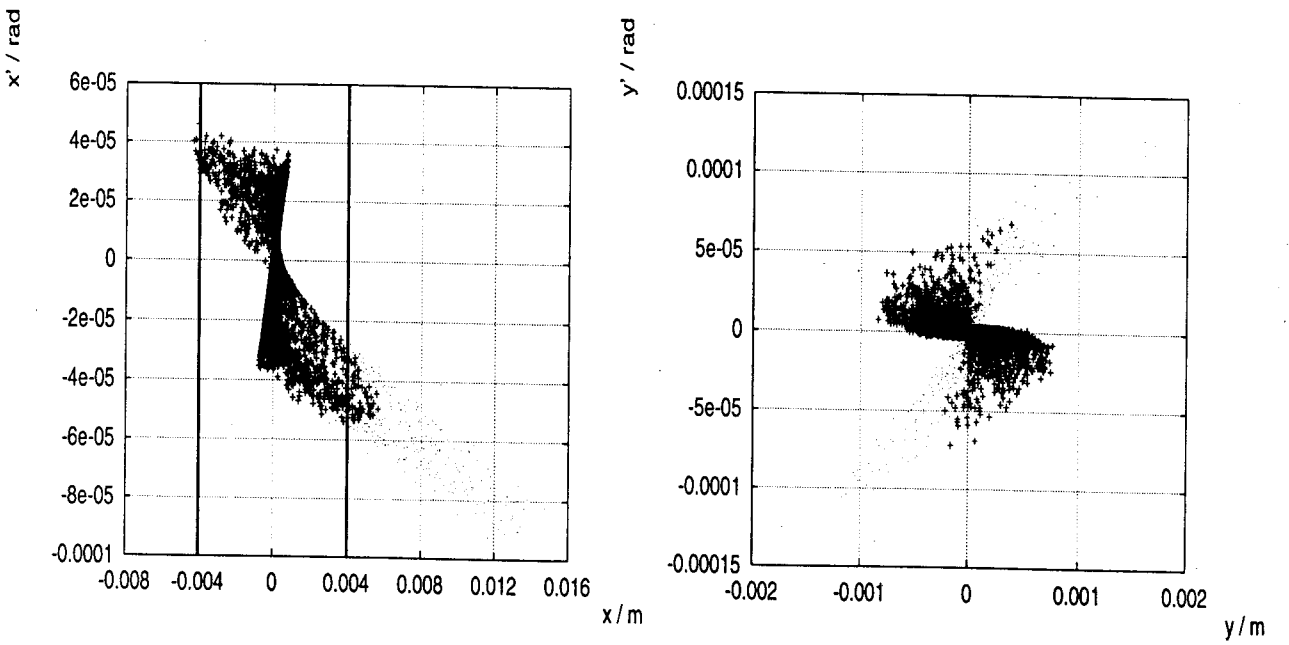

Figure 8.24:
Left: Horizontal phase space at the end of the 5th collimator region between 502.52 and 522.74 m behind the IP. Right: Vertical phase space in the same position.

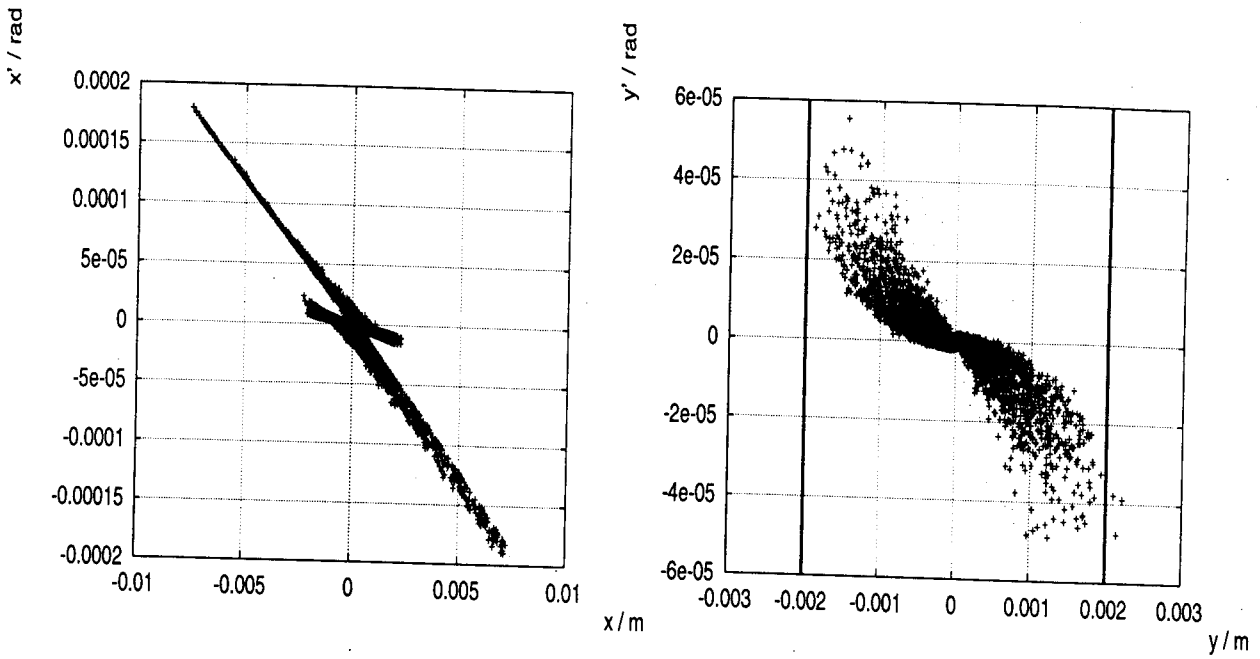

Figure 8.25:
Left: Horizontal phase space at the end of the 6th collimator region between 547.74 and 552.74 m behind the IP. Right: Vertical phase space in the same position.

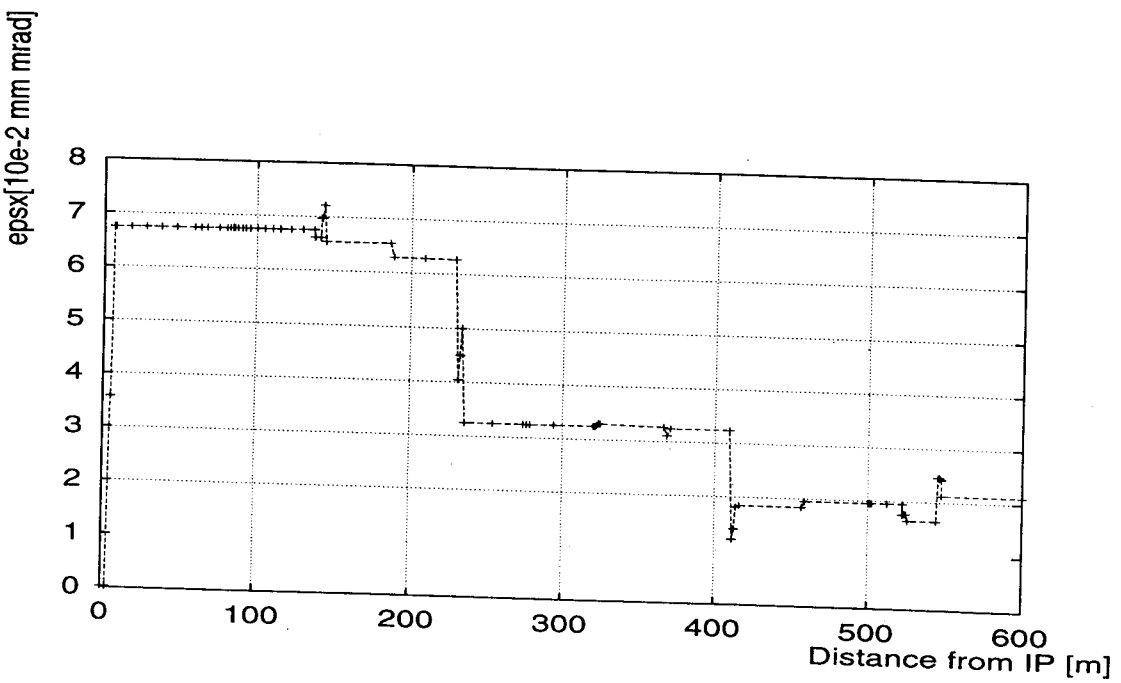

Figure 8.26: *Horizontal emittance along the spent beam capture system for TESLA for the ensemble corresponding to* $|\Delta E/E| < 0.07$. *After the rms-emittance (eq.(8.8) is increased by the final focus quadrupoles, the emittance decreases in the position of the sextupoles. At the beginning of the wiggler, the horizontal emittance is* $\approx 2 \cdot 10^{-2}$ *mm mrad.*

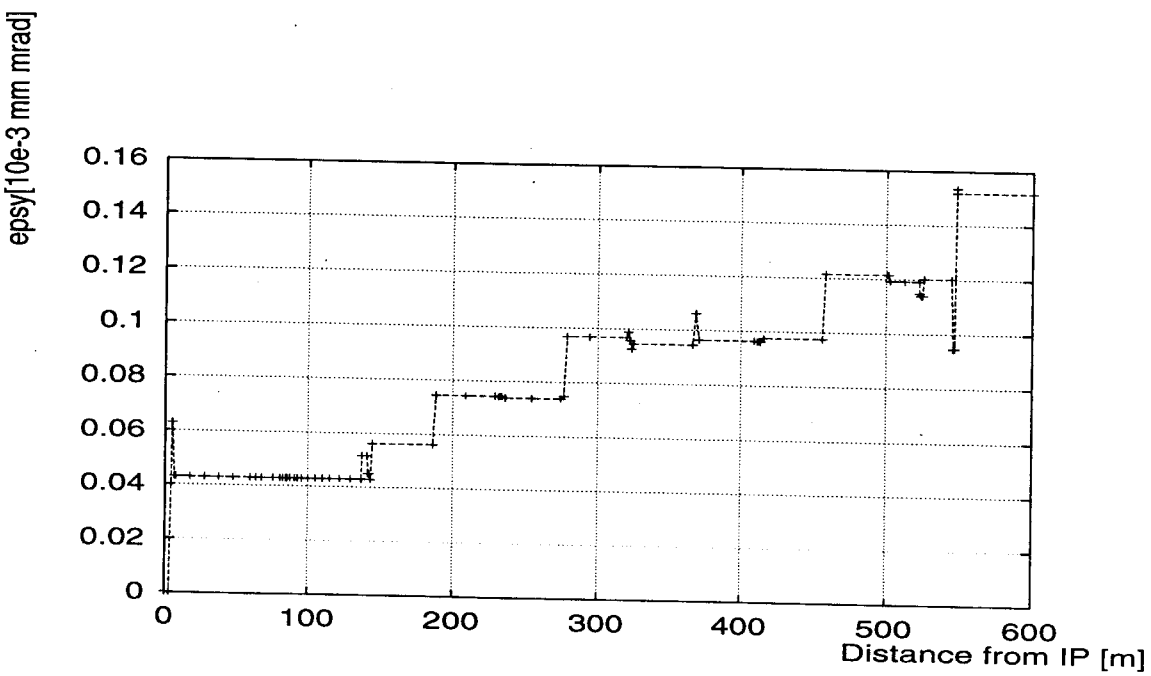

Figure 8.27: *Vertical emittance along the spent beam capture system for TESLA for the ensemble corresponding to* $|\Delta E/E| < 0.07$. *The emittance rises continuously along the spent beam capture system because the vertical chromaticity is not corrected. At the beginning of the wiggler, the vertical emittance is* $\approx 1 \cdot 10^{-3}$ *mm mrad.*

Collimator	Position behind IP [m]	Beam power to be removed [kW]
C1	27.51-59.51	356.19
C2	75.51-122.12	372.52
C3	188.64-229.14	74.6
C4	235.89-274.14	144.48
C5	502.52-522.52	212.33
C6	547.74-552.74	1.88

Table 8.5:
Collimator positions and collimated beam power for TESLA referred to fig.(8.15), fig.(8.28) and fig.(8.29)

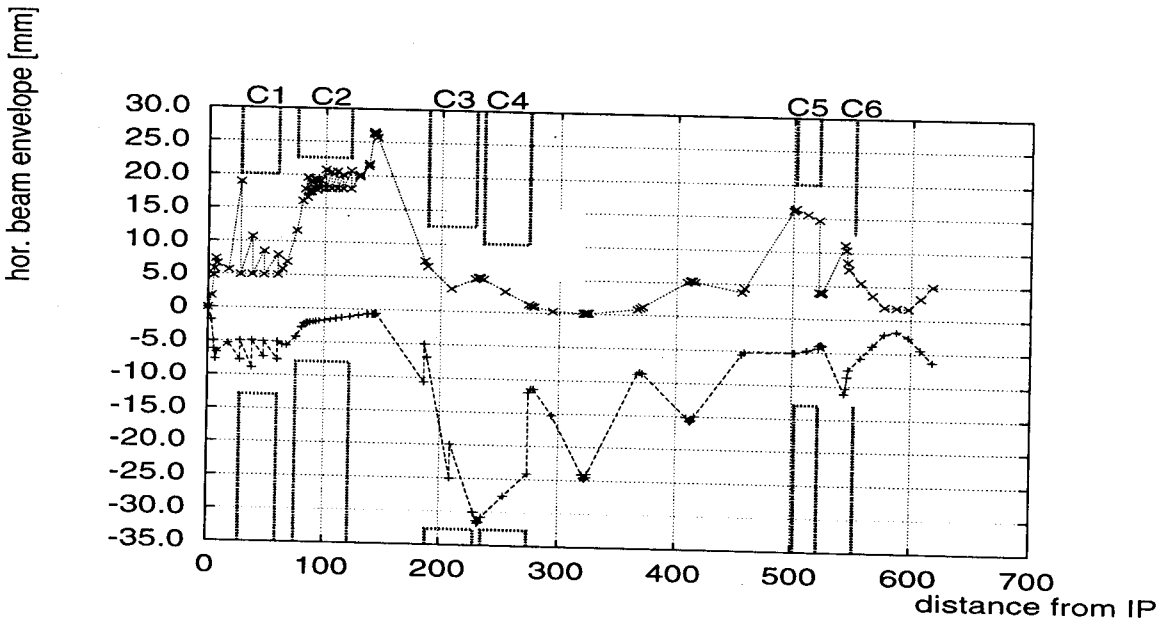

Figure 8.28: *Horizontal envelope of the disrupted beam passing the TESLA spent beam capture system starting from the IP (position 0 m). The wiggler is located in the position 548-583 m.*

8.2.3 The chromaticity correction section and the beam transport through the wiggler for the SBLC

In the case of the SBLC, the spent beam suffers a considerable emittance growth by the nonlinear magnetic fields of the final focus quadrupoles. The origin and the consequences concerning the emittances are discussed in detail in section (8.1.2). Since the spent beam is not focused by the final focus quadrupoles, this must be done as early as possible to keep β-functions small. A half-quadrupole doublet is chosen for this purpose. Each half-quadrupole has a length of 3.5 m. The chromaticity produced by this doublet is comparable is of the same order of magnitude of that in the TESLA case. The vertical emittance is already increased due to the fields of the final focus quadrupoles. Hence there is no freedom to let the vertical emittance grow along the capture system. Therefore the chromaticity correction section consists not only of a horizontal chromaticity correction system but is also supplied with a vertical chromaticity correction system.

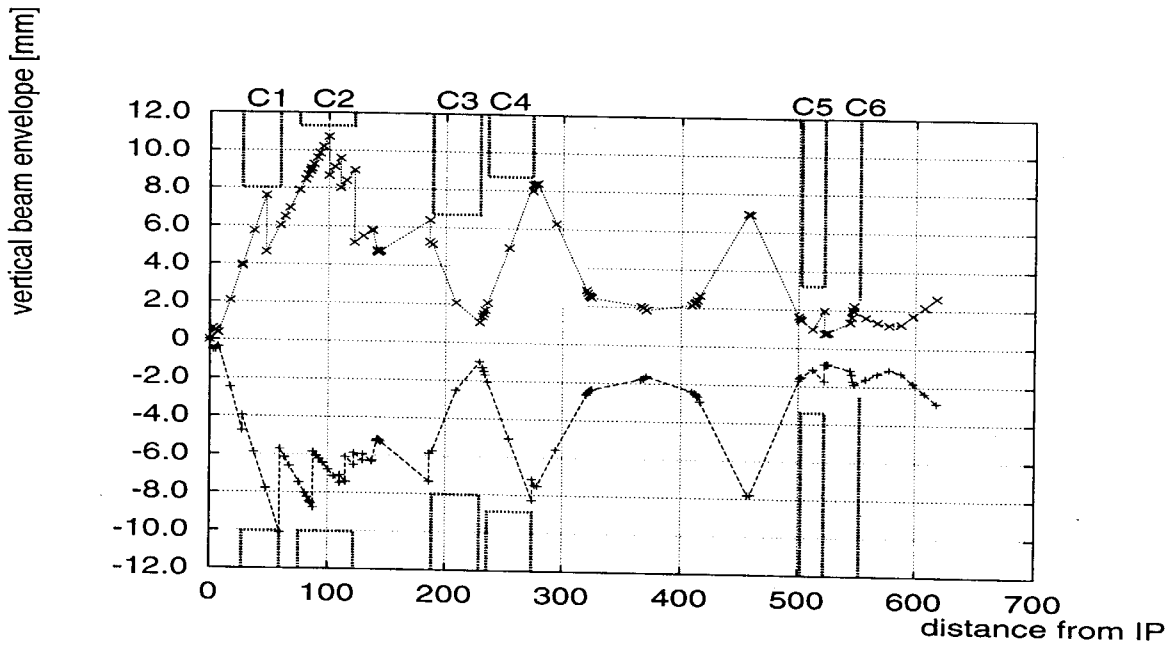

Figure 8.29: *Vertical envelope of the disrupted beam passing the TESLA spent beam capture system starting from the IP (position 0 m). The wiggler is located in the position 548-583 m.*

The difficulties are similar to those in the TESLA case. The capture system, consisting of the matching section (see section (8.1.2)), the chromaticity correction section and the continuation of the optics through the wiggler, must fit into the tunnel of the oncoming beam. In addition, the chromaticity correction section must fulfill the optical requirements for an effective chromatic correction, as explained in section (8.2.1). The initial conditions for the capture system starting at the end of the last final focus quadrupole were matched to the fraction of the spent beam containing particles with energy deviations of $|\Delta p/p| < 0.07$. This subset contains ≈ 85 % of all particles. Based on the experience with the design of the TESLA capture system, this fraction of the spent beam is a reasonable target considering the bandwidth of practical achromatic systems.

In the SBLC, the spent beam is separated from the oncoming beam by the crossing angle of 6 mrad and the additional deflection of 2 mrad due to the dipole component of the fields of the final focus doublet. Hence there is no need for an additional deflection device. The separation is roughly 12 cm in a distence of 10 m behind the final focus quadrupoles which is enough space for the half-quadrupole doublet.

The dispersion created by the final focus quadrupoles is compensated in the matching section, extending from the end of the final focus quadrupoles to the beginning of the chromaticity correction section. The vertical chromaticity correction section, following the matching section, consists of four FODO cells with a phase advance of $\pi/2$ each. The length of each FODO cell is 40 m. Since the dispersion is matched into the chromaticity correction section, the bending magnets inside the vertical chromaticity correction section are only to create the dispersion (and of course to provide a reasonable separation from the oncoming beam). Due to the large initial separation angle of the beam, the direction of the bending magnets of the vertical chromaticity correction section is chosen to deflect the spent beam back into the direction of the oncoming positron beam. The four magnets are positioned following the principle explained in section (8.2.2). The length of the magnets is 18.5 m and the deflection angle is 3.49 mrad. Hence the magnetic field has to be 0.16 T. The main sextupoles are placed at the maxima of the vertical beta functions, with phase advances of π and 2π to the half-quadrupole doublet. The peak of the vertical beta function is inevitably in the position of the horizontal defocusing

quadrupoles. Since the horizontal dispersion shows the same behaviour as single particle trajectories, the main sextupoles for the vertical chromaticity correction are not at the positions of the dispersion maxima. In addition to the main sextupoles (labeled "sd", see fig.(8.30)), the vertical chromaticity correction section is supplied with four additional sextupoles adjacent to the quadrupoles, used to compensate the local chromaticity. At the end of the vertical chromaticity correction section, the distance between the spent beam and the oncoming positron beam is roughly 1.0 m. Here the beam line is deflected back into the direction of the oncoming beam delivery system. Therefore the following horizontal chromaticity correction section is supplied with bending magnets of the same length and strength, but with a different sign of the magnetic field. Hence the sign of the main sextupoles fields is the same as for the vertical chromaticity correction section although the chromaticity is corrected in a different plane. Since the ratio β_y/β_x is small, the horizontal chromaticity is corrected without increasing the vertical chromaticity.

The structure of the horizontal chromaticity correction section is the same as that of TESLA. The optical functions along the matching section and the chromaticity correction section, starting at the exit of the final focus quadrupoles, are shown in fig.(8.30). The geometry of the spent beam capture system with respect to the beam delivery system is shown in fig.(8.31) in which the chromaticity correction section is followed by a 35 m long wiggler.

After fixing the design of the beam line and performing the chromatic fit, the data set representing the beam after the IP was tracked through the capture system until the end of the chromaticity correction section. The beam properties were analyzed as described in section (8.2.2). The horizontal and vertical emittances plotted as functions of the energy dependent fraction of the beam are shown in fig.(8.33) and fig.(8.34), respectively. The vertical emittance growth is small in comparison to the maximum tolerable value of $5 \cdot 10^{-3}$ mm mrad. As seen in fig.(8.33), the horizontal emittance requirements of $2 \cdot 10^{-2}$ mm mrad can be fulfilled for roughly 87 % of the initial beam. As explained in the case of the TESLA capture system, the scraping of the beam is done according to the particles energy deviation. The collimators were positioned along the beam line starting at the exit of the final focus quadrupoles. At the end of the chromaticity correction section (including the collimators), the beam properties were estimated to continue the capture system. A quadrupole triplet is positioned after a drift space of 20 m. The beam is focused such that the radiation emitted in the 35 m long wiggler hits the target in a focal point 20 m behind the wiggler, i.e. 60 m behind the quadrupole triplet. The electron beam can be separated from the wiggler-radiation over a distance of 20 m between the end of the wiggler and the target. A magnetic field of 1.15 T is required to achieve a separation of 0.3 m between the electron beam and the radiation (due to the energy loss during the interaction and inside the wiggler, the particles have only an energy of 235 GeV). The horizontal radiation spot size on the target is roughly 0.9 mm which is greater than the required spot size of 0.7 mm. The effect of a lower capture efficency is compensated by the vertical radiation spot size of 0.5 mm (see fig.(6.2)).

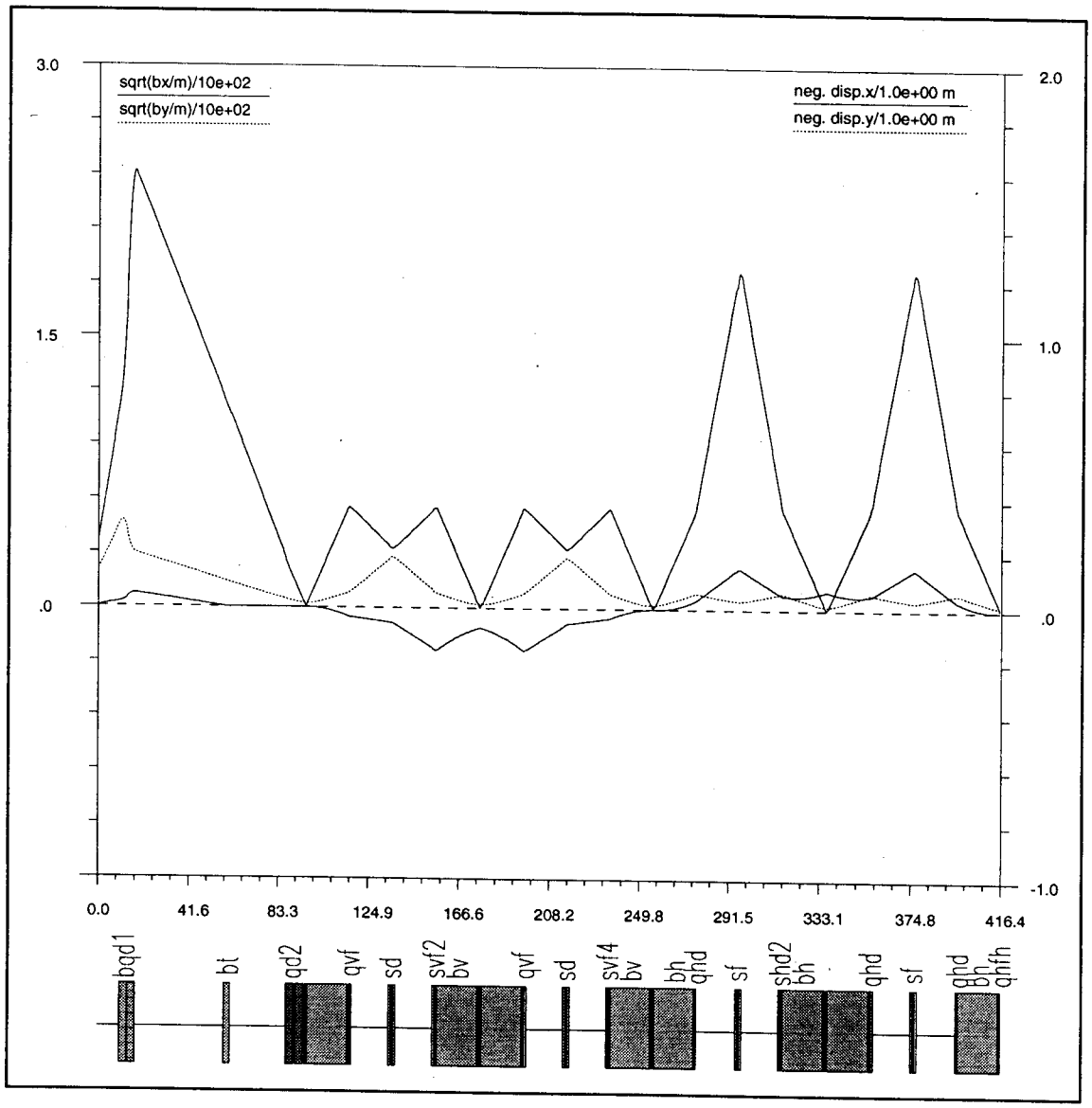

Figure 8.30:
β-functions and dispersion functions for the SBLC spent beam optics from the IP to the end of the chromaticity correction section. The bottom line symbolizes the optical components and includes labels which have been used in the COMFORT input. The IP is located 5.8 m before the position 0 m.

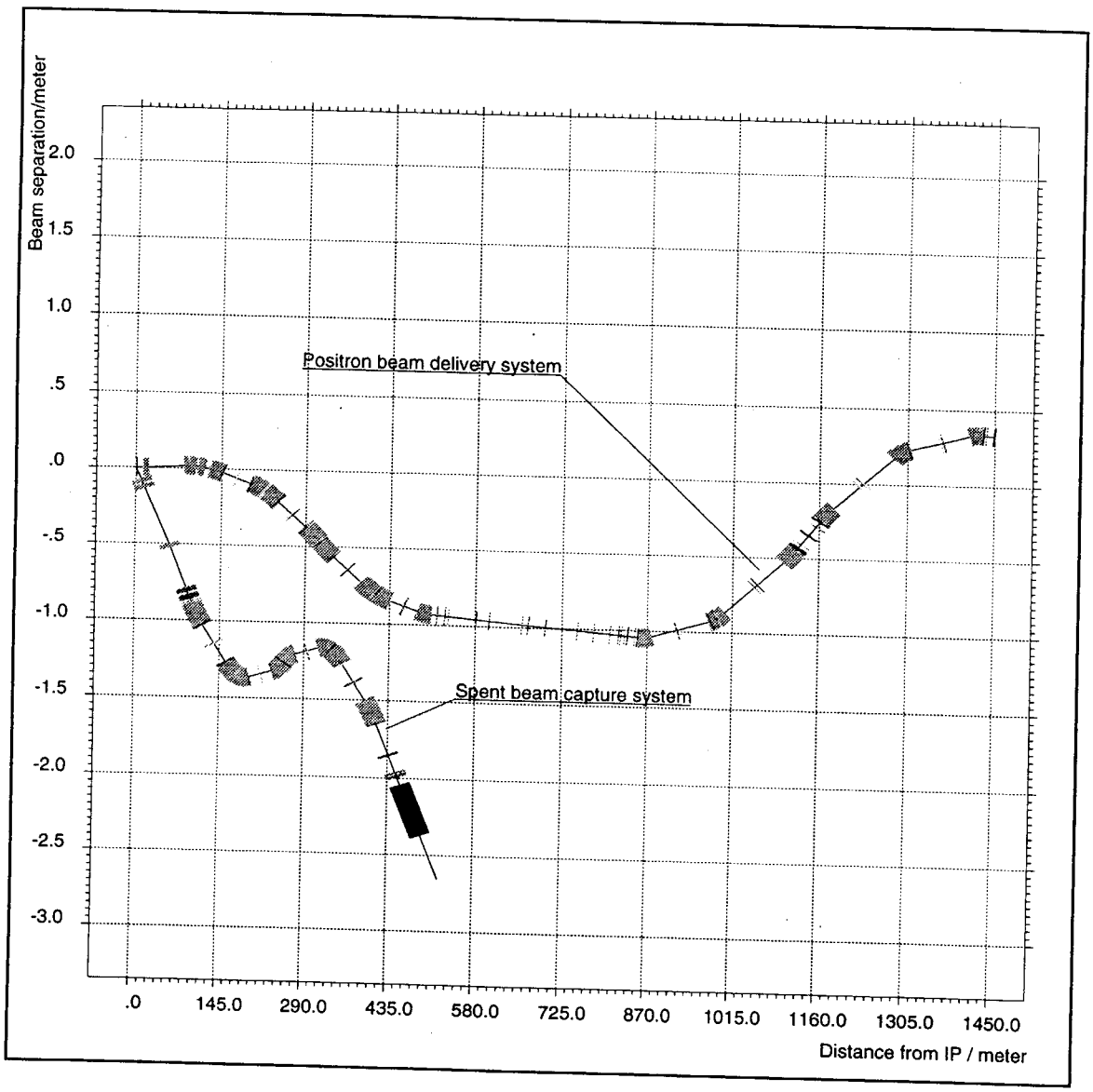

Figure 8.31:
Beam line of the disrupted beam of the SBLC showing the spent beam capture system and the 35 m long wiggler (lower branch) together with the oncoming positron beam (upper branch).

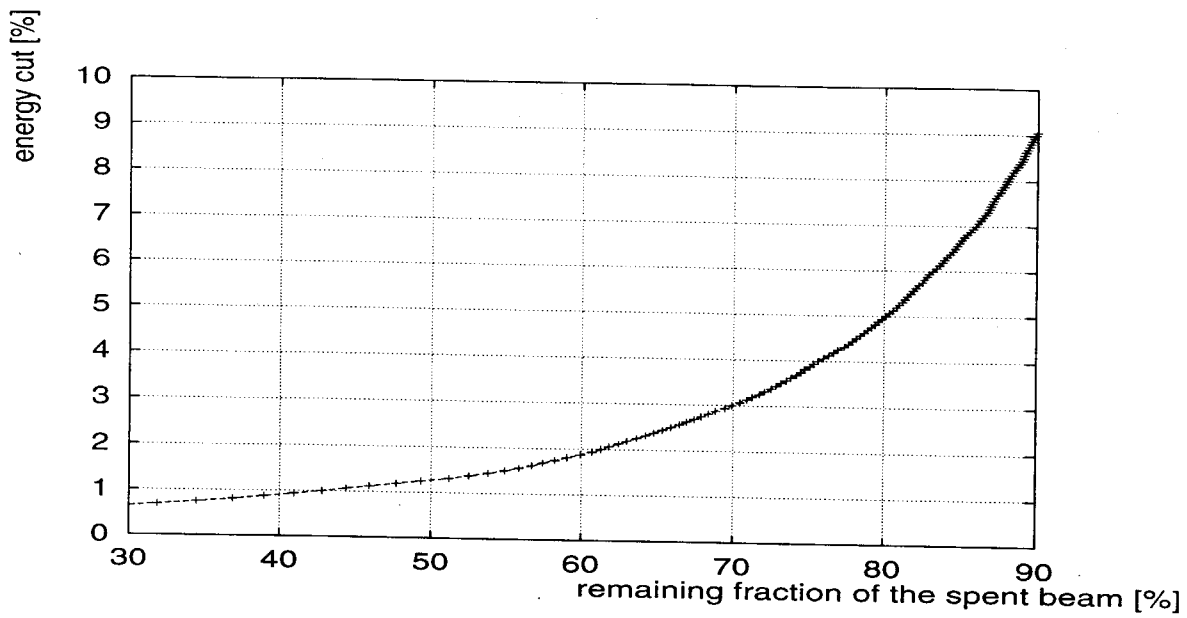

Figure 8.32: *Remaining fraction of the spent beam as a function of the energy cut at the end of the TESLA chromaticity correction section. This figure is useful in combination with fig.(8.33) and fig.(8.34).*

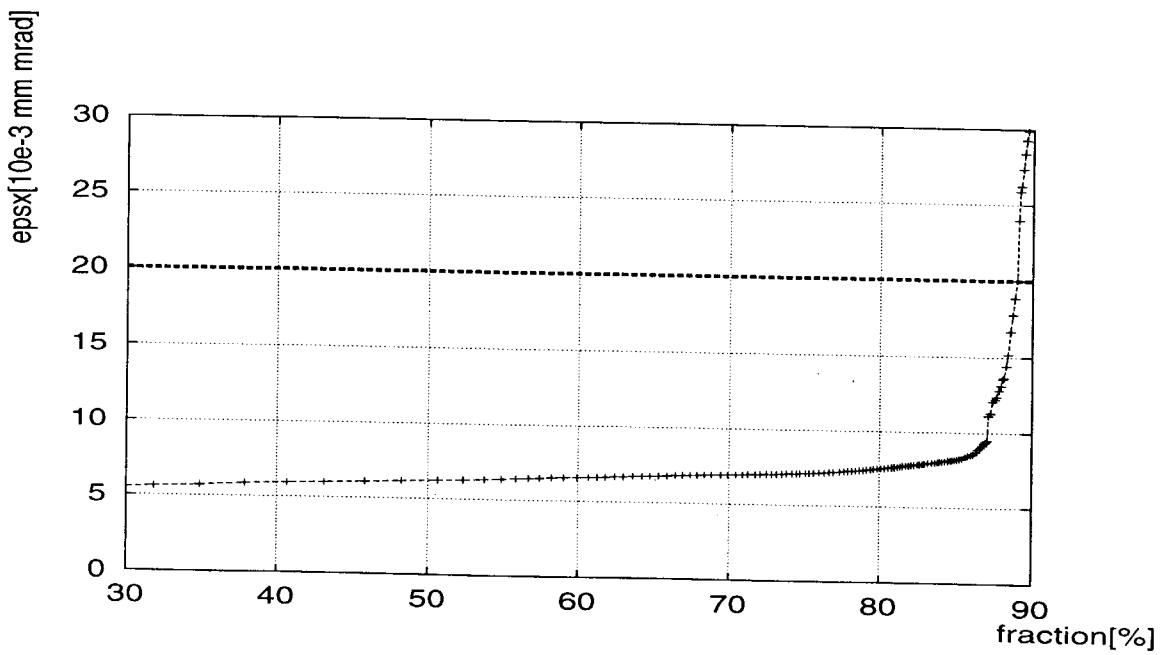

Figure 8.33: *Horizontal emittance as a function of the remaining fraction of the spent beam at the end of the chromaticity correction section. The energy cut, corresponding to the spent beam fraction is shown in fig.(8.32) The emittance requirements (shown by the thick line) for the unpolarized source are fulfilled for a* ≈ 87 *% of all particles. This fraction corresponds to an energy cut* $|\Delta E/E| < 0.07$.

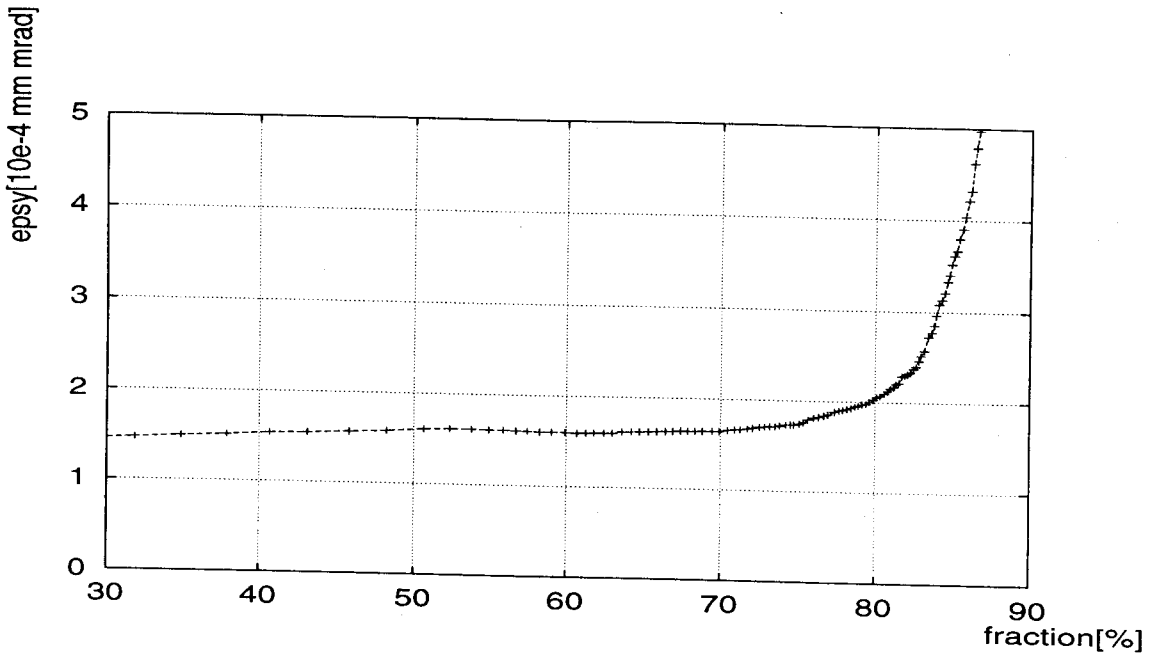

Figure 8.34: *Vertical emittance as a function of the remaining fraction of the spent beam at the end of the chromaticity correction section. The energy cut, corresponding to the spent beam fraction is shown in fig.(8.32)*

The phase space distributions at the collimator positions and the collimator cuts are shown in appendix C. The collimator positions and the corresponding collimated beam power along the capture system are collected in tab.(8.6). The highest collimated beam power per unit length occurs at collimator position C2. Along a 26 m long drift space, a total power of 305 kW has to absorbed, i.e. 11.6 kW per meter. Fig.(8.37) and fig.(8.38) show the horizontal and vertical beam envelopes along the SBLC capture system. Downstream of the last collimators, the beam envelopes grow along the path through the wiggler, particularly in the horizontal plane. This does not imply that the beam (actually the photon beam because the spent electron beam is deflected immediately after the wiggler) is not focused onto the target. These extreme trajectories have energy deviations at the limits of the energy bandwidth of the achromatic system. Thus the beam envelope in this region is determined by the low energy particles which are defocused, although the core of the beam is focused on the target.

It is concluded that an unpolarized wiggler-based positron source using the spent electron beam can also be realized for the SBLC. The results of this section have been estimated based on the design operation of the linac. Problems related to deviations from the design interaction (for example a beam-beam offset at the IP) are discussed in chapter (9).

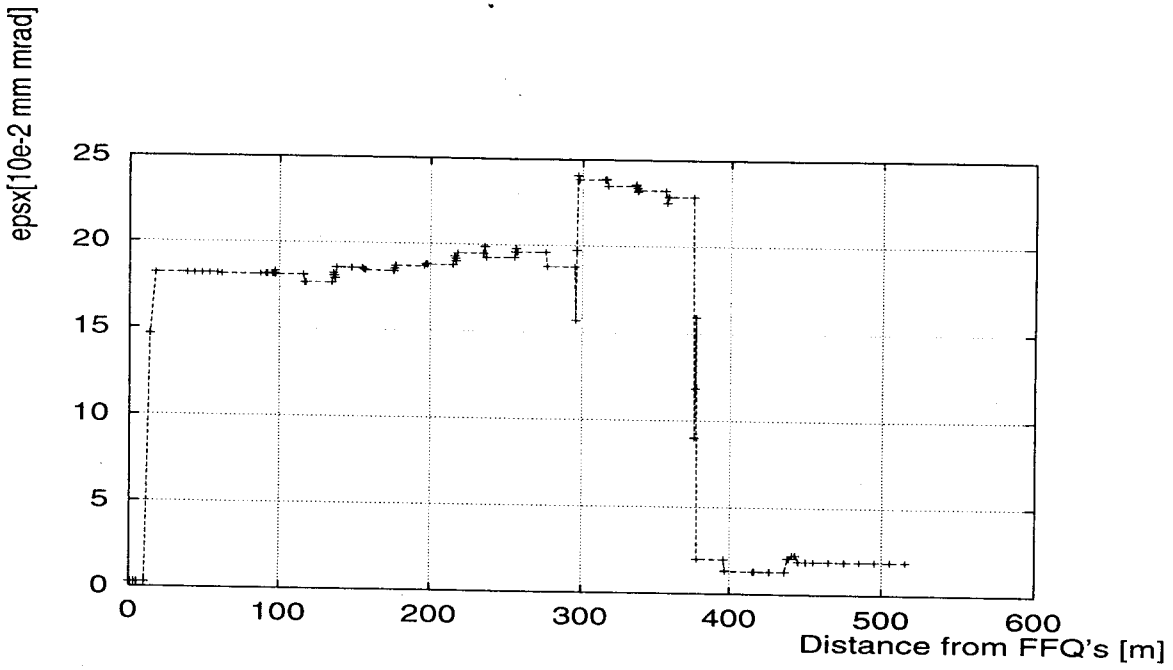

Figure 8.35: *Horizontal rms-emittance (eq.(8.8)) along the spent beam capture system for the SBLC for the $|\Delta E/E| < 0.07$ ensemble starting at the exit of the final focus quadrupoles. The emittance is increased by the half-quadrupole doublet and decreases along horizontal chromaticity correction section in the position of the main sextupoles. The wiggler is located 450-485 m from the exit of the final focus quadrupoles. The horizontal emittance in this position is roughly $2 \cdot 10^{-2}$ mm mrad.*

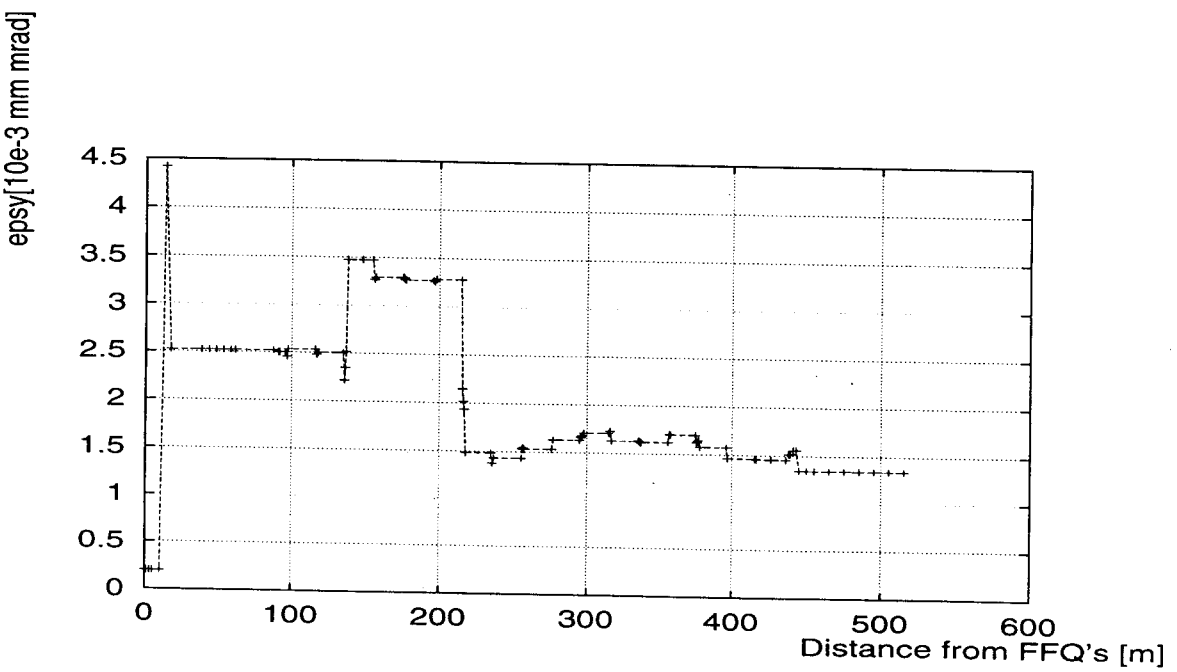

Figure 8.36: *Vertical rms-emittance (eq.(8.8)) along the spent beam capture system for the SBLC for the $|\Delta E/E| < 0.07$ ensemble starting at the exit of the final focus quadrupoles. The emittance is increased by the half-quadrupole doublet and decreases along vertical chromaticity correction section in the position of the main sextupoles. The wiggler is located 450-485 m from the exit of the final focus quadrupoles. The vertical emittance in this position is roughly $1.3 \cdot 10^{-3}$ mm mrad.*

Collimator	Distance from FFQ's [m]	Beam power to be removed [kW]
COL0	0.00-10.00	67.57
COL1	38.23-58.23	70.08
COL2	61.23-87.40	305.02
COL3	137.90-154.90	214.56
COL4	197.90-214.90	27.99
COL5	217.90-234.90	128.50
COL6	377.90-394.90	75.37
COL7	416.40-436.40	41.63
COL8	445.40-450.40	8.17

Table 8.6:
Collimator positions and the beam power which has to be removed for the SBLC. For reference see fig.(8.30), fig.(8.37) and fig.(8.38)

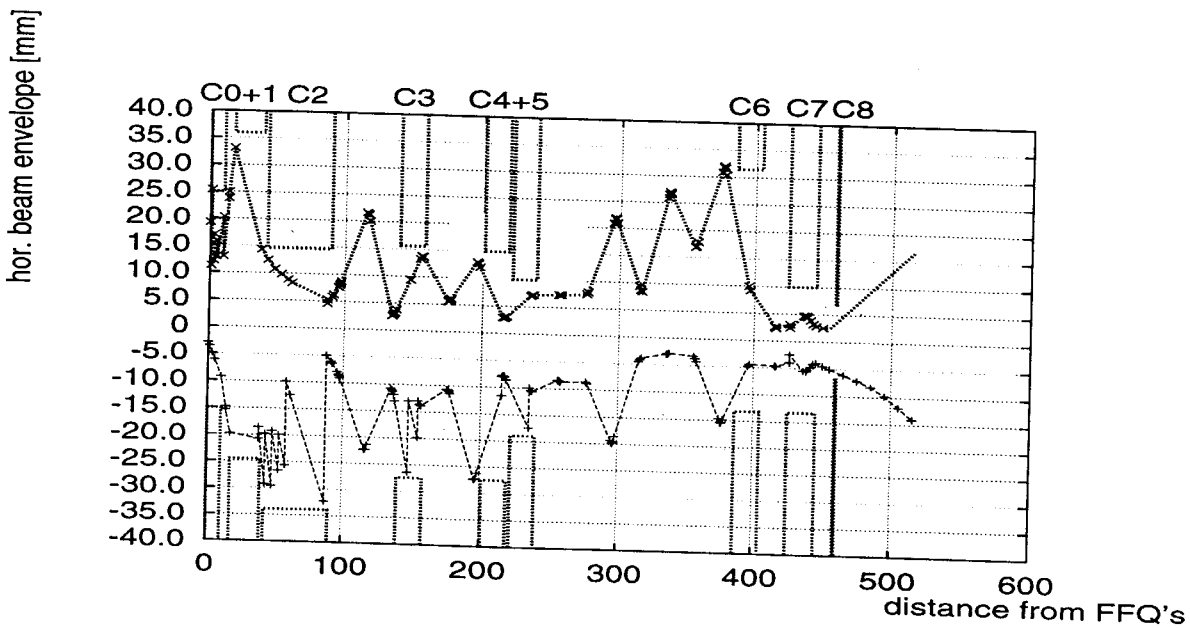

Figure 8.37: *Horizontal envelope of the disrupted beam passing the SBLC spent beam capture system starting from the exit of the final focus quadrupoles (FFQ's). The wiggler is located in the position 450-485 m.*

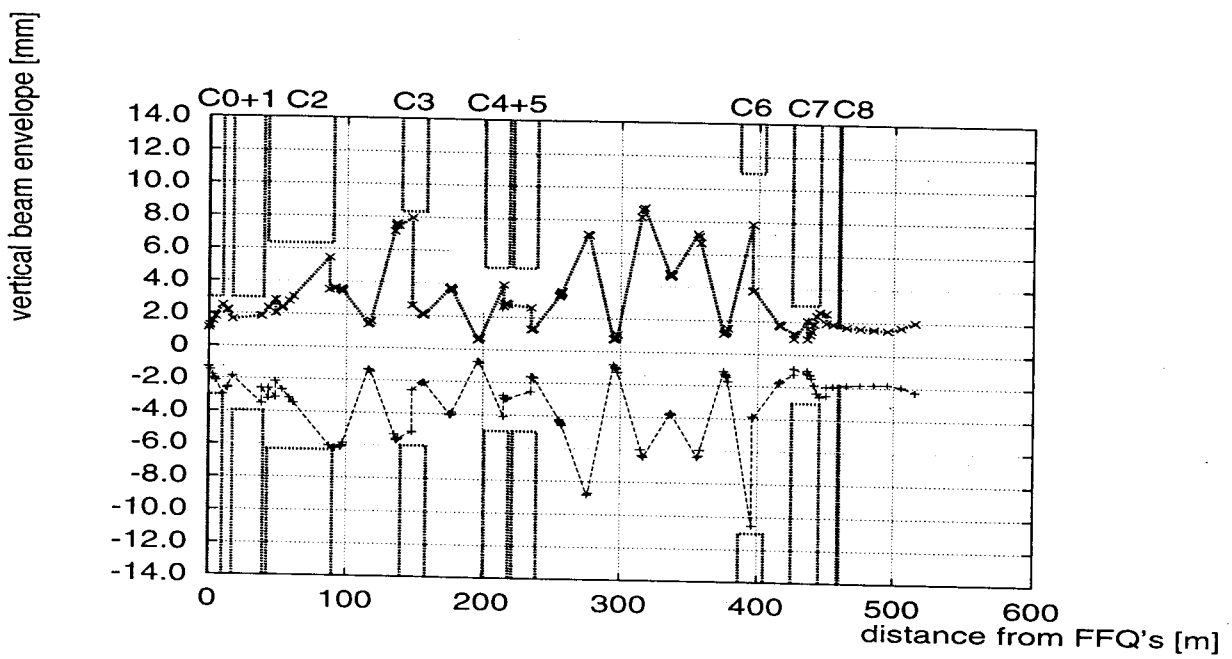

Figure 8.38: *Vertical envelope of the disrupted beam passing the SBLC spent beam capture system starting from the exit of the final focus quadrupoles. The wiggler is located in the position 450-485 m.*

Chapter 9

Operational stability of the positron source using the spent beam

9.1 Bunch charge oscillations due to missing interactions

The efficiency of the capture optics for the disrupted electron beam depends on the properties of the interacting bunches. The optics and the collimation systems described in chapter (8) were developed for bunches interacting with design parameters.

The efficiency of the capture optics is 84.3% for TESLA and 87% for the SBLC, thus for design operation an average yield of 1.19 (TESLA) and 1.15 (SBLC) positrons is required per electron passing the wiggler. The capture efficiency for the disrupted beam depends strongly on the energy spread due to beamstrahlung which is a function of the bunch charge and of other parameters (eq.(7.9)).

Considering a perturbation of the interaction, for example a displacement of the orbit, the spent electron beam suffer less disruption. Hence more electrons would be captured by the spent beam capture system. Assuming a constant converting factor of 1.19 (TESLA) and 1.15 (SBLC), the subsequent positron bunch trains would have a higher charge, which results in a higher energy spread of the spent beam after the IP. Given the fixed energy acceptance of the capture optics, a smaller fraction of the electron beam is available for photon production. Thus, in the next interaction after the initial perturbation, the positron bunches of the next bunch train have a lower charge, and in this way an oscillation of the bunch charge starts. For a stable operation of the linac, such oscillations must be damped.

An investigation of operational stability is done by studying the system under the extreme case of a maximum perturbation i.e. the case that the bunches do not interact at all. The electron beam passes through the collimation system without losses and the positron bunches produced for the next bunch train have a charge 19% (or 15% resp.) larger than designed. The next interaction was simulated with these asymmetric bunch charges. The outgoing disrupted electron beam was tracked through the capture optics to find the efficiency for the following positron bunches. The fraction of the electron beam reaching the wiggler was multiplied with the photon conversion factor to get the asymmetry factor for the next interaction.

Shown in fig.(9.1) and fig.(9.2) is the behavior of the bunch charge as a function of the number of the interactions after the initial perturbation. The oscillations are damped and so the positron source can be operated in a stable manner.

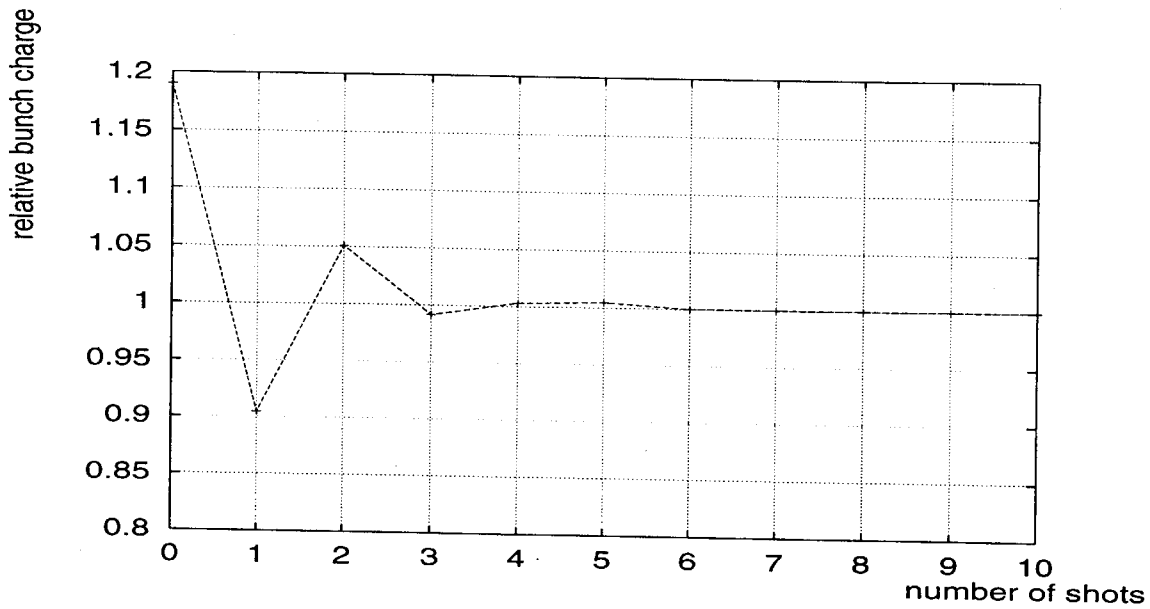

Figure 9.1: *Oscillations of the positron bunch charge after one missing interaction for TESLA. The relative bunch charge reaches the design value after 4 bunch trains after the initial perturbation.*

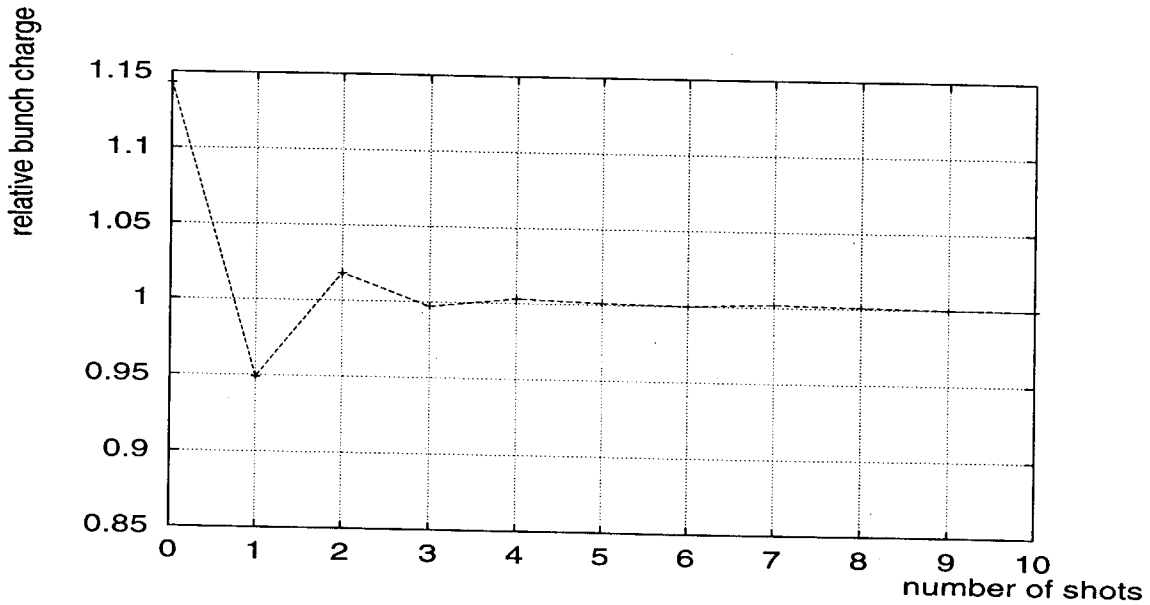

Figure 9.2: *Oscillations of the positron bunch charge after one missing interaction for the SBLC.*

9.2 Effects of beam-beam offsets at the IP

In the case of an interaction of the bunches with a transverse offset, an average deflection occurs i.e. an offset in x' and y' of the phase space distributions of the beam after the interaction. An energy much larger than shown in tab.(8.5) and tab.(8.6) could be deposited in the collimators.

To study this problem, data sets have been produced in which the beam-beam interaction has been simulated for different horizontal and vertical offsets. The height and the step width of the displacements have been chosen according to fig.(7.1) and fig.(7.2) under the assumption that the collective deflection of the whole bunch is of the same order of magnitude as the deflection of a single particle after a design interaction.

Nevertheless, the interaction of the whole bunch has to be simulated because collective effects including disruption and energy loss due to beamstrahlung depend strongly on the displacement. The efficiency of the capture system depends on the energy spread of the spent beam which has also be taken into account. As shown in fig.(8.20) to fig.(8.25) in section (8.2.2) and fig.(C.1) to fig.(C.9) in appendix (C), the positions of the horizontal collimator are asymmetric whereas the few collimators in the vertical plane are positioned symmetric. For this reason, the simulations of horizontal deviations must be performed for both positive and negative offsets.

The average deflection after the interaction is shown in fig.(9.3) and fig.(9.4) for horizontal and vertical displacements, respectively. The collective horizontal deflection qualitatively follows the deflection of single particles shown in the horizontal phase space distributions after the IP. The vertical kick strength increases until a maximum is reached and then decreases with increasing separation between the bunches.

Particle trajectories for different beam offsets were tracked through the spent beam capture system with fixed collimator positions. The power deposited per unit length was plotted as a function of the beam offset in the regions of the collimators with the highest power deposition. The removed power per length in the case of the SBLC are shown in fig.(9.5) and fig.(9.6) for horizontal and vertical offsets, respectively; Figure(9.7) and fig.(9.8) are the corresponding figures for TESLA. Interactions with a horizontal beam offset do not create difficulties. The beam power per meter to be to be removed by the collimators in the case of a horizontal displacement is almost of the same order magnitude as in the case of design operation.

The energy deposited in the collimators with a vertical displacement is much more critical particularly in case of TESLA. Even for the SBLC the deposited power in the collimators per unit length is of the order of 62 kW/m in the 8^{th} and 9^{th} collimators for a displacement Δy of $10\sigma_y$ or 150 nm. For TESLA, the situation is worse. In the last collimator before the wiggler a power of 200-300 kW/m is deposited if the bunches are displaced vertically by Δy of 5-50σ_y. This serious problem has to be investigated in more detail because it is not possible to absorb this amount of energy without producing an intolerable large heat load.

The simplest solution is to distribute the vertical collimators. In the present design for TESLA there is only one vertical collimator just before the wiggler and two vertical collimators for the SBLC. The collimation of the spent beam in the vertical plane in all other collimator positions could be helpful.

In this respect a chromaticity correction in the vertical plane could be advantageous for TESLA. It is to be expected that a lower vertical emittance at the entrance of the wiggler would reduce the fraction of the beam which is to be collimated. An other option is to stretch the capture system. The drift spaces between the elements would be longer and the beam power to be removed by the collimators would be distributed over a larger area. Together

with a stabilization system which is able to avoid critical beam offsets at the IP, the problem of intolerable energy deposition in the collimators should be avoidable. An additional way to ensure safe operation of the spent beam capture system is the presense of an active safety system to dump the beam in the case of intolerable loss rates.

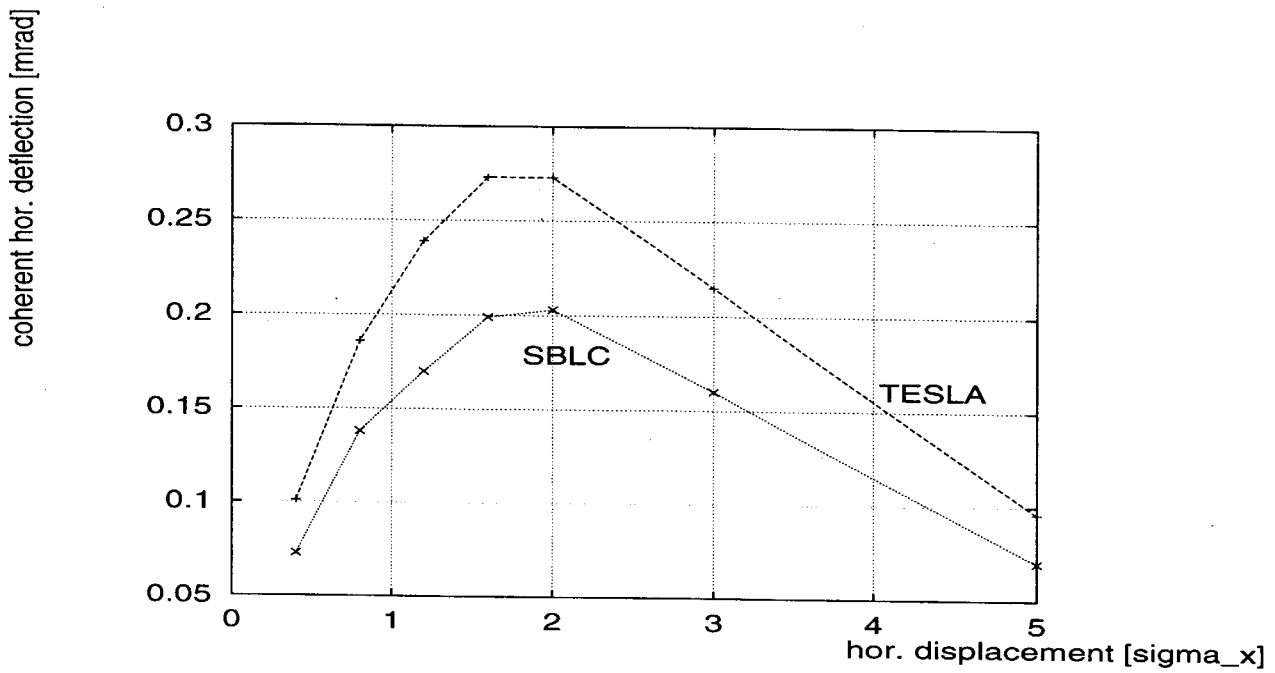

Figure 9.3: *Average deflection of the colliding bunches due to horizontal beam offsets at the IP, for TESLA and the SBLC.*

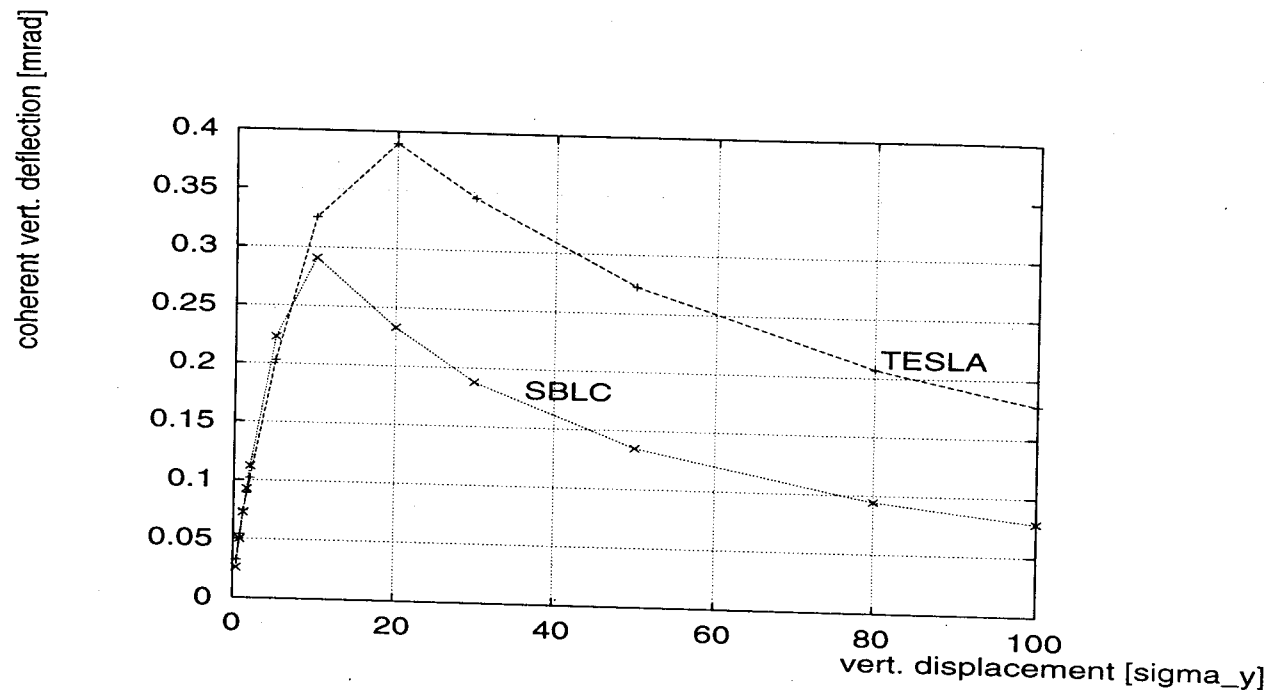

Figure 9.4: *Average deflection of the colliding bunches due to vertical beam offset at the IP, for TESLA and the SBLC.*

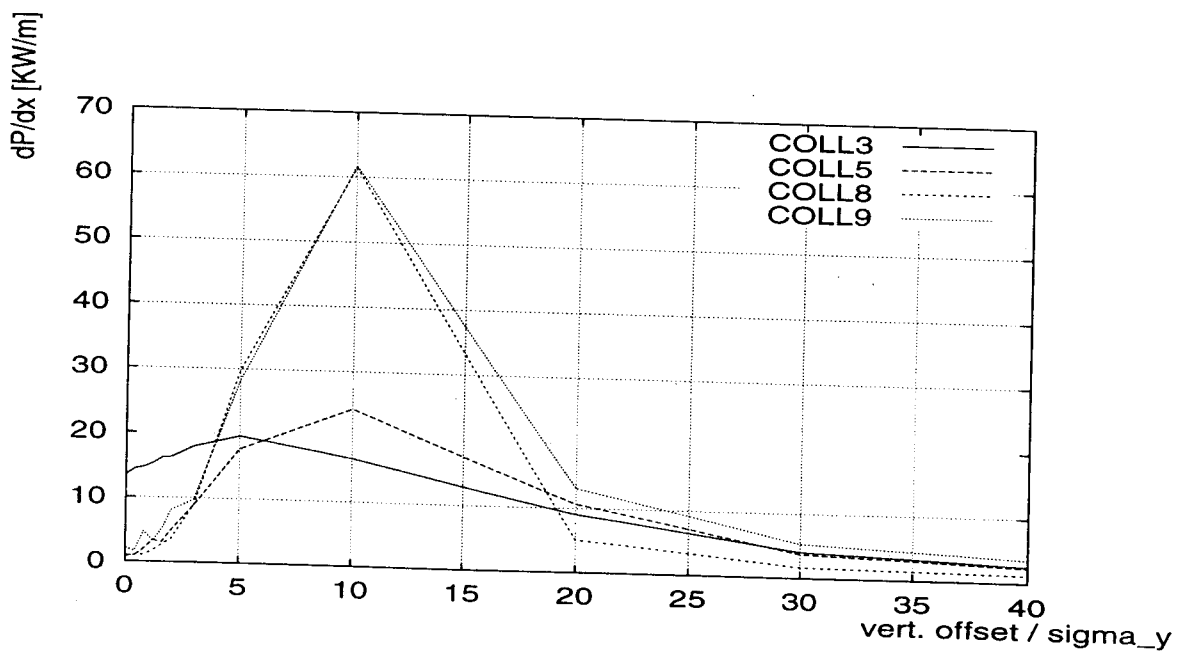

Figure 9.5: *Power deposited per unit length in the collimators COLL3, COLL5, COLL8 and COLL9 as a function of the vertical bunch displacement for the SBLC capture system.*

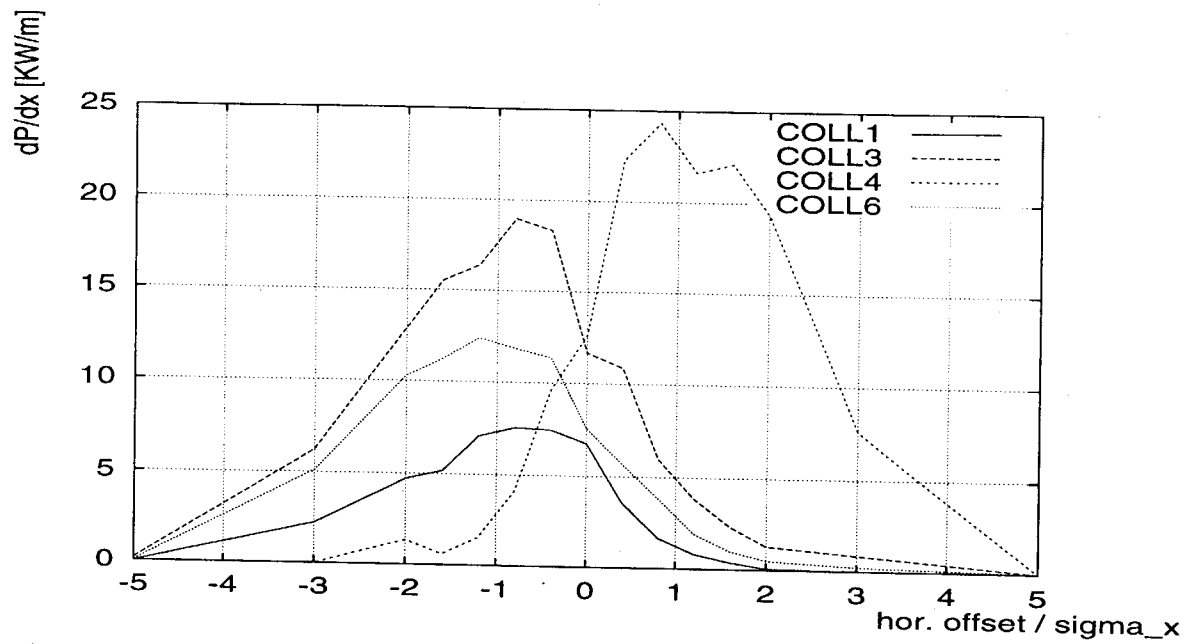

Figure 9.6: *Power deposited per unit length in the collimators COLL1, COLL3, COLL4 and COLL6 as a function of the horizontal bunch displacement for the SBLC capture system.*

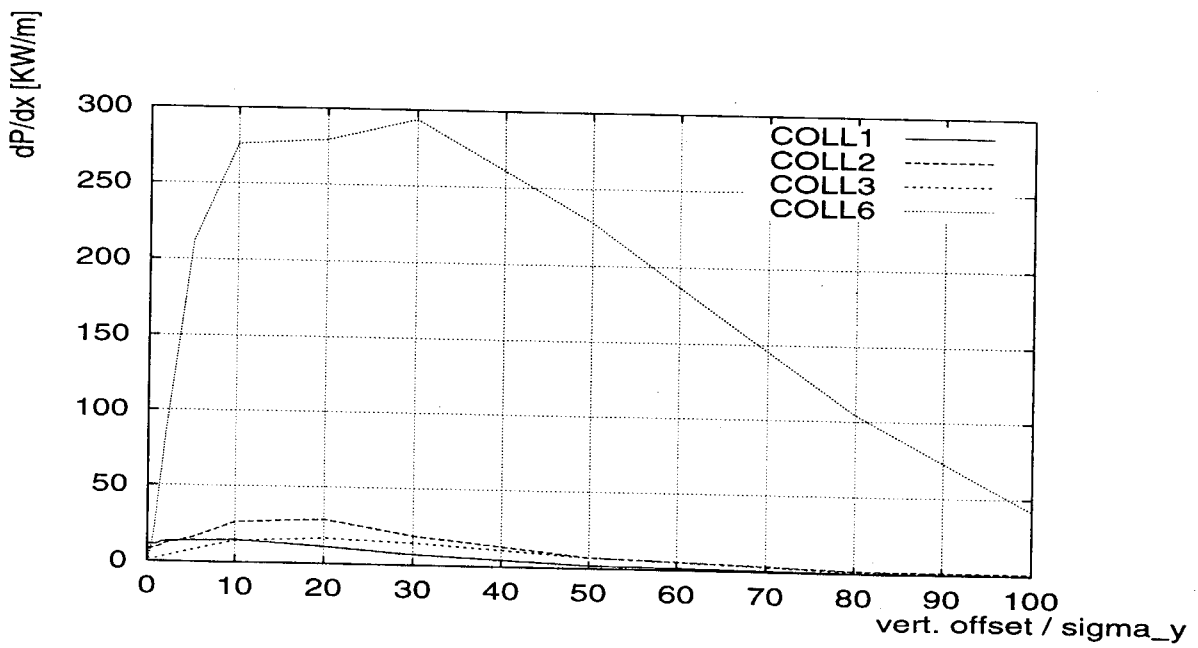

Figure 9.7: *Power deposited per unit length in the collimators COLL1, COLL2, COLL3 and COLL6 as a function of the vertical bunch displacement for the TESLA capture system.*

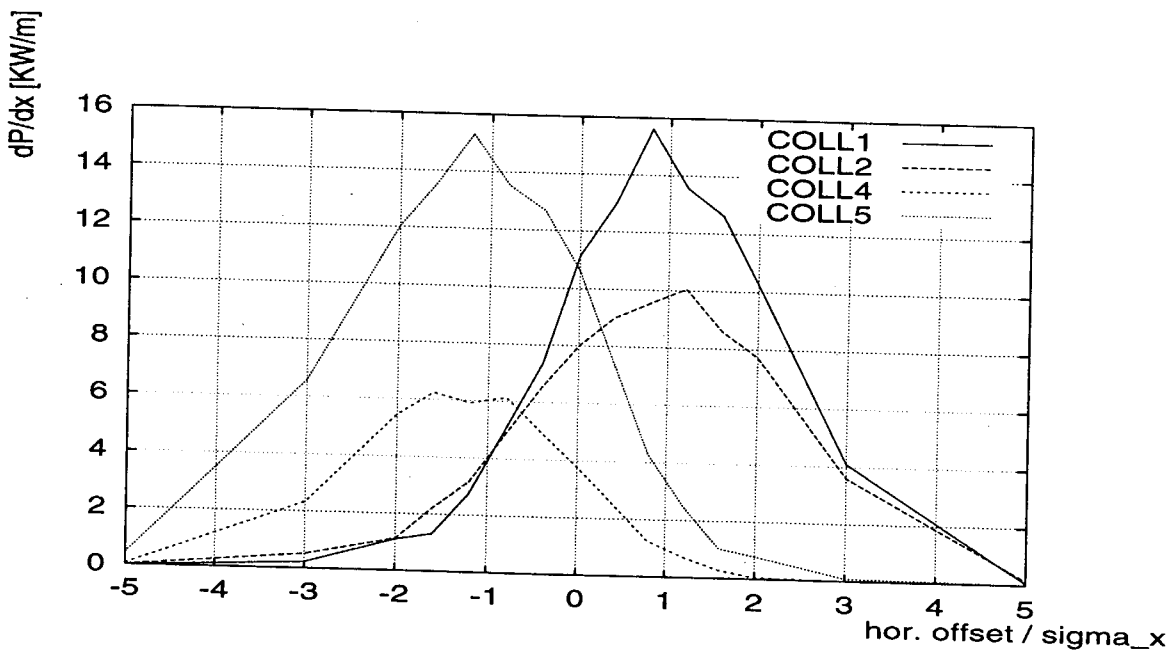

Figure 9.8: *Power deposited per unit length in the collimators COLL1, COLL2, COLL4 and COLL5 as a function of the horizontal bunch displacement for the TESLA capture system.*

Chapter 10

Potential upgrade for a polarized positron source for TESLA

As described in section (2.2), the emittance requirements for the polarized positron source based on a helical undulator of about 100 m length are much stronger than for an unpolarized source. The electrons of the spent beam have to produce circularly polarized photons which are converted into polarized positrons inside the target. Only on-axis photons are completely circularly polarized. The photon spot size on the target must be dominated by the natural spot size of the undulator radiation. The higher harmonics of the undulator radiation must be scraped between the end of the undulator and the target. The emittances must be reduced to $5 \cdot 10^{-4}$ mm mrad in both the horizontal and the vertical planes. The distance between the end of the undulator and the target must be increased to $\approx$ 150 m to provide sufficient space for photon collimation. A solution has been found which provides the required properties for an almost sufficient fraction of the spent beam for TESLA, under design conditions at the IP.

The results from the capture system for the unpolarized source were performed to realize a spent beam capture system for the polarized positron source. As can be seen in fig.(8.18), the vertical emittance requirement is fulfilled for a fraction of roughly 80 % of the beam although the chromaticity is not corrected in the vertical plane. At the end of the chromaticity correction section, the horizontal emittance is $\approx 4.5 \cdot 10^{-4}$ mm mrad for roughly 60 % of the spent beam. These results were obtained for an achromatic section which was optimized for a broad energy bandwidth, considering particles with an energy deviation of $|\Delta E/E| < 0.07$. The optical functions after the IP were matched to this large energy bandwidth of the beam. As shown in fig.(8.17), a spent beam fraction of $\approx$ 60 % corresponds to an energy cut of roughly $|\Delta E/E| < 0.025$. Attempts were made to improve the efficiency of the chromaticity correction section. The initial conditions at the beginning of the capture system were matched to this smaller energy bandwidth of the spent beam. The idea was to increase the capture efficiency with regard to the small emittance requirements by decreasing the band width of the achromatic section. However, it was not possible to improve the capture efficiency with respect to the requirements for the polarized source. As shown in fig.(8.18), the emittance of spent beam fractions of less than roughly 65 % (corresponding to an energy deviation of less than 3 %) is almost constant. Thus, the emittance in the flat region of fig.(8.19) is actually not dominated by linear chromatic effects but by quantum excitation, nonlinear effects and remaining uncompensated geometric aberrations. Therefore the emittance requirements can only be fulfilled by stronger collimation. Shown in fig.(10.1) is the horizontal emittance along the capture system without collimators. The data set used in the tracking simulations contained particles with an energy loss of not

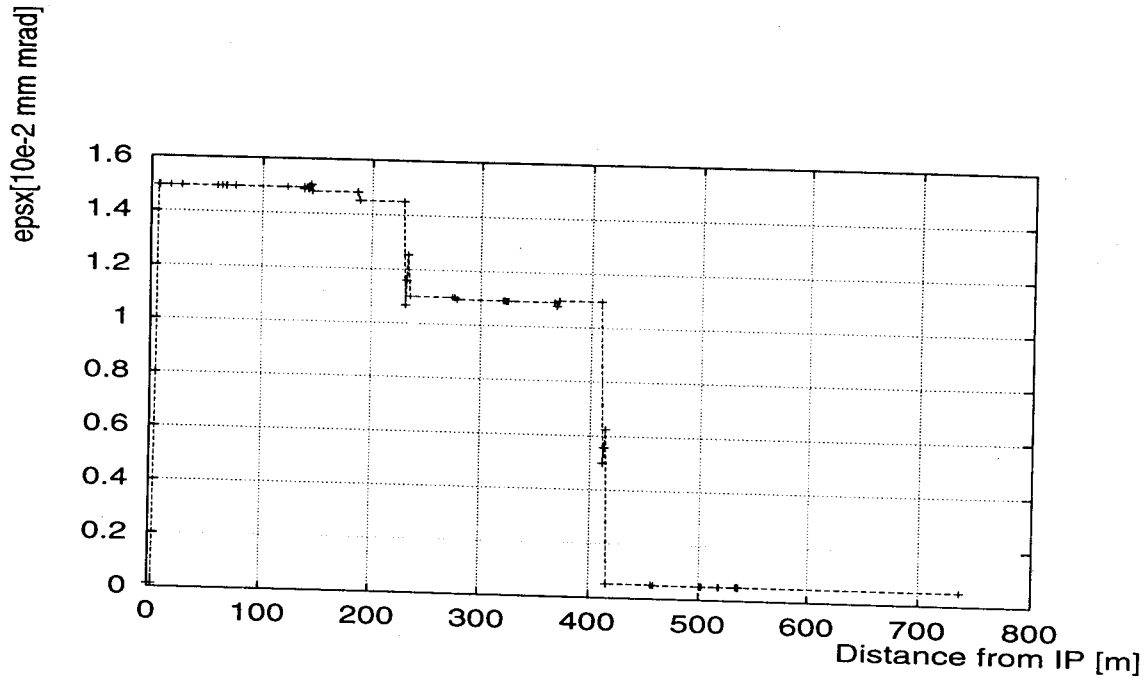

Figure 10.1: *Horizontal emittance along the spent beam capture system and the helical undulator without collimators. The tracking was done using the fraction of the beam with an energy loss of less than 2.5 %. At the beginning of the undulator, the horizontal emittance for* ≈ 60 *% is reduced to* $4.4 \cdot 10^{-10}$ *radm for this data set.*

more than 2.5 %.

The optical elements inside the matching section and the chromaticity correction section are the same as those for the unpolarized source. A strong separation at the end of the capture system is required for the target and the following optics. The separation can be increased by changing the sign of the bending strengths inside the collimation section of the oncoming beam delivery system. This can be done without complications if the signs of the sextupole strengths are also changed. The capture system including the undulator and the separation section is shown in fig.(10.2) together with the modified beam delivery system developed by O.Napoly [Nap94].

The collimators were positioned in a way as explained for the unpolarized positron source. At the end of the chromaticity correction section the only particles which remain are those with an energy deviation not less than 2.62 %. The emittances are $4.89 \cdot 10^{-4}$ mm mrad horizontally and $1.01 \cdot 10^{-4}$ mm mrad vertically for this remaining fraction of 62 % of the spent beam. At a distance of 15 m downstream of the chromaticity correction section, the optics is continued with a quadrupole triplet. The collimator positions and the collimated beam power are shown in tab.(10.1)

The capture efficiency of the spent beam capture system is roughly 8 % less than that required in the calculations of K.Floettmann [Flt93]. The spent beam fraction of 70% is required for a safety factor of 2, i.e. that one electron produces two positrons. Thus, with reduced margin of safety it is possible to realize the polarized source.

The serious problem with such a low capture efficiency is the effects of perturbed interactions at the IP. In the case of a missing interaction, the bunch charge will oscillates with a much larger amplitude (with deviations up to 60 % of the design charge) and with a longer damping time. In the case of a collective deflection of the beam, an intolerable power deposition inside the collimation regions is to be expected. Even under design interactions, the power deposited inside the second collimator after the IP is approximately 2.4 MW, or 50.1 kW/m. It is to be expected, that the limits of the collimators are reached already for a small displacements of the

bunches at the IP.

To avoid these problems, the beam size at the IP could be increased in order to reduce the beamstrahlung. The efficiency of the capture system is determined mainly by the bandwidth of the chromaticity correction section. Thus, an increase of the population with a low energy loss, see fig.(7.4), would cause a higher fraction of the initial beam which could be transported through the helical undulator. Since the broad energy distribution behind the IP is caused by beamstrahlung i.e. the strength of the deflection and oscillation of the particles during the bunch crossing, it is straightforward to increase beam size at the IP. This can be done by increasing the horizontal β-function. The luminosity is given by

$$\mathcal{L} = \frac{P_b \cdot N}{4\pi E\, \sigma_x^* \sigma_y^*}, \tag{10.1}$$

where σ_x^* and σ_y^* denote the horizontal and vertical rms beam size at the IP, P_b the beam power, E the beam energy and N the number of bunches per pulse. A beam-beam-simulation has been performed for different horizontal β-functions. The particle ensembles have been tracked through the same capture optics as for the design parameters. The result of an increased horizontal beam size at the IP is a higher fraction of the spent beam inside the energy acceptance of the capture system. Shown in fig.(10.3) is the transfer efficiency of the spent beam capture system as a function of the horizontal β-function at the IP. The efficiency rises to 89 % for a horizontal β-function of four times the design value. This corresponds to a luminosity loss by a factor of two which is quite a lot. However, the required spent beam fraction [Flt93] of 70 % can be captured for a horizontal β-function of 37 mm, i.e. a factor of roughly 1.5 than the design value. This would lead to a luminosity loss of 18 %.

It can be concluded, that the polarized source using a helical undulator is feasible if the beam size at the IP could be increased. However, the disadvantage of a luminosity loss in order to get circularly polarized positrons has to be discussed with respect to the luminosity requirements of the experiments. Furthermore it has to be ensured that no particles hit the superconducting device, even under worse conditions. Therefore the effects of non-design interactions, discussed in chapter (9.2) have to be investigated very carefully. In addition, deviations of the element strengths, caused for example by fluctuations in the power supply of the optical elements, must be studied.

Collimator	Position behind IP [m]	Collimated beam power [kW]
C1	27.51-59.51	679.23
C2	75.51-122.12	2375.44
C3	235.89-274.14	30.22
C4	415.89-456.39	27.47
C5	536.19-541.19	0.69

Table 10.1:
Collimator positions and collimated beam power for the polarized positron source for TESLA. The total power to be collimated along the capture system is 3.11 MW.

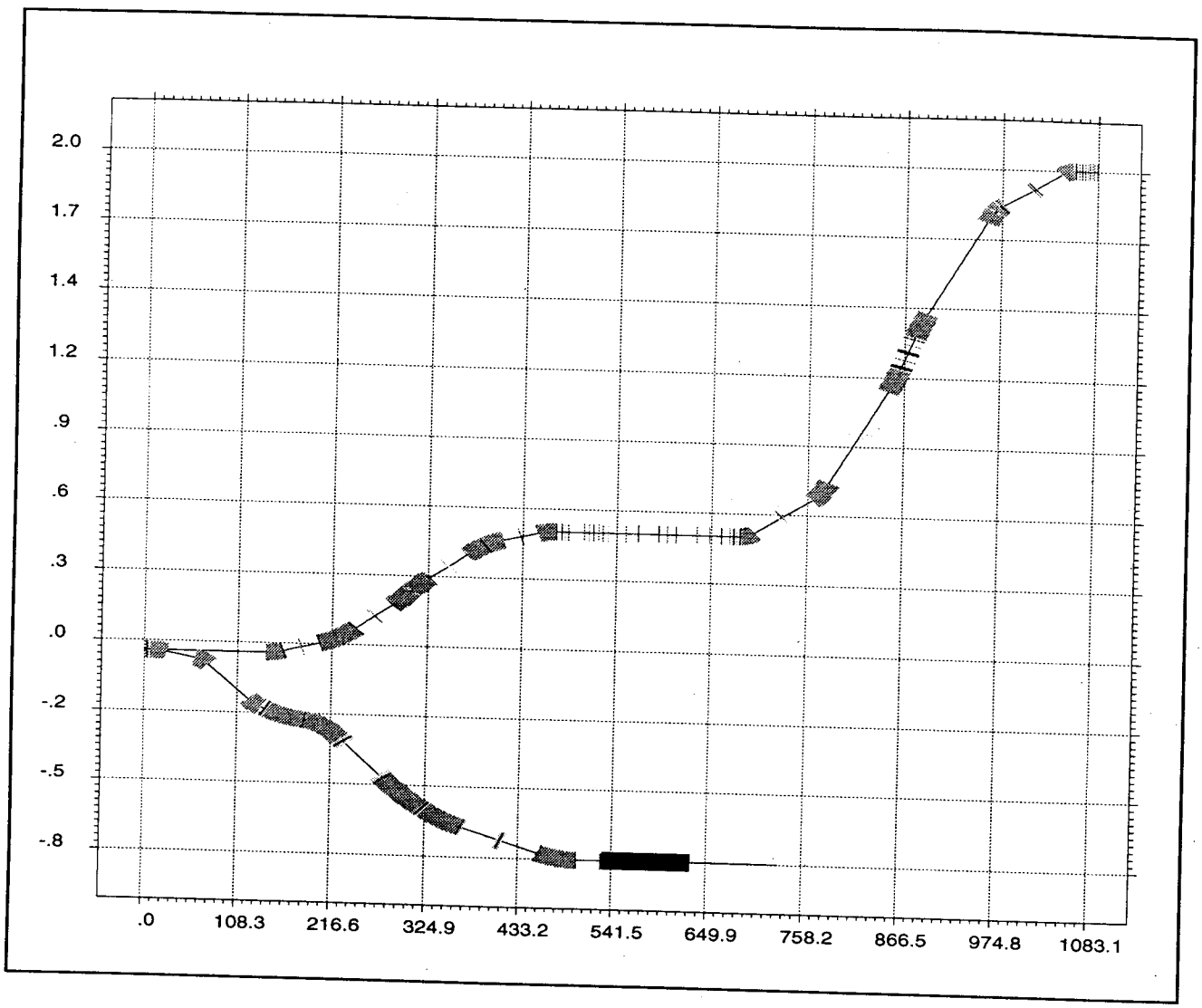

Figure 10.2: *Spent beam capture system for TESLA continued with the 100 m long helical undulator (lower branch), and the oncoming positron beam (upper branch).*

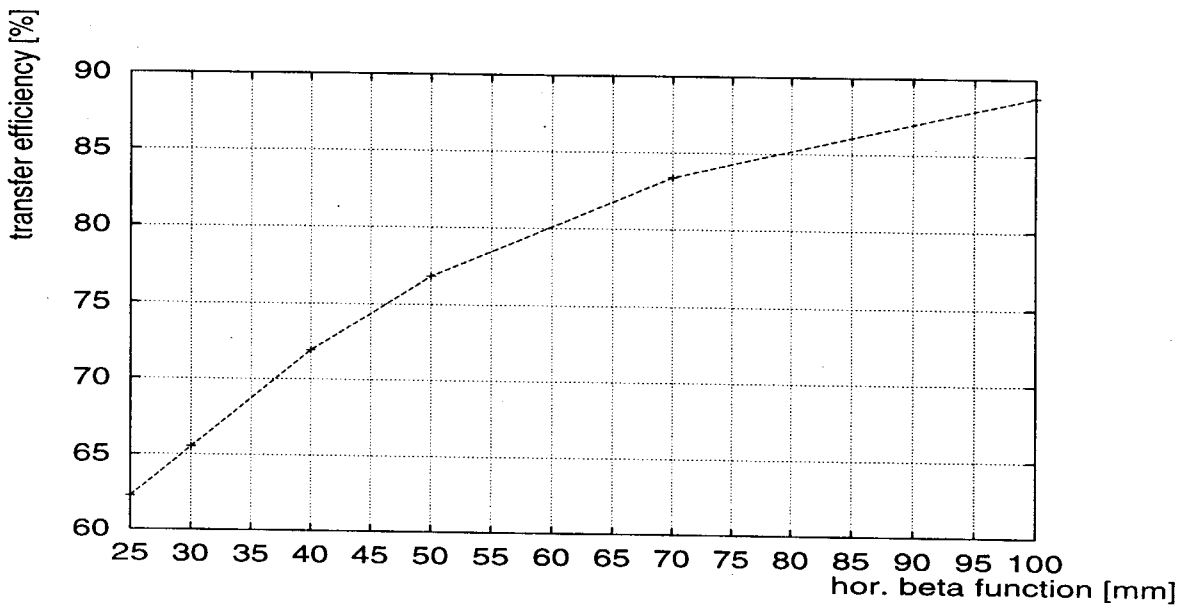

Figure 10.3: *Capture efficiency as a function of the horizontal β-function at the IP for polarized positron source for TESLA. Starting from the design value of 25mm the capture efficiency reaches 70% of the disrupted beam at $\beta_x = 37$ mm. With this value of β_x, 20 %of the design luminosity is lost.*

Chapter 11

Conclusions

In the present thesis, the feasibility of high intensity positron sources for the SBLC and TESLA was studied. The beam current for these linear colliders is up to two orders of magnitude higher than existing ones. Therefore a positron source based on conventional technology would be very difficult to realize. A different concept of positron production was invented by V.E. Balakin and A.A. Mikhailichenko [Bal79]. The positrons are produced by a photon beam which is converted into electron-positrons pairs in a suitable target. The photon beam is generated using an electron beam passing through a wiggler or undulator. Based on this principle, a high intensity, unpolarized and polarized positron source for linear colliders was developed by K.Floettmann [Flt93]. The requirements on the beam properties for the polarized positron source realized by 100 m long helical undulator are much tighter than for the unpolarized wiggler-based source.

In order to reduce the installation and operational costs, the positron sources should be preferably operated using the spent electron beam for the photon production. Therefore the main part of the present work treats the development of a beam optical transport system from the interaction point to the beginning of the wiggler or undulator. It has been found, that the unpolarized source can be operated using the spent beam for the SBLC and for TESLA. For the SBLC, it is possible to use 87 % of the original spent beam for photon production. In the TESLA case, the requirements are fulfilled for 85 % of the spent beam. Thus, the efficiency of the spent beam capture system is considerably higher than the 70 % assumed by[Flt93] (which includes a safety factor of 2). Since not the whole beam can be used for positron production, the unwanted fraction of the spent beam must be scraped off along the capture system. The collimators are distributed along the drift spaces of the capture system in order to reduce the heat load. The highest amount of deposited power per unit length under design interactions was found to be 14.3 kW/m which is in reasonable limits of state-of-the-art vacuum systems.

The results of both capture systems mentioned above are only valid under design interactions. Therefore the consequences of perturbed interactions of the bunches have been investigated. In the case of a missing interaction, charge oscillations of the positron bunches are to expect as a result of the different energy spreads after the following interactions and as a consequence of the fixed collimator positions. Numerical analyses have shown, that the bunch charge oscillations after one missing interaction are not critical.

A more severe problem is caused by transverse beam-beam offsets at the interaction point. The electron bunches suffer an average deflection due to the electromagnetic field of the oncoming positron bunches. However, the collimator positions are fixed for the design interaction. Hence a much higher power deposition occurs in the case of a coherent deflection of the spent

electron beam. It has been shown in numerical simulations that a horizontal beam offset is uncritical for both linear colliders. The highest power deposition per unit length were found to be roughly 25 kW/m for the SBLC and 15 kW/m for TESLA. The main problem is beam-beam offset in the vertical plane. This leads to a maximum power deposition up to 60 kW/m for the SBLC. In the TESLA case, the maximum deposited power inside the last collimator before the wiggler actually rises up to 300 kW/m which is not tolerable. However, the collimator positions are not yet optimized with regard to deviations from the design interaction. In the present design of the spent beam capture systems, the collimation systems concerns mainly the horizontal plane.

By increasing the over-all length of the collimator sections and paying more attention to vertical losses of the beam, it should be possible to solve this problem in a future, more sophisticated design.

Concerning the polarized positron source, it has been shown that the emittance requirements cannot be fulfilled for the present SBLC design. Even the emittance growth by quantum excitation caused by the synchrotron radiation in the off-axis fields of the final focus quadrupoles is not acceptable. Additional problems are nonlinear chromatic effects together with the geometric aberrations which cannot be corrected in the following capture optics.

A way out could be a different design of the first final focus quadrupole behind the interaction. The multipole components in the spent beam position beyond the pole tips (as seen from the longitudinal symmetry axis) are responsible for the deterioration of the beam quality. These multipole components depend strongly on the shape of the magnet. Thus, an optimization of the quadrupole design could reduce the negative effect on the spent beam.

A better solution would be an increase of the crossing angle such that the spent beam does not have to pass through the final focus quadrupoles. Then the beam would not be affected by higher order magnetic multipoles fields. Furthermore it could be focused after a short distance behind the interaction point and the situation would be comparable to that of TESLA. However, such a crossing angle would increase the difficulties for the crab crossing.

In the case of TESLA, a solution was found for operating the polarized positron source using ≈ 62 % of the spent beam. For this fraction (reducing the safety factor in the positron production from 2 to 1.8) the very tight emittance requirements could be fulfilled under design conditions at the IP.

The comparably low efficiency of the spent beam capture system increases the problems due to perturbations at the interaction point. This would lead to huge bunch charge oscillations after a missing interaction which would still be damped but with higher amplitudes and with a much longer damping time. Also the problems of transverse beam-beam offsets would be more serious than even for the unpolarized source.

In order to reduce the problem of instabilities and the resulting heat load inside the collimator system and to find a reliable solution for the polarized source, the consequences of an operation before the IP have been investigated.

After passing the wiggler or undulator, the electron beam has lost energy due to the emitted photons. Therefore the operating energy of the linac has to be higher to provide the required energy at the IP. It has been found for the wiggler-based positron source, that the electron energy at the entry of the wiggler has to be 3.3 % higher than the design energy of 250 GeV. For the polarized source, the energy would have to be 2.6 % higher.

The most serious problem, however, is the energy spread induced by the wiggler or undula-

tor. In the TESLA case, the unpolarized positron source before the IP would cause an energy spread 7 times higher than designed. The weaker helical undulator would increase the energy spread by a factor of 5. Thus, one of the main advantages of TESLA, the very small energy spread, is lost.

In the SBLC case the situation is worse. The crossing angle at the IP requires the crab crossing scheme to work. An energy spread correlated to the longitudinal particle position inside the bunch is needed. This correlation is reduced inside the wiggler or undulator. Assuming the present crossing angle of 6 mrad, the luminosity would be reduced by a factor of 2.9 for the unpolarized source and by a factor of 2.3 for the polarized source. A way out could be a rf-crab crossing (the bunches are rotated by a cavity working in a deflecting mode).

Furthermore, the effects of manufacturing tolerances were analyzed concerning the unpolarized source. In could be shown, that variations in the length and strength of the magnetic poles within reasonable limits have only a negligible effect on the beam emittance.

Since an operation of the linac at lower energies is important for the commissioning, the minimum possible electron energy which can be used to drive a wiggler-based positron source was estimated. It has been found that a reasonable lower limit for the operating energy of the collider with a full positron intensity is given by an electron beam energy of 100 GeV.

For the polarized source it is not only important to ensure a safe passage of the beam through the undulator. Due to the emission characteristics of the undulator radiation, a fraction of the radiated power is deposited inside the magnet aperture. For a beam energy of 250 GeV with the present undulator strength and period length, the power deposition inside the undulator does not seem to be critical. In the case of a very small beam diameter (i.e. the polarized source is operated before the IP) the total deposited power for a 150 m long undulator is in the order of 22 W with a maximum power density of roughly 0.75 W/m. In the case of operating the polarized source using the spent beam, the power deposition is higher. The power deposition for a transverse rms-beam size of 0.5 mm would be four times higher than for a beam with a negligible beam diameter, which still seems to be tolerable even for a superconducting undulator. For a low energy operation of the polarized source, the power deposition would be more serious because it is dominated by the opening angle of the radiation which is increasing with decreasing energy.

It is concluded that the unpolarized wiggler-based positron source can be operated by the spent electron beam.

For TESLA, a solution was found to realize the undulator based polarized source under design conditions at the IP. However, a reliable operation using the spent beam needs further investigations. Concerning the operation before the IP, the advantage of providing polarized positrons versus the drawback of an increased energy spread has to be discussed between the users.

With the present design of the SBLC, a realization of the polarized positron source is not possible. A way out could be an operation before the IP with an rf-crab crossing.

Acknoledgements

I want to thank my supervisor Dr.J.Rossbach for the possibility to work on this interesting field and for his continuous encouragement.

Furthermore I am deeply indebted to Dr.R.Brinkmann and Dr.K.Flöttmann for the many helpfull discussions and for their numerous suggestions.

I would like to thank Prof.Dr.P.Schmüser for being the second examiner and for his lots of advice concerning the design of this thesis.

I am also indebted to Mrs.S.Wipf, Dr.D.Kelly, Dr.T.Limberg,Dr.M.Lomperski and Dr.N.Walker for carefully correcting the manuscript.

Last not least I want to thank my family for their support and my girl friend for her patience.

Appendix A

Energy deposition by a single electron inside a helical undulator

It is to expect that the beam parameters will change in the future, particularly since also an operation of the polarized source at energies lower than 250 GeV is interesting. In section (3.3) the power deposition inside a helical undulator is calculated using the present TESLA parameters for the design energy of 250 GeV. In this chapter, the deposited energy per unit length and the total energy deposition is plotted for one single electron passing through a helical undulator. Each picture shows the energy deposition in MeV and MeV/m for electron energies of E_{e^-}=100,150,200 and 250 GeV,respectively. From this, the power deposition per unit length dP/dx in W/m and the total power deposition P_{tot} in W inside the undulator can easily be obtained by multiplying the dE/dx (in MeV/m) and the energy deposition E_{tot} (in MeV) with the factor

$$\xi = 1.602 \cdot 10^{-13} \left[\frac{J}{MeV}\right] N_p N_b f_{rep}. \tag{A.1}$$

Here N_p is the number of particles per bunch, N_b the number of bunches per pulse and f_{rep} the linac repetition frequency. All calculations were done with the same undulator strength B_0=0.9 T changing the undulator period length λ_u to get results for different undulator parameters of K (K = 0.5, 0.75, 1.0 and 2.0). As explained in chapter (3.3), the results have to be scaled with the factor $(B/B_0)^2$ for a different undulator field B, keeping the undulator parameter K fixed.

At the first sight, the results shown in fig.(A.1) to fig.(A.8) are amazing because the energy deposition caused by low energy electrons is systematically higher than the deposition by the high energy electrons although the total radiated power is proportional to γ^2 (eq.(3.24)). The reason for this is the increase of the opening angle with decreasing particle energy ($\theta \propto 1/\gamma$). Then the ratio of the opening angle of the radiation to the opening angle of the undulator $KL/r\gamma$ approaches one. The energy deposition from the tail of the angular distribution of the radiated power shown in fig.(3.2) growth stronger than the total radiated energy proportional γ^2.

If the undulator would be extended while keeping all other parameters constant, the increase of the energy deposition per unit length inclines until up to a maximum. At least from this point on, the total depositioned energy is indeed $\propto \gamma^2$ but an undulator with this properties is not reasonable at all.

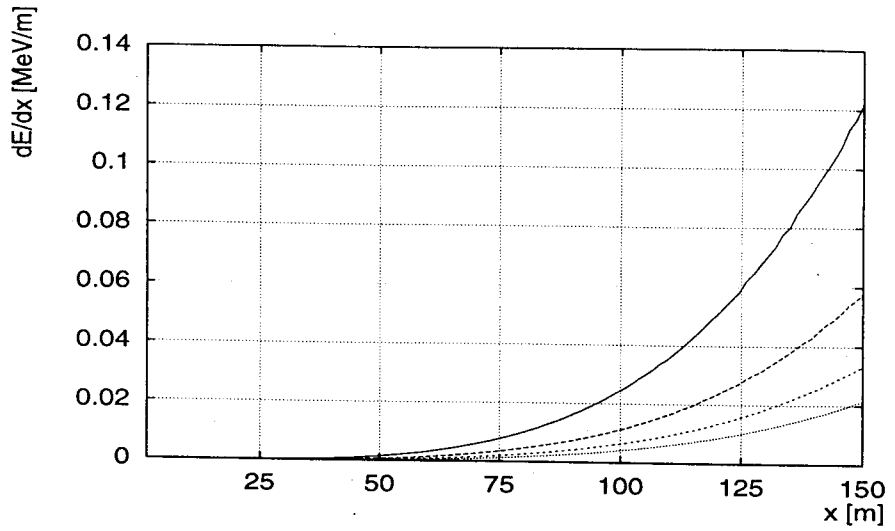

Figure A.1: *Energy per unit length deposited by a single relativistic electron inside a helical undulator with K=0.5 (B=0.9 T, λ_u=6 mm) for a fixed inner radius of 2.5 mm. The electron energy is E_{e^-}=100,150,200,250 GeV from the highest to the lowest curve.*

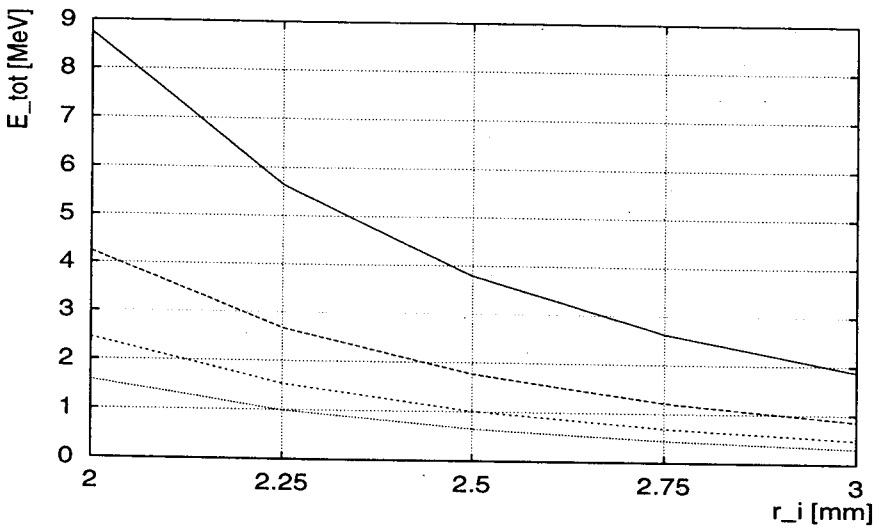

Figure A.2: *Total deposited energy by one single relativistic electron inside a helical undulator with K=0.5 (B=0.9 T, λ_u=6 mm) as a function of the inner radius. The electron energy is E_{e^-}=100,150,200,250 GeV from the highest to the lowest curve.*

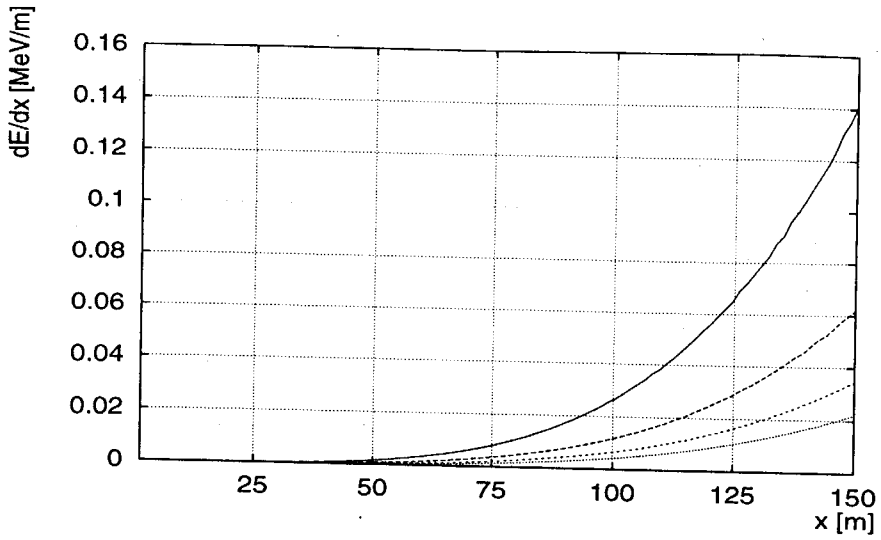

Figure A.3: *Energy per unit length deposited by a single relativistic electron inside a helical undulator with K=0.75 (B=0.9 T, λ_u=9 mm) for a fixed inner radius of 2.5 mm. The electron energy is E_{e^-}=100,150,200,250 GeV from the highest to the lowest curve.*

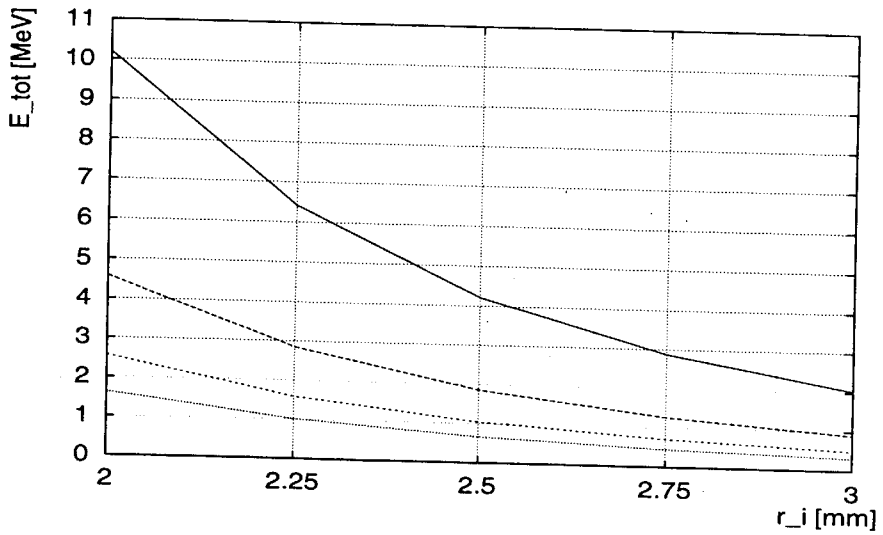

Figure A.4: *Total deposited energy by one single relativistic electron inside a helical undulator with K=0.75 (B=0.9 T, λ_u=9 mm) as a function of the inner radius. The electron energy is E_{e^-}=100,150,200,250 GeV from the highest to the lowest curve.*

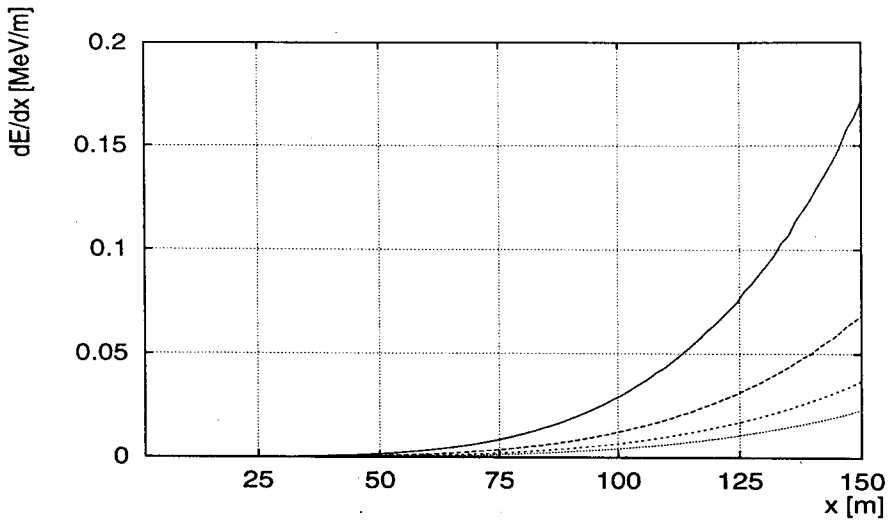

Figure A.5: *Energy per unit length deposited by a single relativistic electron inside a helical undulator with K=1.0 (B=0.9 T, λ_u=12 mm) for a fixed inner radius of 2.5 mm. The electron energy is E_{e^-}=100,150,200,250 GeV from the highest to the lowest curve.*

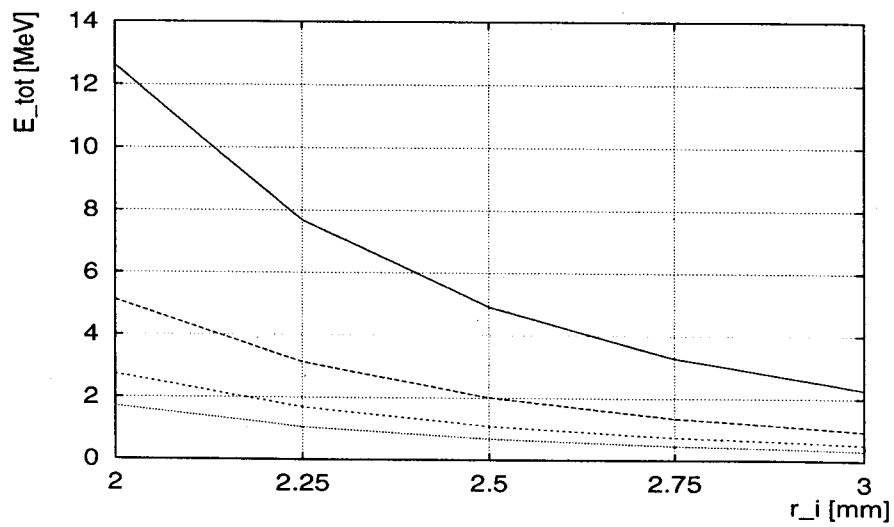

Figure A.6: *Total deposited energy by one single relativistic electron inside a helical undulator with K=1.0 (B=0.9 T, λ_u=12 mm) as a function of the inner radius. The electron energy is E_{e^-}=100,150,200,250 GeV from the highest to the lowest curve.*

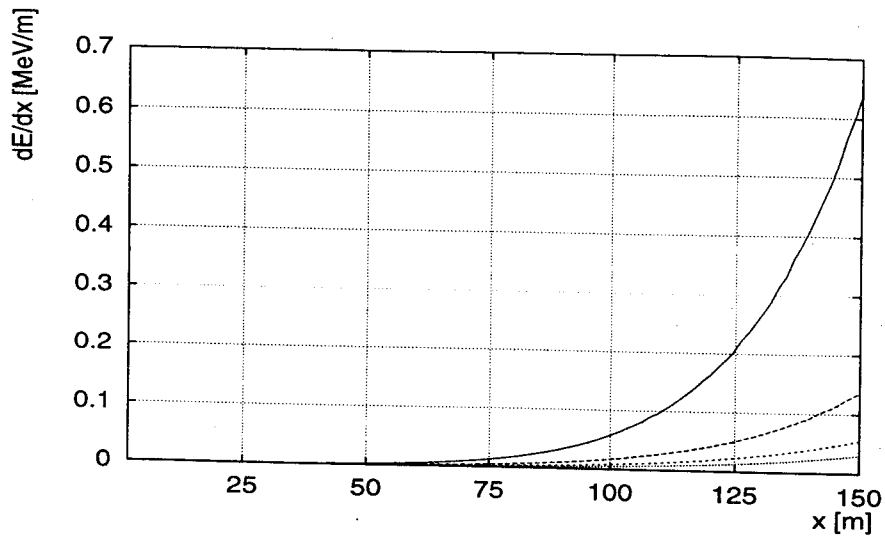

Figure A.7: *Energy per unit length deposited by a single relativistic electron inside a helical undulator with K=2.0 (B=0.9 T, λ_u=24 mm) for a fixed inner radius of 2.5 mm. The electron energy is E_{e^-}=100,150,200,250 GeV from the highest to the lowest curve.*

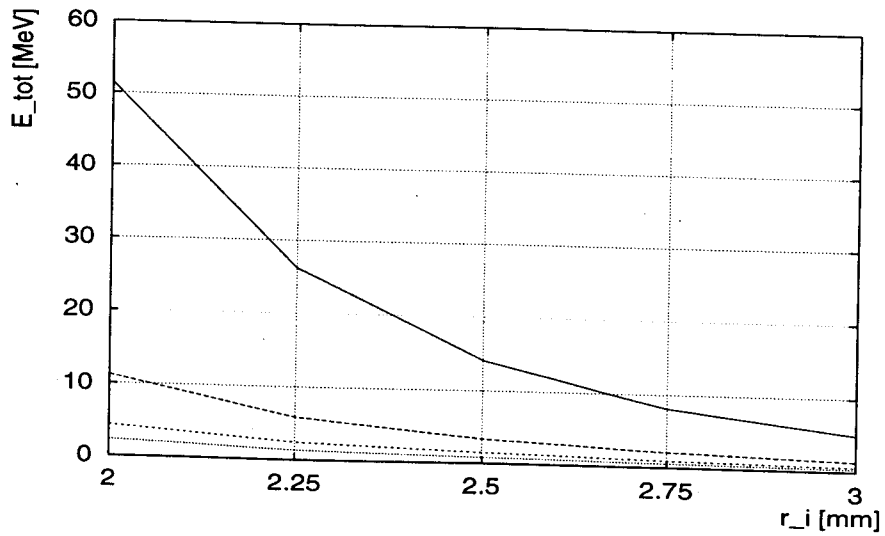

Figure A.8: *Total deposited energy by one single relativistic electron inside a helical undulator with K=2.0 (B=0.9 T, λ_u=24 mm) as a function of the inner radius. The electron energy is E_{e^-}=100,150,200,250 GeV from the highest to the lowest curve.*

Appendix B

A statistical expression for emittances and optical functions

In the present work the beam emittance is one of the most important parameters to estimate whether the positron source can be operated or not. Together with the optical functions it is related to the beam diameter and its propagation along the wiggler or undulator whose aperture limits (together with the special demands on the polarized source) lead to the emittance requirements quoted in [Flt93]. The optical functions are well defined by the periodic solution a circular machine but there is a freedom to choose the Twiss parameters for a beam passing a transport line. In this case the condition of periodicity does not exist and the optical functions which parameterizes the orientation and the size of the phase space ellipsoid is undefined but can be chosen in reasonable way [Ros92]. Once the Twiss parameters are fixed for an initial particle ensemble, the phase space ellipsoid is transported through the transport line by the usual matrix formalism. If the Twiss parameters do not describe the correct phase space distribution, the beam transport through the optical elements could lead to an emittance increase due to filamentation.

The optical functions and emittances have to be estimated from of the particle data which used in all the numerical simulations. The second order moments of the phase space distributions have been calculated after the linear dispersion was subtracted. The emittance has been estimated according to [Lap71] and [Buo94].

The main axis of the phase space distributions are aligned such that the sum of the square distances of all particles to these axes are minimized. This leads to an angle between the axes of the coordinate system (x, x') and the main axes of the phase space ellipsoid (X, X') of

$$\theta = \frac{1}{2}\arctan\left(\frac{2\,\overline{xx'}}{\overline{x^2} - \overline{x'^2}}\right) \tag{B.1}$$

with

$$\overline{xx'} = \frac{1}{N}\sum_{i=1}^{N}(x_i - \overline{x})(x_i' - \overline{x'}), \quad \overline{x^2} = \frac{1}{N}\sum_{i=1}^{N}(x_i - \overline{x})^2, \quad \overline{x'^2} = \frac{1}{N}\sum_{i=1}^{N}(x_i' - \overline{x'})^2, \tag{B.2}$$

With regard to the ellipsoid axes, the standard deviations are

$$\sigma_{X,X'} = \frac{1}{2}\left(\overline{x^2} + \overline{x'^2} \pm \frac{2\overline{xx'}}{\sin 2\theta}\right) \tag{B.3}$$

The definition of the emittance as the elliptical area of the phase space distribution $\varepsilon_x = \sigma_X \sigma_{X'}$ leads to

$$\varepsilon_x = \sqrt{\overline{x^2} + \overline{x'^2} - \overline{xx'}^2} \tag{B.4}$$

Out of the relation $\overline{x^2} = \sqrt{\beta_x \varepsilon_x}$ and $\overline{x'^2} = \sqrt{\gamma_x \varepsilon_x}$ one gets

$$\beta_x = \frac{\overline{x^2}}{\sqrt{\overline{x^2} + \overline{x'^2} - \overline{xx'}^2}} \tag{B.5}$$

and

$$\gamma_x = \frac{\overline{x'^2}}{\sqrt{\overline{x^2} + \overline{x'^2} - \overline{xx'}^2}} \tag{B.6}$$

Since $\gamma_x = (1 + \alpha_x^2)/\beta_x$ one gets

$$\alpha_x = -\frac{2 \cdot \overline{xx'^2}}{\sqrt{\overline{x^2} + \overline{x'^2} - \overline{xx'}^2}} \tag{B.7}$$

The emittance and the optical functions out of the second order moments obtained from eq.B.2 are estimated correctly only in case of absence of dispersion.

In dispersive regions one has to calculate first the relation between the energy deviation and the phase space coordinates of the particles. The contribution of the dispersion has to be subtracted what means that if $(\widetilde{x_i}, \widetilde{x_i'})$ are the original phase space coordinates, the second order moments have to be computed using

$$x_i = \widetilde{x_i} - D \cdot \frac{\Delta p_i}{p}, \quad x'_i = \widetilde{x_i}' - D' \cdot \frac{\Delta p_i}{p} \tag{B.8}$$

where D and D' is the linear dispersion and its slope which have been estimated out of the particle ensemble by a linear regression [Brn80] in the $\widetilde{x}\frac{\Delta p}{p}$ and the $\widetilde{x'}\frac{\Delta p}{p}$ distribution according to

$$D = \frac{\sum_{i=1}^{N} (\widetilde{x_i} - \overline{\widetilde{x}})(\frac{\Delta p_i}{p} - \overline{\frac{\Delta p}{p}}),}{\sum_{i=1}^{N} (\frac{\Delta p_i}{p} - \overline{\frac{\Delta p}{p}})^2} \tag{B.9}$$

and

$$D' = \frac{\sum_{i=1}^{N} (\widetilde{x_i}' - \overline{\widetilde{x'}})(\frac{\Delta p_i}{p} - \overline{\frac{\Delta p}{p}}),}{\sum_{i=1}^{N} (\frac{\Delta p_i}{p} - \overline{\frac{\Delta p}{p}})^2} \tag{B.10}$$

All these calculations have been done in the same way for the vertical plane.

Appendix C

Phase space distributions and collimator-cuts for the SBLC spent beam capture system

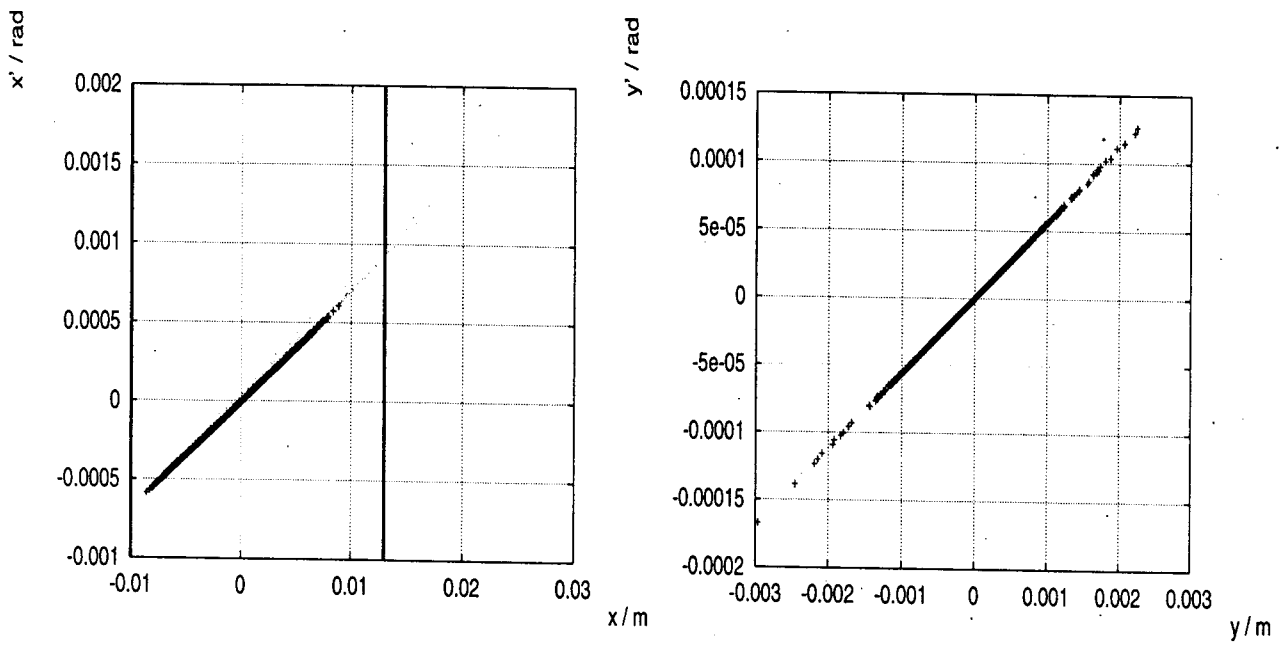

Figure C.1:
Left: Horizontal phase space at the end of the first collimator region at the beginning of the first half-quadrupole 10 m behind the last final focus quadrupole. Right: Vertical phase space in the same position.

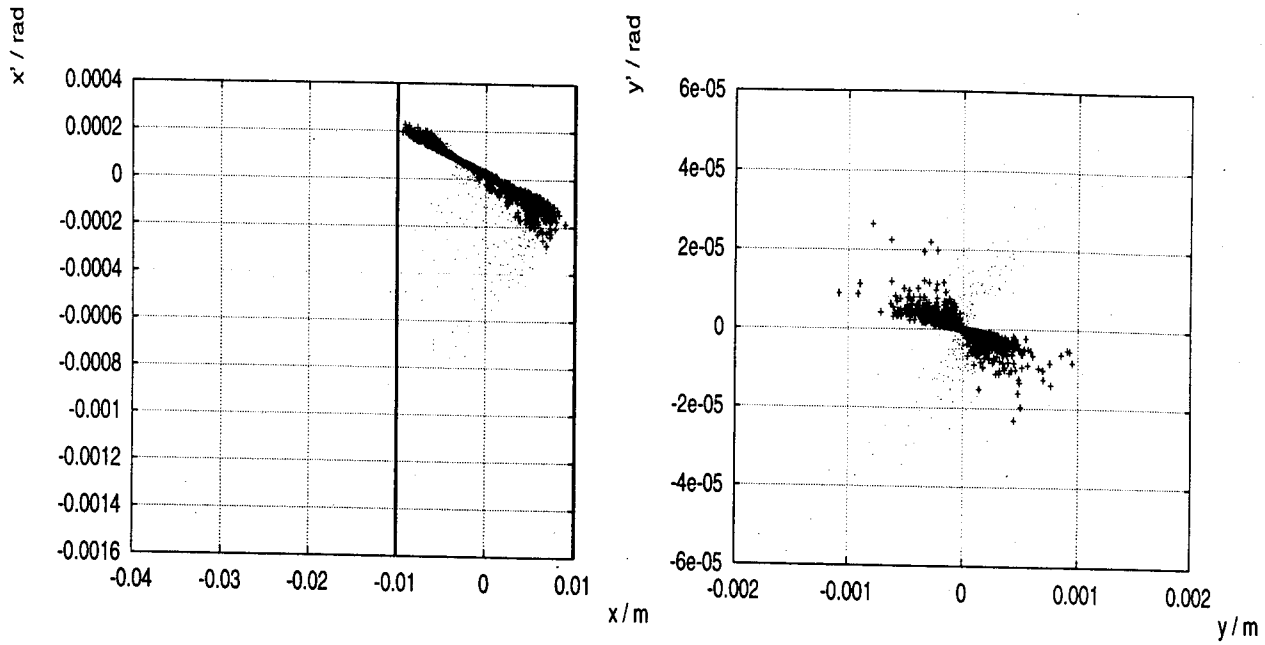

Figure C.2:
Left: Horizontal phase space at the end of the first collimator region between 38.23 and 58.23 m behind the last final focus quadrupole. Right: Vertical phase space in the same position.

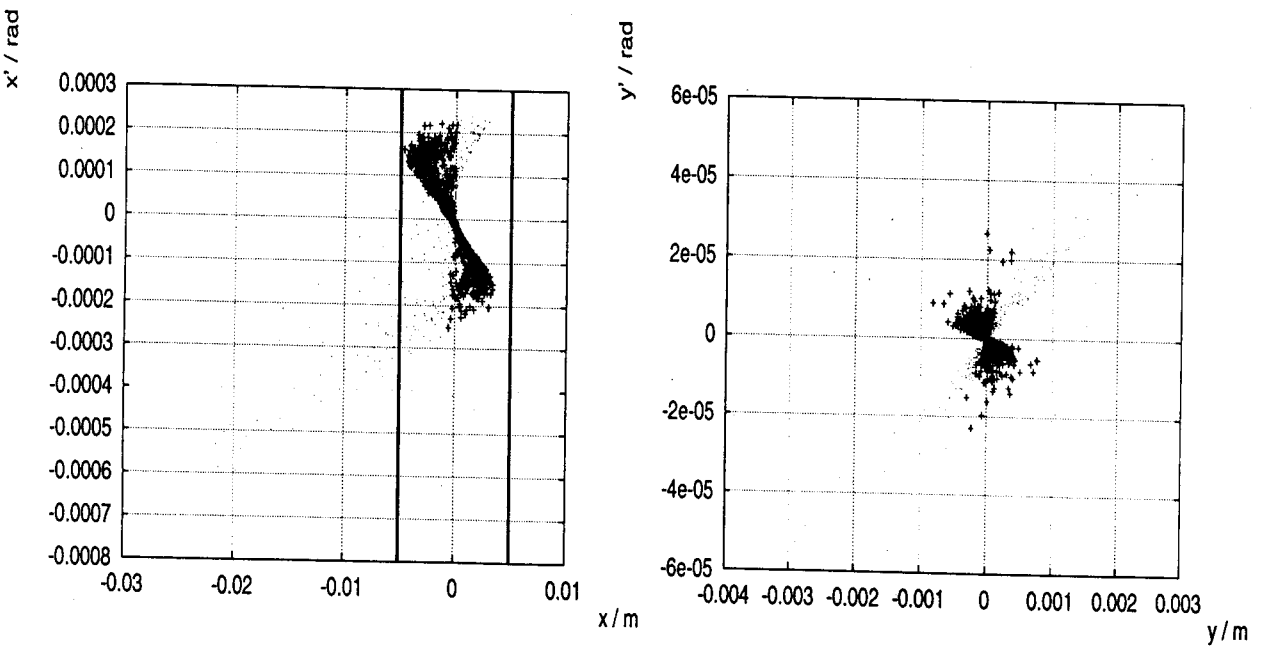

Figure C.3:
Left: Horizontal phase space at the end of the third collimator region in a distance of 87.4 m behind the last final focus quadrupole. Right: Vertical phase space in the same position.

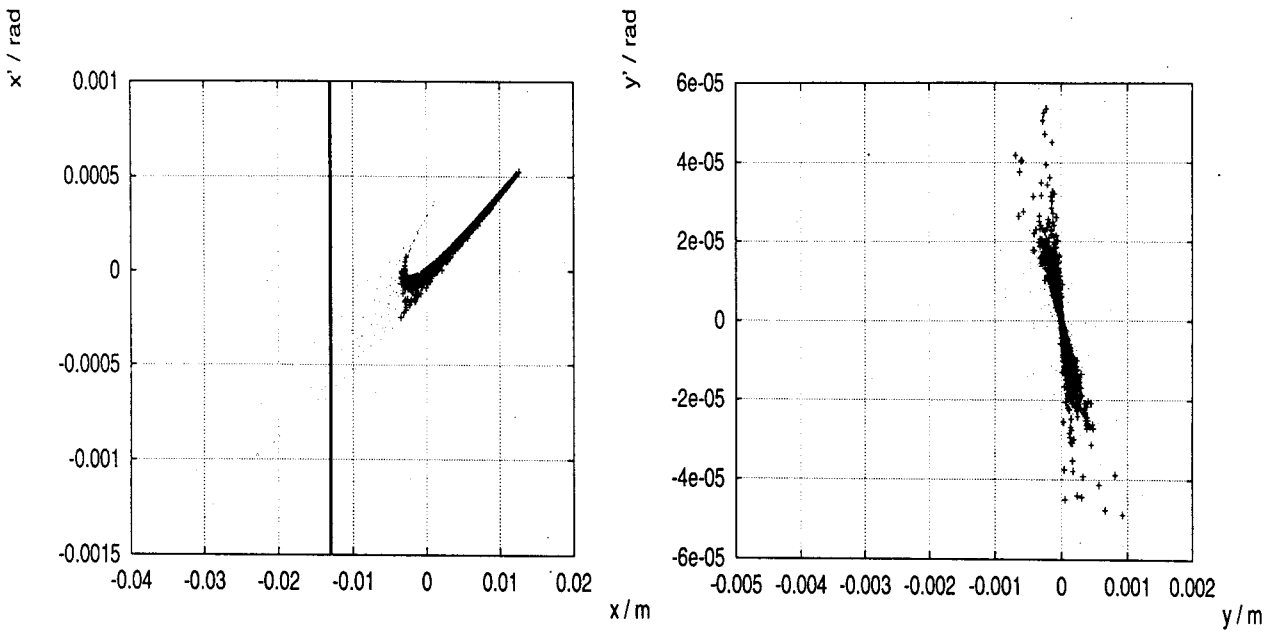

Figure C.4:
Left: Horizontal phase space at the end of the fourth collimator region 154.9 m behind the last final focus quadrupole. Right: Vertical phase space in the same position.

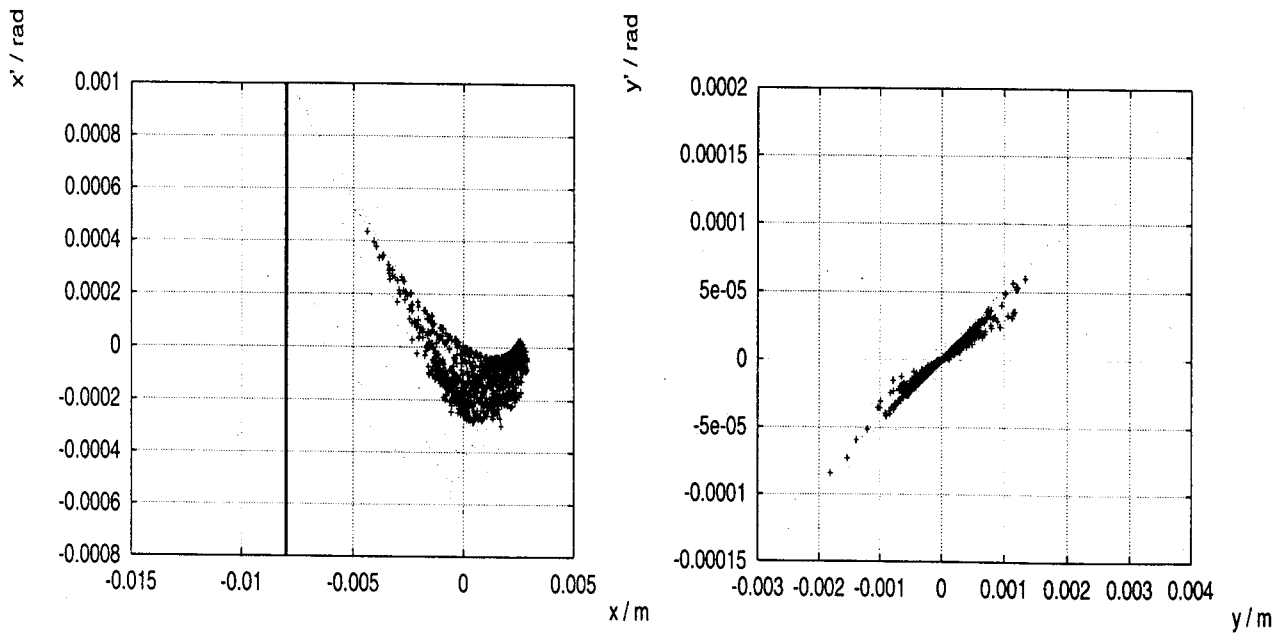

Figure C.5:
Left: Horizontal phase space at the end of the 5th collimator region 214.9 m behind the last final focus quadrupole. Right: Vertical phase space in the same position.

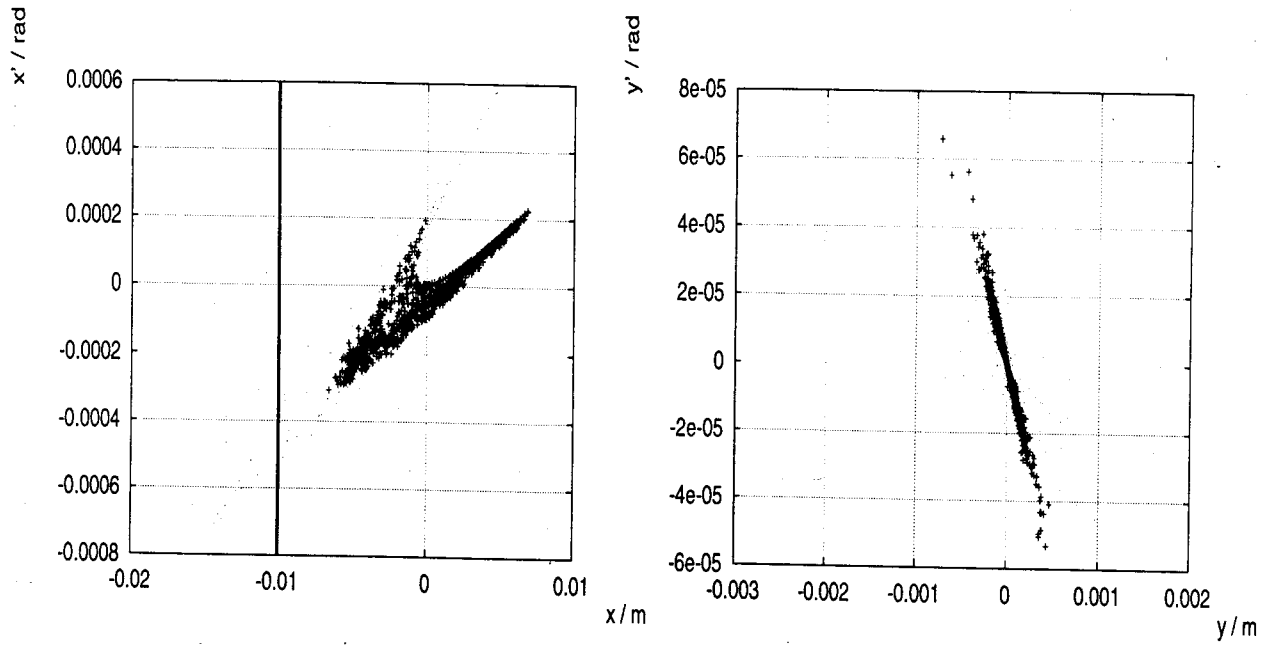

Figure C.6:
Left: Horizontal phase space at the end of the 6th collimator region 234.9 m behind the last final focus quadrupole. Right: Vertical phase space in the same position.

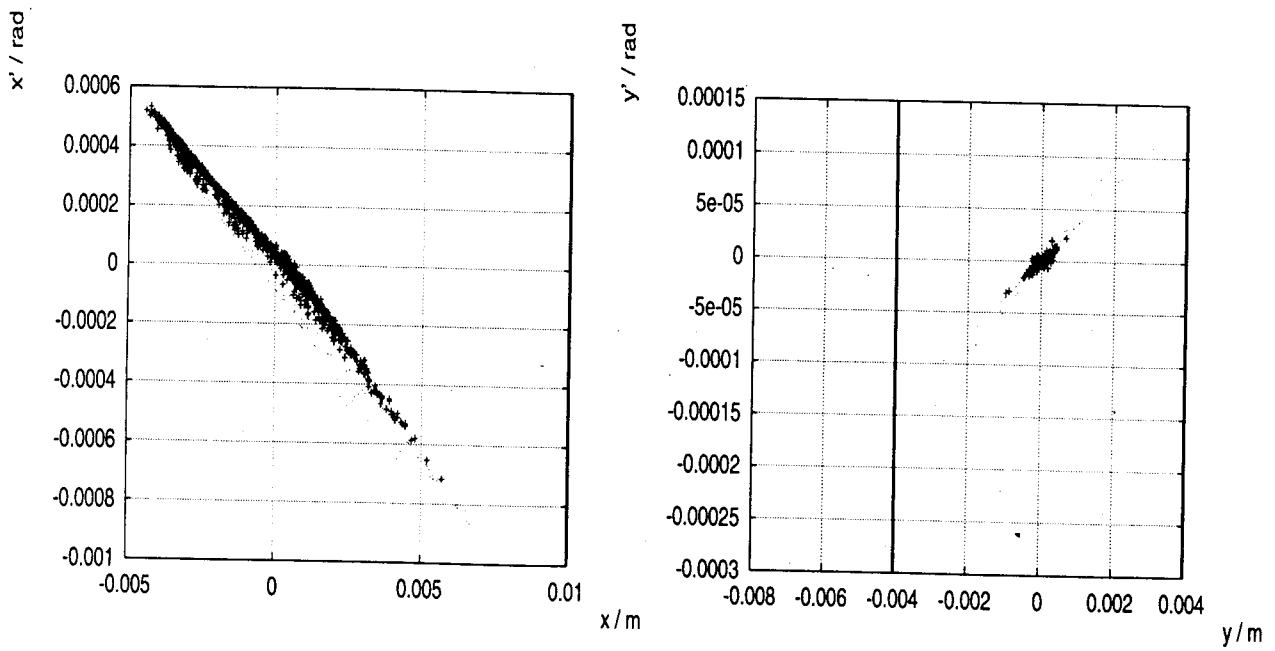

Figure C.7:
Left: Horizontal phase space at the end of the 7th collimator region 394.9 m behind the last final focus quadrupole. Right: Vertical phase space in the same position.

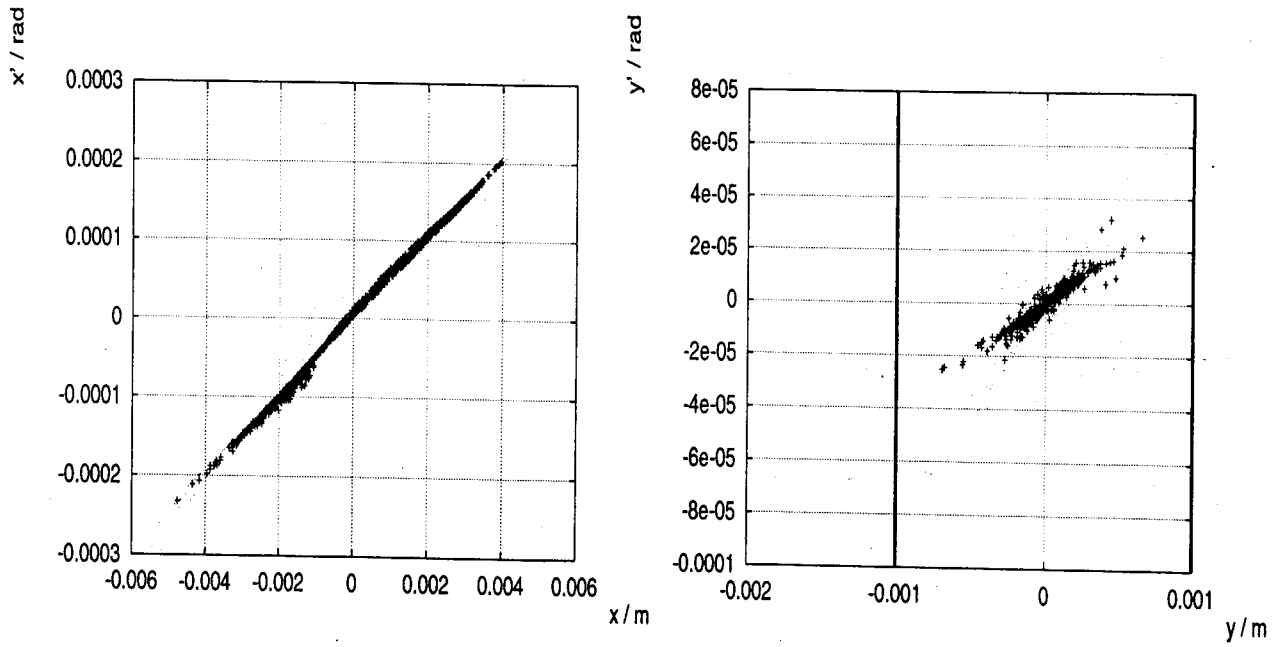

Figure C.8:
Left: Horizontal phase space at the end of the 8th collimator region 436.4 m behind the last final focus quadrupole. Right: Vertical phase space in the same position.

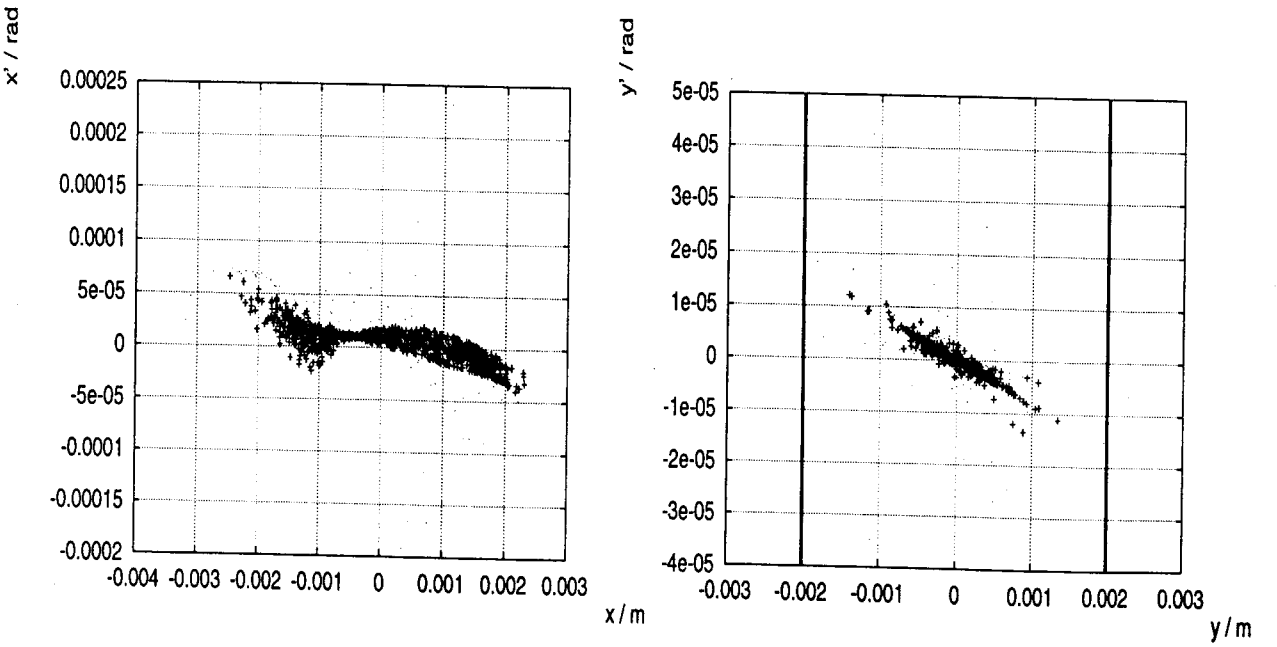

Figure C.9:
Left: Horizontal phase space at the end of the 9th collimator region 450.4 behind the last final focus quadrupoles. Right: Vertical phase space in the same position.

Bibliography

[Bal79] V.E. Balakin, A.A. Mikhailichenko , *The Conversion System for obtaining high polarized electrons and positrons*, Preprint INP 79-85 (1979)

[Bew77] J.P.Bewlett, R.Chasman, *Orbits and fields in the helical wiggler*, Journal of Applied Physics, Vol.48, No.7, July 1977

[Bri90] R. Brinkmann, *Optimization of a Final Focus System for Large Momentum Bandwidth*, DESY-M-90-14, 1990.

[Bri92] R. Brinkmann, Presented at LC92, EFCA Workshop on e^+ e^- Colliders, Garmisch Partenkirchen, 25.7.-2.8.1992, EFCA 93-54

[Brn80] I.N.Bronsein,K.A.Semendjajew , *Taschenbuch der Mathematik*, Verlag Harri Deutsch, Thun und Frankfurt/Main

[Bro80] K.L.Brown, R.V. Servranckx, *Proc. 11th Int'l Conf. on High Energy Accelerators*, (Birkh"auser, Basel 1980) p.656

[Bry94] P.J.Bryant, K. Johnson *The Principles of Circular Accelerators and Storage Rings*, Cambridge University Press 1993

[Buo94] J.Buon, *Beam Phase Space and Emittance*, CERN Accelerator School Proceedings (Editor: S.Turner), CERN 94-01; Vol I, p. 89-115

[CDR97] R.Brinkmann, G.Materlik,J.Rossbach,A.Wagner, *Conceptual Design of a 500 Gev e^+e^- Linear Collider with Integrated X-ray Laser Facility*, DESY 1997-048, ECFA 1997-182

[Dro94] A.Drozhdin, *Extraction of the Spent Beam into the TESLA Beam Capture Section* , DESY Print 1994, TESLA 94-29

[Ell90] P.Elleaume, *Free Electron Laser Undulators, Electron Trajectories and Spontaneous Emission*, Laser Handbook, Vol.6, North-Holland 1990, Ed.: W.B.Colson,C.Pellegrini, A.Renieri

[Flt91] K.Flöttmann and J. Roßbach, *A High Intensity Positron Sources for Linear Colliders*,DESY M-91-11

[Flt93] K.Flöttmann, *Investigations Toward the Development of Polarized and Unpolarized High Intensity Positron Sources for Linear Colliders*,DESY 93-161

[Hal83] K. Halbach, J. Phys., Coll.C1. Suppl. no2, vol.44 (1983)

[Hel62] R.H.Helm, *Adiabatic Approximation for Dynamics of a Particle in the Field of a Tapered Solenoid*, SLAC-4 (1962)

[Hol81] R.Hollebeek, *Disruption Limits for Linear Colliders* Nucl.Instr. and Meth. 184 (1981) 333

[Jack83] J.D.Jackson, *Klassische Elektrodynamik*, W. de Gruyter & Co., Berlin; New York 1982

[JLC92] JLC Group, JLC-I, KEK Report 92-16 (1992)

[Lap71] P.M. Lapostolle, *IEEE Trans. Nucl. Sci.*, No.3, 1101 (1971)

[Loe95] G.A.Loew, T.Weiland, *International Linear Collider Technical Review Committee Report 1995*, Standford University, SLAC-R-95-471

[Kle84] K.Kleinknecht, *Detektoren für Teilchenphysik*, Teubner Studienbücher, Stuttgard 1984

[Kin77] B.M. Kincaid, *A short-period helical wiggler as an improved source of synchrotron radiation*, Journal of Applied Physics, Vol.48; No.7 (1977), 2684-2691

[McD90] Ch. McDowell, *Field Calculation and Optimization of a Linear Collider Final Focus Quadrupole Lens with Tri-Planar Pole Tips*, DESY M-90-10

[Mei95] V.Meier, *GDS - Kurzanleitung -3D-*, DESY MEA,26.07.95

[Nap93] O.Napoly, *A Large Aperture Final Focus System for TESLA* , DESY Print 1993, TESLA 93-27

[Nap94] O.Napoly, E.Klein, J.M.Rifflet *TESLA Final Focus System with superconducting Magnets in the Interaction Region: Optics, Tolerances and Magnet*, DESY Print 1994, TESLA 94-31

[Pre92] W.H.Press et al., *Numerical recipes in FORTRAN*, Cambridge University Press, 1992

[Reu91] E.M.Reuter, J.A.Hodgson, *3D Nummerical Thermal Stress Analysis of the High Power Target for the SLC Positron Source*, SLAC-PUB-5370 (1991)

[Rich76] B.Richter, *Very High Energy Electron-Positron Colliding Beams for the Study of Weak Interaction*, Nucl. Inst. and Meth. 136, 47 (1976)

[Ros95] J. Rossbach, *Options and Trade-Offs in Linear Collider Design*, Contributions to the PAC'95, DESY Print 1995, TESLA 95-11

[Ros91] J. Rossbach, *Positron recycling in high energy linear colliders* , Nucl. Instr. Meth. A309(1991) 25-36

[Ros92] J.Rossbach, P.Schmüser, *Basic Course on Accelerator Physics*, CERN Accelerator School Proceedings (Editor: S.Turner), CERN 94-01; Vol I, p. 17-87

[Sal96] E.L.Saladin, E.A.Schneidmiller M.V.Yurkov, *Calculation of Energy Diffusion in an Electron Beam Due to Quantum Fluctuations of Undulator Radiation*, March 1996, TESLA-FEL 96-05

[Sands] M. Sands, *The Physics of Electron Storage Rings. An Introduction*, University of California - Santa Cruz, Cal.

[Sok68] A.A.Sokolov, I.M.Ternov *Synchrotron Radiation* , Akademie Verlag Berlin, 1968

[Wie95] H. Wiedemann, *Particle Accelerator Physics I+II*, Springer-Verlag Berlin Heidelberg 1995

[Wil92] K. Wille, *Physik der Teilchenbeschleuniger und Synchrotronstrahlungsquellen*, Teubnerverlag. Stuttgard 1992

[Wip97] St. Wipf, M.Marx, private communication.

[Woo83] M.D.Woodley, M.J.Lee, J.Jäger,A.S.King, *Control of Machine Functions or Transport Systems*, IEEE Transaction on Nuclear Science **NS-30**,2367-2370 (1983)

[Yok91] K. Yokoya, P. Chen, *Beam-Beam Phenomena in Linear Colliders*, KEK Preprint 91-2, April 1991 A